

Final Technical Report

**Young Investigator Program:
Quasi-Liquid Grain Boundary Films in Refractory Metals**

Grant. No.: FA9550-07-1-0125
PI: Jian Luo
Institute: Clemson University
Project Period: February 1, 2007 – January 15, 2010
Amount: \$300k (\$100k per year)

Submitted to:

Dr. Joan Fuller
High Temperature Aerospace Materials
Directorate of Aerospace, Chemistry and Material Sciences
Air Force Office of Scientific Research
875 North Randolph Street
Suite 325, Room 3112
Arlington, Virginia 22203
Phone: (703) 696-7236
Fax: (703) 696-8451

Submitted by:

Dr. Jian Luo
Associate Professor
School of Materials Science and Engineering
Clemson University
206 Olin Hall
Clemson, SC 29634
Phone: (864) 656-5961
Fax: (864) 656-1453

REPORT DOCUMENTATION PAGE

Form Approved
OMB No. 0704-0188

Public reporting burden for this collection of information is estimated to average 1 hour per response, including the time for reviewing instructions, searching existing data sources, gathering and maintaining the data needed, and completing and reviewing this collection of information. Send comments regarding this burden estimate or any other aspect of this collection of information, including suggestions for reducing this burden to Department of Defense, Washington Headquarters Services, Directorate for Information Operations and Reports (0704-0188), 1215 Jefferson Davis Highway, Suite 1204, Arlington, VA 22202-4302. Respondents should be aware that notwithstanding any other provision of law, no person shall be subject to any penalty for failing to comply with a collection of information if it does not display a currently valid OMB control number. PLEASE DO NOT RETURN YOUR FORM TO THE ABOVE ADDRESS.

1. REPORT DATE (DD-MM-YYYY) April 14, 2010	2. REPORT TYPE Final Technical Report	3. DATES COVERED (From - To) 02/01/2007 - 01/15/2010		
4. TITLE AND SUBTITLE Nanoscale Quasi-Liquid Grain Boundary Films in Refractory Metals		5a. CONTRACT NUMBER		
		5b. GRANT NUMBER FA9550-07-1-0125		
		5c. PROGRAM ELEMENT NUMBER		
6. AUTHOR(S) Luo, Jian Shi, Jimmy		5d. PROJECT NUMBER		
		5e. TASK NUMBER		
		5f. WORK UNIT NUMBER		
7. PERFORMING ORGANIZATION NAME(S) AND ADDRESS(ES) Clemson University School of Materials Science and Engineering 206 Olin Hall Clemson, SC 29634		8. PERFORMING ORGANIZATION REPORT NUMBER		
9. SPONSORING / MONITORING AGENCY NAME(S) AND ADDRESS(ES) Dr. Joan Fuller Air Force Office of Scientific Research 875 North Randolph Street Suite 325, Room 3112 Arlington, Virginia 22203		10. SPONSOR/MONITOR'S ACRONYM(S) AFOSR		
		11. SPONSOR/MONITOR'S REPORT NUMBER(S)		
12. DISTRIBUTION / AVAILABILITY STATEMENT Approved for public release				
13. SUPPLEMENTARY NOTES				
14. ABSTRACT: Nanoscale intergranular “glassy” films often control the fabrication and mechanical properties of high-temperature structural ceramics. This AFOSR Young Investigator program unequivocally demonstrated the high-temperature formation of analogous liquid-like grain boundary (GB) films in metallic refractory alloys. The bulk computational thermodynamic (CalPhaD) methods were extended to GBs, predicting the onset of GB disordering at as low as 60-85% of the bulk solidus line. Combined experimental and modeling studies of both W and Mo based systems unambiguously demonstrated that the mysterious solid-state activated sintering is due to the increased mass transport in impurity-based liquid-like GB films that are thermodynamic stabilized below the bulk solidus line. Determining this solid-state activated sintering mechanism solved an outstanding scientific problem that has puzzled the materials community for >50 years. Subsequently, Ni-doped Mo was selected for systematical evaluation via characterizing well-quenched specimens and thermodynamic modeling. Finally, “GB ‘phase’ diagrams” were developed as a new materials science tool to control microstructural evolution and forecast high-temperature properties; their correctness has been quantitatively validated by measuring GB diffusivities, direct HRTEM and Auger characterizations, and atomistic simulations. The developed high-temperature interfacial thermodynamic models can be further extended to more complex multicomponent metals and ceramics in future studies.				
15. SUBJECT TERMS refractory alloys; activated sintering; high-temperature interfacial thermodynamics; computational thermodynamics; grain boundary; high-temperature materials; intergranular films; microstructural evolution				
16. SECURITY CLASSIFICATION OF: a. REPORT Unclassified		17. LIMITATION OF ABSTRACT Unlimited	18. NUMBER OF PAGES 78	19a. NAME OF RESPONSIBLE PERSON Jian Luo
b. ABSTRACT Unclassified				19b. TELEPHONE NUMBER (include area code) 864-656-5961
c. THIS PAGE Unclassified				

Abstract

Nanoscale intergranular “glassy” films often control the fabrication and mechanical properties of high-temperature structural ceramics. This AFOSR Young Investigator program unequivocally demonstrated the high-temperature formation of analogous liquid-like grain boundary (GB) films in metallic refractory alloys. The bulk computational thermodynamic (CalPhaD) methods were extended to GBs, predicting the onset of GB disordering at as low as 60-85% of the bulk solidus line. Combined experimental and modeling studies of both W and Mo based systems unambiguously demonstrated that the mysterious solid-state activated sintering is due to the increased mass transport in impurity-based liquid-like GB films that are thermodynamic stabilized below the bulk solidus line. Determining this solid-state activated sintering mechanism solved an outstanding scientific problem that has puzzled the materials community for >50 years. Subsequently, Ni-doped Mo was selected for systematical evaluation via characterizing well-quenched specimens and thermodynamic modeling. Finally, “GB ‘phase’ diagrams” were developed as a new materials science tool to control microstructural evolution and forecast high-temperature properties; their correctness has been quantitatively validated by measuring GB diffusivities, direct HRTEM and Auger characterizations, and atomistic simulations. The developed high-temperature interfacial thermodynamic models can be further extended to more complex multicomponent metals and ceramics in future studies.

Table of Contents

Abstract	2
Narrative	
1. Overview.....	4
2. Background.....	6
3. Summary of Key Results	8
3.1. Nanoscale Quasi-Liquid IGFs in Doped W	8
3.2. Solid-State Activated Sintering: Resolving a 50 Year Old Mystery.....	10
3.3. “GB Diagrams” – A New Materials Science Tool?	12
3.4. A Systematical Study of Ni-Doped Mo	12
3.5. Complexion: A Transformative Concept & Contributions via This Program	16
4. Relevance to Aerospace Materials and Broader Impacts	17
5. Executive Summary (Conclusions).....	19
A List of People Involved	20
A Special Highlight (Student Award).....	21
A List of Publications	22
A List of Presentations.....	22
References	25
Appendix A: Experimental Procedures	34
Appendix B: Thermodynamic Models	43
Appendix C: Sintering and GB Diffusivities of Ni-Doped Mo.....	62

LIST OF ACRONYMS

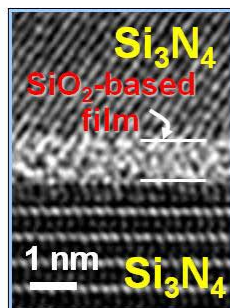
GB: Grain Boundary
IGF: Intergranular Film
CalPhiD: <u>Calculation of Phase Diagram</u>
AES: Auger Electron Spectroscopy
TEM: Transmission Electron Microscopy
HRTEM: High-Resolution TEM
STEM: Scanning TEM
SEM: Scanning Electron Microscopy
XRD: X-Ray Diffraction
AFOSR: Air Force Office of Scientific Research
YIP: Young Investigator Program

1. Overview

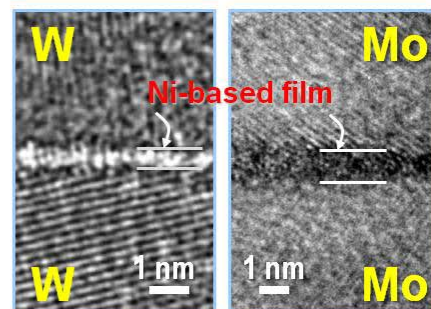
Nanoscale, impurity-based, intergranular films (IGFs) are commonly observed in Si_3N_4 , SiC , SiAlON , Al_2O_3 , ZrO_2 , BN , B_4C and other high-temperature structural ceramics. They often control sintering, grain growth, and mechanical properties [1]. With the support of this AFOSR Young Investigator Program (AFOSR-YIP), we discovered and studied an analogous interfacial phenomenon in binary refractory metals:

- We demonstrated the stabilization of subsolidus quasi-liquid IGFs (Fig. 1) [2].
 - Despite various indications [1], this is the first direct high-resolution transmission electron microscopy (HRTEM) observation of quasi-liquid IGFs in metallic alloys.
 - This observation deepens the understandings of this class of interfacial phenomena.
- We demonstrated that short-circuit diffusion in subsolidus quasi-liquid IGFs result in “solid-state activated sintering” in refractory metals. This work solved **an outstanding scientific problem that has puzzled the materials community for over 50 years** [2, 3].
- We extended bulk computational thermodynamic (CalPhaD) methods to model grain boundaries (GBs) and predicted that the nanoscale quasi-liquid IGFs can be stabilized at temperatures as low as 60-85% of the bulk solidus lines [3, 4].
 - Such quasi-liquid IGFs can critically affect the microstructural evolution and high-temperature properties [3].

Well-Known



Our Discovery



Scientific Significance: Metallic counterparts to IGFs in ceramics?

- Relative simple systems → high-T interfacial thermodynamics
- Help to understand more complex ceramics, e.g., Si_3N_4 & UHTM

Technological Importance

- GB diffusivity ↑ (sintering? Coble creep?)
- GB mobility ? (grain growth? microstructural evolution?)
- High-T mechanical properties, e.g. GB sliding? creep?
- Oxidation or corrosion resistance?
- GB embrittlement? Liquid-metal embrittlement?

Relevant to high-T materials (because its stability scales with T_m)

A Long-Range Scientific Goal: GB “phase” diagrams

- A new tool for mechanism-informed design of high-T materials.

Fig. 1: The well-known equilibrium-thickness IGFs in ceramic materials and analogous quasi-liquid IGFs in refractory metals.

We further proposed a long-range scientific goal of developing “GB diagrams” as a new tool for mechanism-informed materials design. Fig. 2 represents two of such GB diagrams developed and verified in this AFOSR-YIP. These GB diagrams can be used to **a**) provide useful information for designing optimal fabrication protocols and **b**) forecast certain high-temperature material properties.

This interfacial phenomenon is more important for **high-temperature materials**, such as refractory metals and ceramics. This is because GB energy increases with increasing melting temperature, and greater GB energies can stabilize liquid-like GB structures over larger undercooling ranges and critically affect microstructural evolution (e.g., sintering and grain growth) and high-temperature properties (e.g., creep). Furthermore, impurity-based IGFs will often be retained upon cooling and affect low-temperature properties (e.g., embrittlement) [1].

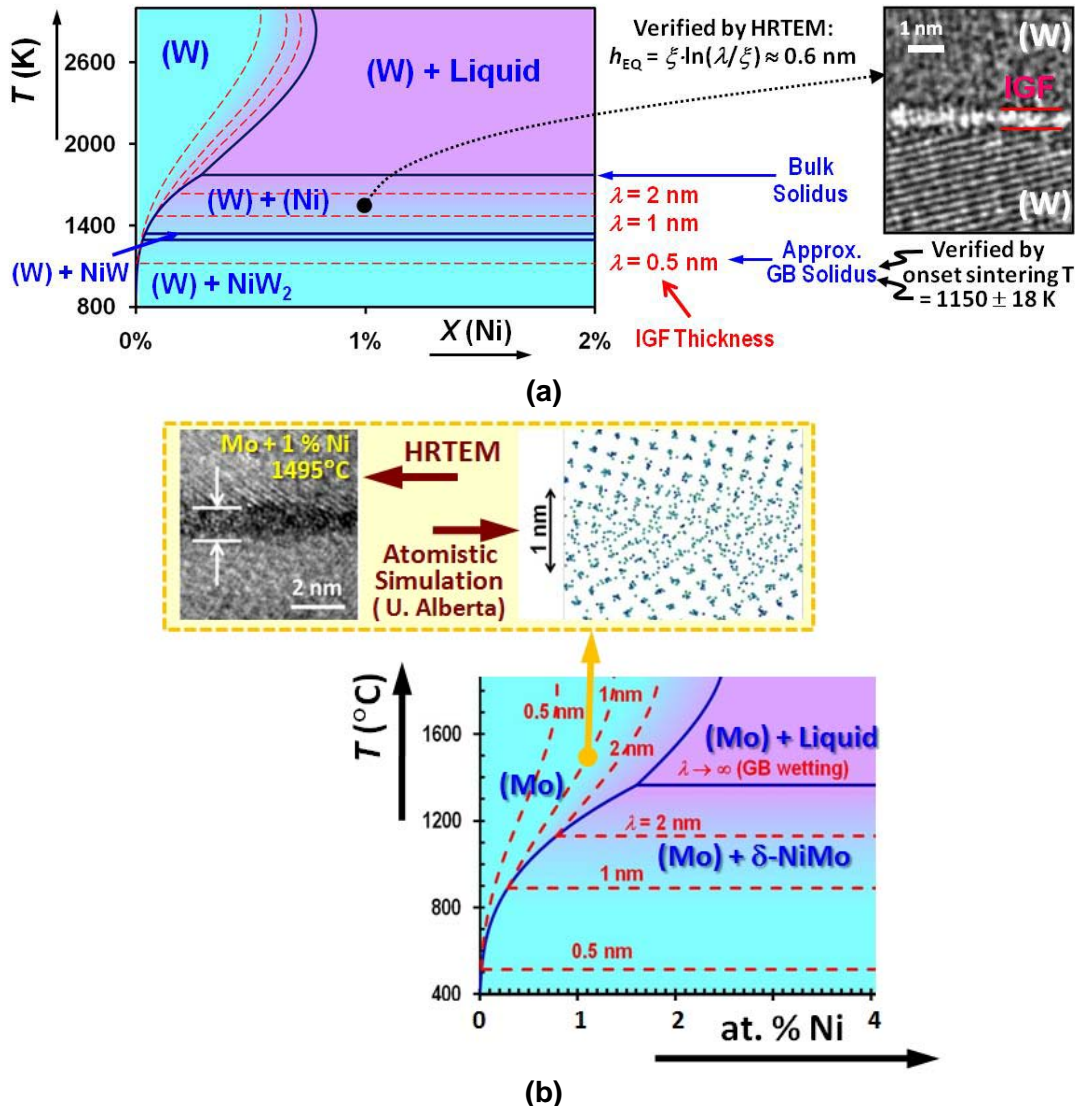


Fig. 2: “GB diagrams” for (a) Ni-doped W and (b) Ni-doped Mo, in which computed thicknesses of stable quasi-liquid IGF (λ 's; red dashed lines) are plotted in the binary bulk phase diagrams. The colors represent the thermodynamic tendency for GBs to disorder. These computed GB diagrams were validated via experiments (by HRTEM, Auger and GB diffusivity measurements) and atomistic simulations (by U. Alberta collaborators).

2. Background

2.1. Premelting

Premelting, first postulated by Faraday in 1842, refers to the stabilization of nanoscale liquid-like interfacial layers below the bulk melting temperature. **Surface premelting** has been observed in many unary solids [18-20]. For example, ice premelting (Fig. 3) plays important roles in snow “sintering”, glacier motion (creep) [20], and the ice-skating process [21].*

Materials researchers have also sought to confirm the existence of **GB premelting**. In 1989, Balluffi *et al.* reported [22] that GB premelting did not occur until $0.999T_{\text{melting}}$ for pure Al. The occurrence of GB premelting in colloidal crystals was reported in 2005 (Fig. 4) [23]. Nonetheless, the importance of GB premelting in unary materials remains controversial.

In multicomponent materials, however, a class of “premelting-like” films can be stabilized at GBs over wider ranges of undercooling, wherein GB disordering is enhanced by a concurrent adsorption in a “prewetting” regime. Here, “**prewetting**” refers to an adsorption transition initially proposed in the Cahn critical-point-wetting model [24] for binary de-mixed liquids.

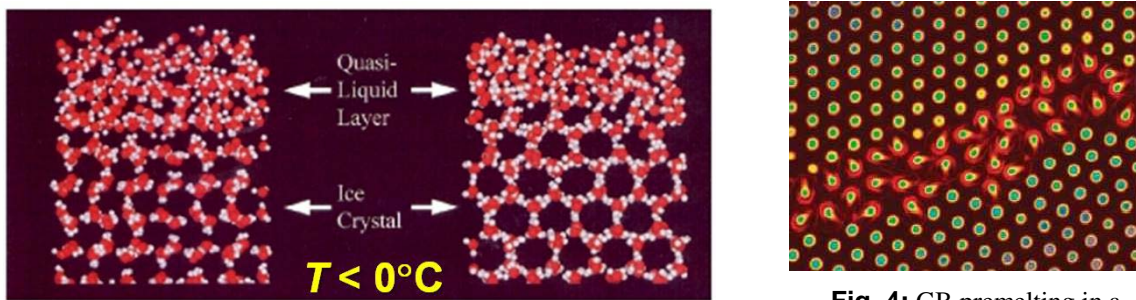


Fig. 3: Surface premelting in ice (atomistic simulation by Furukawa and Nada, 1997).

Fig. 4: GB premelting in a colloidal crystal, an image featured on the cover of *Science* [23].

2.2. Equilibrium-Thickness Intergranular Films (IGFs)

Researchers studying ceramics have discovered the widespread existence of a unique class of **intergranular films (IGFs)** that exhibit the following **distinct characteristics** [1]:

- self-selecting or “equilibrium” thickness on the order of 1 nm;
- composition that is neither observed, nor stable, as a bulk liquid/glass phase (e.g., the average film composition can lie within a bulk immiscible gap!); and
- quasi-liquid structure that is neither completely crystalline, nor fully amorphous.

These nanoscale IGFs can be alternatively understood to be:

- liquid-like interfacial films that adopt an equilibrium thickness in response to several attractive and repulsive interfacial forces (the Clarke model) [25-27] or
- a unique class of disordered multilayer adsorbates (the Cannon model) [28].

The stabilization of impurity-based, quasi-liquid IGFs at subsolidus temperatures have been observed [2, 29-31], provoking an analogy to “premelting” in unary systems.

* The popular “pressure melting” theory for ice-skating is flawed [21]. An ice skater can exert a pressure to cause local melting at only a few degrees below zero. Premelting and “frictional heating” enable skating at -35 °C.

In 2006, Tang, Carter, and Cannon (MIT and Berkeley) [1] proposed to explain subsolidus IGFs in binary systems from coupled GB premelting (structural disordering) and prewetting (adsorption) transitions [32]. The Tang-Carter-Cannon model [32] serves as a qualitative basis for understanding IGFs in ceramics. Electrostatic [26] and van der Waals (vdW) London dispersion forces [33] must be separately included, resulting in complex adsorption and wetting behaviors. For example, nanoscale equilibrium-thickness IGFs can often persist above the bulk solidus line, due to the presence of the attractive van der Waals (vdW) London dispersion forces in ceramics [1, 34]. IGFs in ceramics can also represent a metastable equilibration.

In addition to the well-known silicate-based IGFs in Si_3N_4 , SiC and other structural ceramics, thin interfacial films of similar characteristics have been found in an increasing number of other material systems (Fig. 5) [1], including:

- non-silicate-based IGFs in various oxide ceramics;
- IGFs at ceramic hetero-interfaces;
- silicate-based IGFs at metal-oxide interfaces;
- free-surface counterparts to IGFs; and
- metallic IGFs.

The PI has recently published a 43-page Critical Review article about the observations, theories, and technological importance of nanoscale quasi-liquid interfacial films [1]. More specifically, the existence of metallic IGFs was unequivocally and directly confirmed in our AFOSR-YIP [2-4, 9]. Moreover, understanding “surface amorphous films” (SAFs, i.e., the free-surface counterparts to IGFs) [13] can help to control nanoscale native oxide films and their detrimental effects in the densification of non-oxide high-temperature materials.

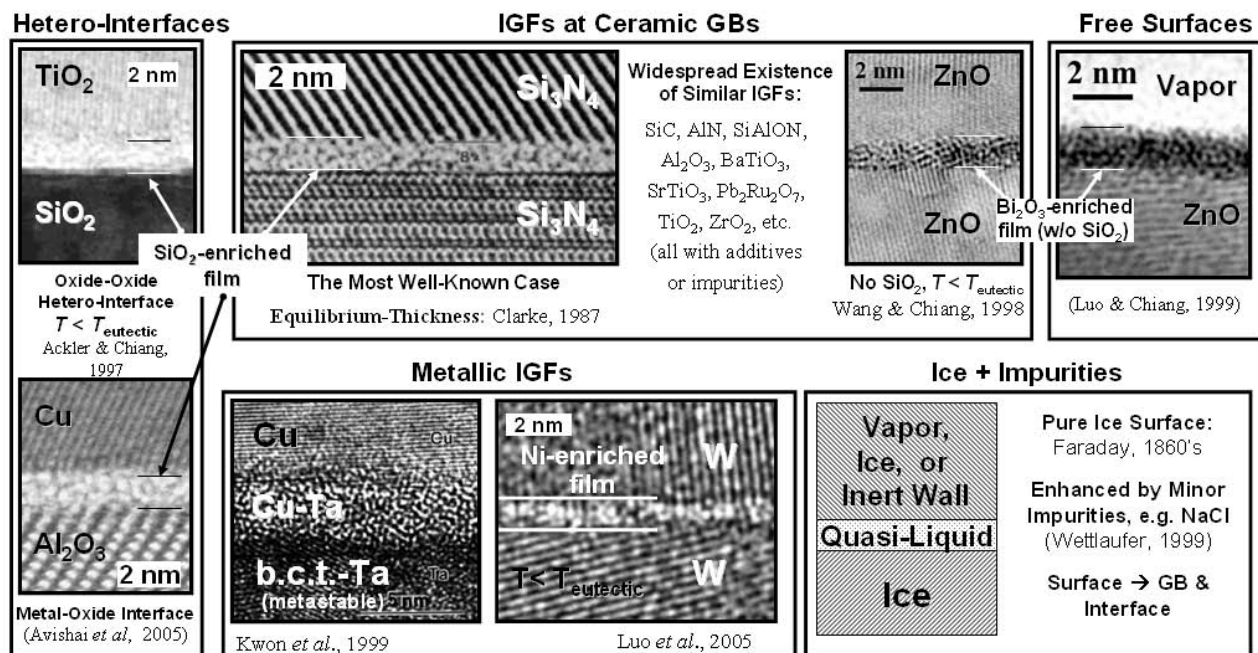


Fig. 5: The widespread existence of various impurity-based quasi-liquid interfacial films. Reprinted from the PI's critical review (an AFOSR-supported publication [1]).

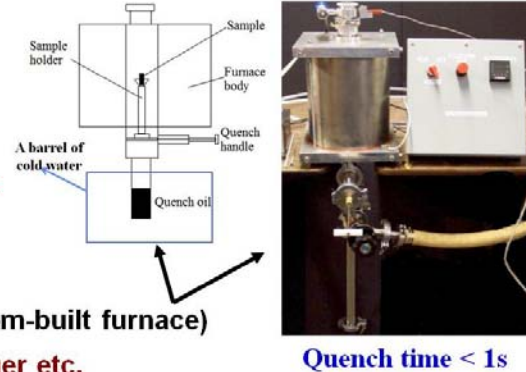
3. Summary of Key Results

The experimental and computational methods used in this project are schematically illustrated in Fig. 6. The detailed experimental procedures are documented in **Appendix A**. Key results are discussed in the following sections.

Methods

Experiments

- **Carefully-prepared specimens**
 - High-purity
 - Isothermally annealed
 - Well quenched (using custom-built furnace)
- **Characterized by HRTEM, Auger etc.**
- **Controlled sintering experiments → GB diffusivity**



Theories & Modeling

- Extend bulk CalPhiD ([Calculation of Phase Diagram](#)) to GBs
- Statistical thermodynamic models → interfacial energies
- Atomistic modeling (via collaboration w/ U. Alberta)

Fig. 6: Summary of experimental and theoretical methods used in this study.

3.1. Nanoscale Quasi-Liquid IGFs in Doped W

We unequivocally demonstrated the stabilization of nanoscale quasi-liquid IGFs well below the bulk eutectic temperature in Ni-doped W (Fig. 7) [2]. While indirect evidence has been reported previously [42], this is the first direct HRTEM evidence supporting the existence of such nanoscale quasi-liquid IGFs in metallic alloys.

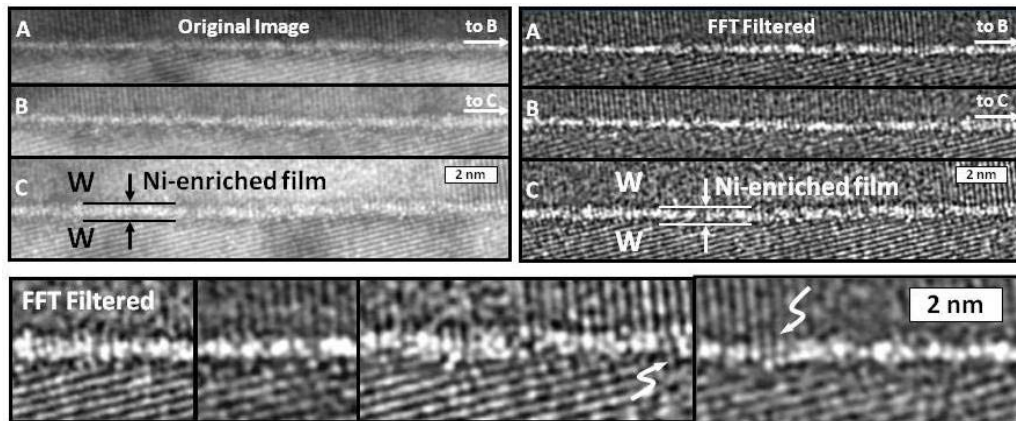


Fig. 7: Representative HRTEM image of nanoscale quasi-liquid IGFs that are **thermodynamically stable** at 95 K below the bulk eutectic temperature in Ni-doped W.

Reprinted from an AFOSR supported publication in *Acta Materialia* [2].

By extending bulk CalPhaD (Calculation of Phase Diagram) methods to GBs, we predicted that quasi-liquid IGFs can be stabilized at W GBs as low as 60-85% of the bulk solidus temperatures [4]. The basic concepts of this model are schematically illustrated in Fig. 8. A refined thermodynamic model is elaborated in **Appendix B**. The key results of this model [3, 4] are briefly discussed below.

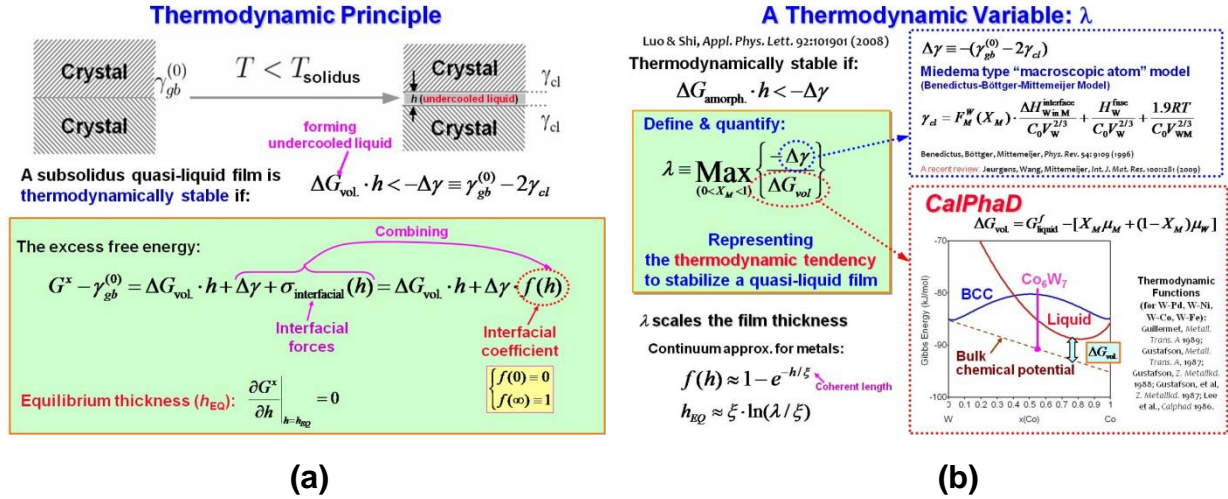


Fig. 8: Schematic illustration of the proposed thermodynamic model.

As shown in Fig. 8(a), a subsolidus quasi-liquid IGF can be thermodynamically stable if:

$$\Delta G_{\text{amorph.}} \cdot h < (-\Delta\gamma) \equiv \gamma_{gb}^{(0)} - 2\gamma_{cl} \quad (1)$$

Where: h is the film thickness, $\gamma_{gb}^{(0)}$ is the excess energy of a random GB without adsorption, and γ_{cl} is the crystal-liquid interfacial energy. The volumetric free energy to form an undercooled liquid ($\Delta G_{\text{amorph.}}$) of a binary alloy can be quantified using the bulk CalPhaD methods. A thermodynamic variable λ is defined to represent the maximum thickness of a quasi-liquid IGF that can be thermodynamically stable (without consideration of interfacial forces):

$$\lambda \equiv \text{Max}\{-\Delta\gamma / \Delta G_{\text{amorph.}}\}, \quad (2)$$

The definition and quantification of the thermodynamic variable λ are schematically illustrated in Fig. 8(b). Further details of this and refined models are discussed in **Appendix B**.

Five computed “GB diagrams” are shown in Fig. 2 (Ni-doped W; Ni-doped Mo) and Fig. 9 (Pd-doped W; Co-doped W; and Fe-doped W), where the lines of constant λ are plotted in the bulk binary phase diagrams.

For metallic alloys, the dominance of an exponentially-decaying interfacial force allows a simple estimate of the actual “equilibrium” IGF thickness as: $h_{\text{EQ}} \approx \xi \cdot \ln(\lambda/\xi)$, where ξ is the coherent length. The “GB solidus temperature” (T_{GBS}) can then be estimated by $\lambda(T_{\text{GBS}}) = \xi \approx 0.5\text{-}1 \text{ nm}$. Interfacial forces are more complex in ceramic materials [1].

In metallic alloys, the film thickness is divergent as the bulk solidus line is approached from below, above which a bulk liquid phase appears and completely wets the GBs. In ceramics, however, attractive vdW forces can stabilize nanoscale IGFs above the bulk solidus lines.

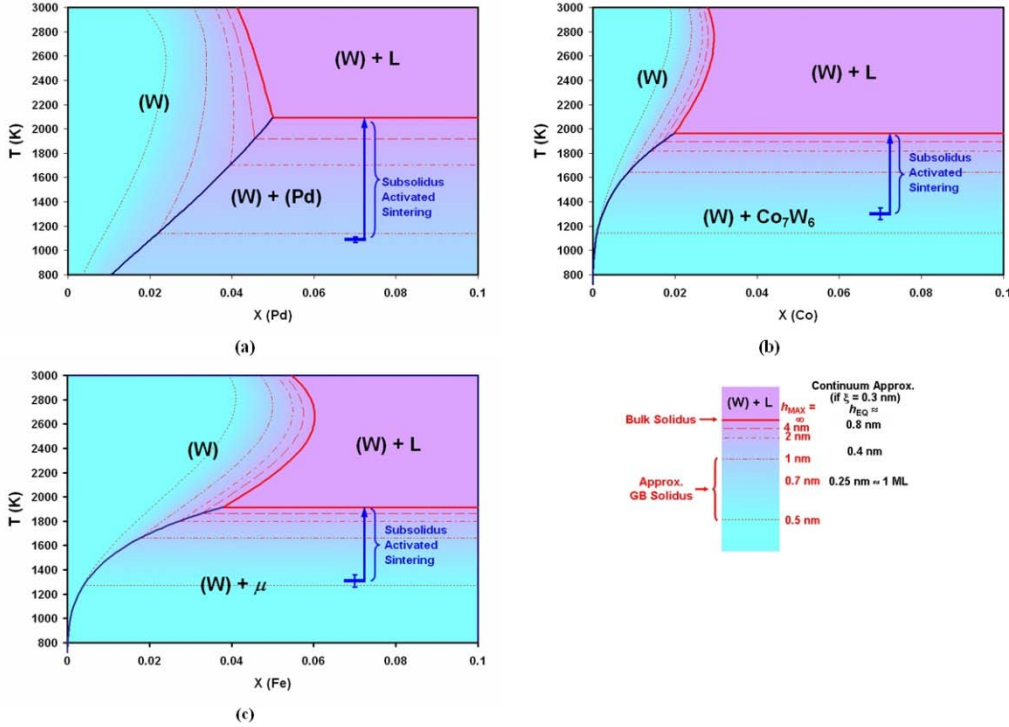


Fig. 9: Computed GB diagrams for (a) Pd-doped W, (b) Co-doped W, and (c) Fe-doped W. Two additional computed GB diagrams for Ni-doped W and Ni-doped Mo are shown in Fig. 2. In each bulk phase diagram, a series of dashed and dotted lines were plotted to represent the conditions that 4, 2, 1 and 0.5 nm thick quasi-liquid IGFs can be thermodynamically stable at GBs. The ranges of subsolidus activated sintering are also labeled. Redrawn from an AFOSR supported publication in *Curr. Opin. Solid State Mater. Sci.* [3].

3.2. Solid-State Activated Sintering: Resolving a 50-Year-Old Mystery

Solid-state (subsolidus) activated sintering refers to the enhancement of densification due to solid-state sintering additives. In their classic 1978 review [43], Coble and Cannon stated that:

"The most significant changes which have been taken place in recent years regard the finding with respect to densification below the eutectics in numerous systems, notably WC:Co, W:Ni, ..."

The exact mechanism has puzzled the materials community for decades.

A prior study by the PI provided the first insight towards resolving this mystery [44]. In Bi_2O_3 -doped ZnO , nanoscale “glassy” IGFs were found to be stabilized at GBs well below bulk T_{eutectic} , occurring concurrently with the onset of activated sintering, implying that the enhanced sintering is likely due to the short-circuit diffusion in these subsolidus IGFs [44]. While a ceramic is not the best system to unequivocally prove the hypothesis, due to the complex interfacial forces, we proved this hypothesized activated sintering mechanism systematically using the binary refractory metals in this AFOSR-YIP, as elaborated subsequently.

It has been commonly understood since the 1950’s that the addition of < 1 % of various transition metals can significantly increase the densification of W and Mo in the subsolidus region [43, 45-51]. In a classical model, the solid-state “activator” is presumed to be the secondary bulk crystalline phase that completely wets the GBs. We recently unequivocally illustrated that solid-state wetting does not occur (Fig. 10; Fig. 13) [2, 3, 9]. Instead, quasi-liquid

IGFs can be stabilized at GBs well below the bulk solidus line and lead to an enhanced GB diffusion and activated sintering [2-4, 9].

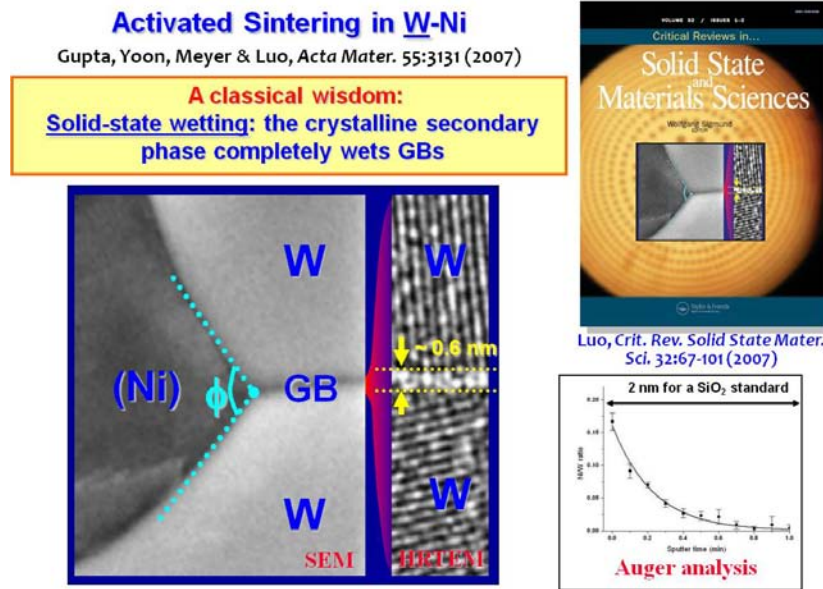


Fig. 10: In contrast to the classical wisdom, the Ni-rich crystalline phase does not wet the W GB. HRTEM and Auger electron spectroscopy (AES) revealed the stabilization of nanoscale Ni-enriched, liquid-like IGFs below the bulk eutectic temperature. Combined experimental and modeling studies unambiguously demonstrated that the mysterious solid-state activated sintering is due to the increased mass transport in impurity-based liquid-like GB films that are thermodynamic stabilized below the bulk solidus line. Determining this mechanism for solid-state activated sintering in refractory alloys solved an outstanding scientific problem that has puzzled the materials community for >50 years.

Subsolidus activated sintering experiments have been conducted for W using various dopants with significantly different effectiveness [48, 52], enabling a critical test of the hypothesized sintering mechanism. On the other hand, by using onset sintering as an indicator for GB disordering, we can test whether our model can predict GB disordering, which has broader applications beyond sintering [4]. The comparisons between the predictions and experiments for five systems (W-M, M = Pd, Ni, Co, Fe and Cu) are illustrated in Table 1 and Fig 11 [4]. These results not only support the hypothesized subsolidus activated sintering mechanism, but also the correctness and usefulness of our model described in §3.1.

Table 1: Measured onset sintering temperatures vs. predicted GB disordering temperatures. Reprinted from an AFOSR supported publication in *Appl. Phys. Lett.* [4].

	$T_{e/p}$ (K)	$\Delta \gamma_{e/p}$ (J/m ²)	T_{sinter} (K)	T_{GBS} (K)
W-Pd	2088	-0.60	1090 ± 23	<1141 ^a
W-Ni	1768	-0.52	1150 ± 18	1121–1470
W-Co	1962	-0.40	1301 ± 49	1140–1644
W-Fe	1910	-0.37	1308 ± 50	1273–1664
W-Cu	1357	+0.49	No activated sintering	No IGF

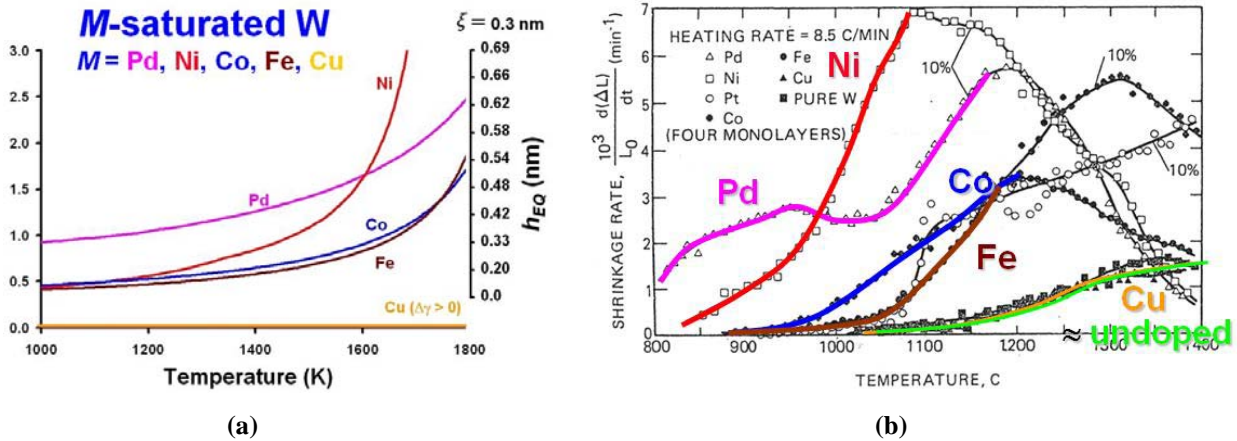


Fig. 11: (a) Computed IGF thickness vs. temperature for dopant-saturated W specimens. (b) The experimental sintering (densification) rates. Reprinted from an AFOSR supported publication in *Appl. Phys. Lett.* [4].

3.3. “GB Diagrams” – A New Materials Science Tool?

In this AFOSR-YIP, we developed **a long-range scientific goal** of establishing “GB diagrams” as a new tool for mechanism-informed materials design, which involves three concepts:

- Guided by GB diagrams, fabrication protocols can be designed to utilize the most appropriate GB structures to achieve optimal microstructures, e.g., utilizing liquid-like GBs for low-temperature sintering;
- Heat treatment protocols can be devised to adjust GB structures to achieve the desired properties, e.g., to de-wet impurity-based IGFs to mitigate GB embrittlement; and
- GB diagrams provide information for predicting high-temperature properties, e.g., creep resistance.

The necessity of developing such GB diagrams is demonstrated by our studies of the solid-state activated sintering of ceramics [44] and metals [2]. Since nanoscale quasi-liquid IGFs can form well below the bulk solidus lines and result in enhanced sintering behaviors similar to liquid-phase sintering [4], bulk phase diagrams are **not adequate** for designing activated sintering protocols. On the other hand, our results indeed showed that the onset activated sintering can be predicted from the computed GB diagrams (Table 1; Fig. 9; Fig. 11).

Furthermore, such GB diagrams can lead to applications in the mechanism-informed design of fabrication protocols (beyond sintering) and the prediction of high-temperature properties.

3.4. A Systematical Study of Ni-Doped Mo

We recently systematically evaluated the Ni-doped Mo system via characterizing *well-quenched* specimens, in conjunction with thermodynamic modeling. In contrast to prior beliefs [50, 53], we found that the δ -NiMo phase does not wet Mo GBs in the solid state (Fig. 13). On the other hand, the Ni-rich liquid wets Mo GBs completely above the solidus line (Fig. 13).

Furthermore, HRTEM and AES analysis demonstrated that nanometer-thick quasi-liquid films persist at GBs into the single-phase region ($X < X_{\text{solidus}}$), where the bulk liquid phase is no longer stable (Fig. 12). While such quasi-liquid IGFs promote sintering at firing temperatures, they will become brittle δ -NiMo layers upon cooling, resulting in GB embrittlement [50].

Furthermore, molecular dynamic simulation conducted by our collaborator, Professor Hao Zhang from the University of Alberta in Canada, supported our experiments in proving that the addition of Ni (below the bulk solid solubility limit) causes GBs to widen and become more disordered (Fig. 14). This also significantly increases the GB diffusion (Fig. 14(c)).

Measured: $h = 0.80 \pm 0.12 \text{ nm}$

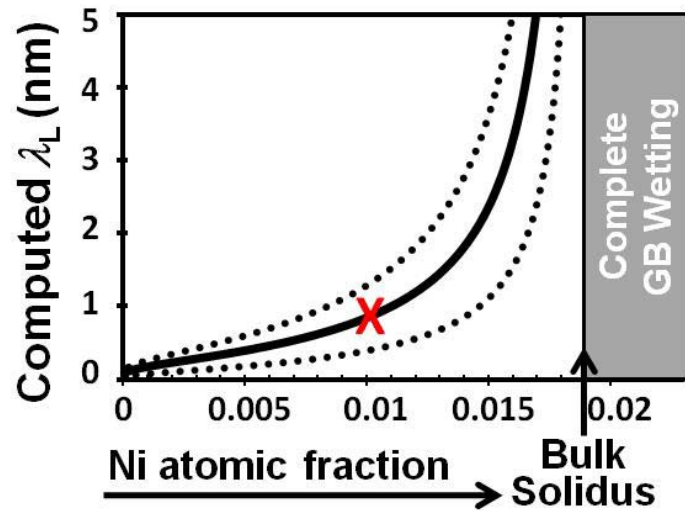
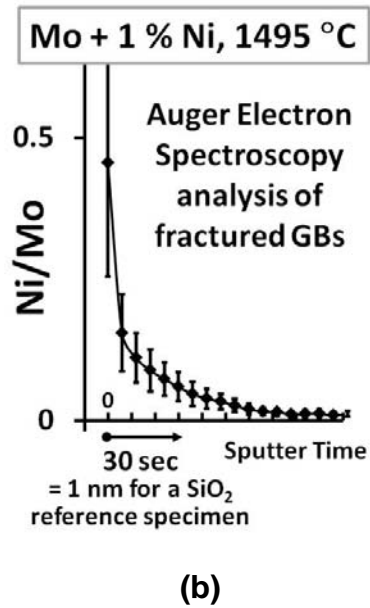
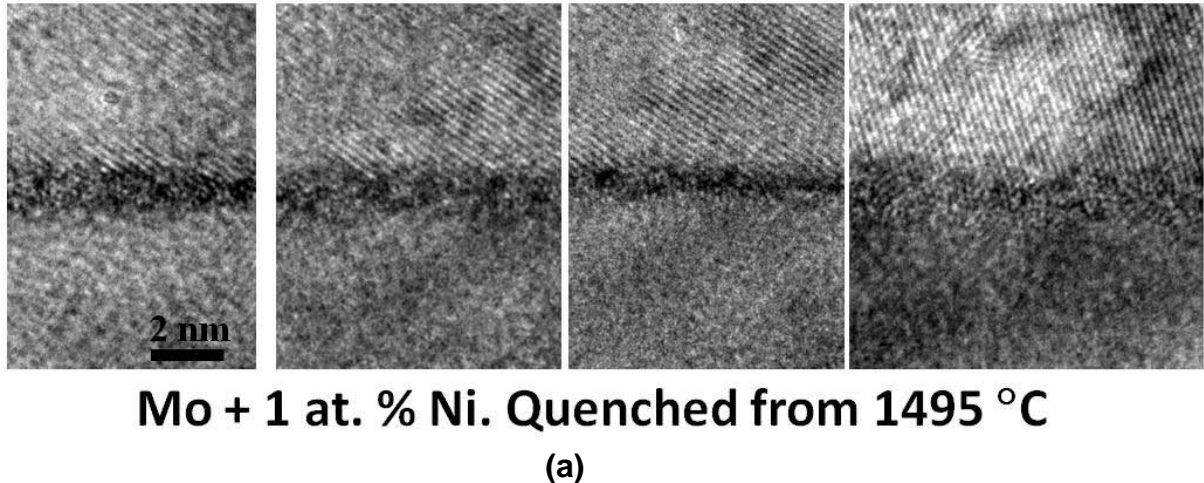


Fig. 12: (a) HRTEM images and (b) AES analysis revealed the thermodynamic stabilization of $\sim 0.8 \text{ nm}$ thick quasi-liquid IGFs in a Mo + 1% Ni specimen at 1400 °C, which lies in the single-phase region where the bulk liquid is not yet stable. (c) Computed thickness of stable IGFs vs. the Ni bulk fraction at 1400 °C, where the “X” indicates the Mo + 1% Ni specimen. Reprinted from an AFOSR supported publication in *Appl. Phys. Lett.* [9].

Ni-doped Mo: Summary

Shi & Luo, APL 94: 251908 (2009)

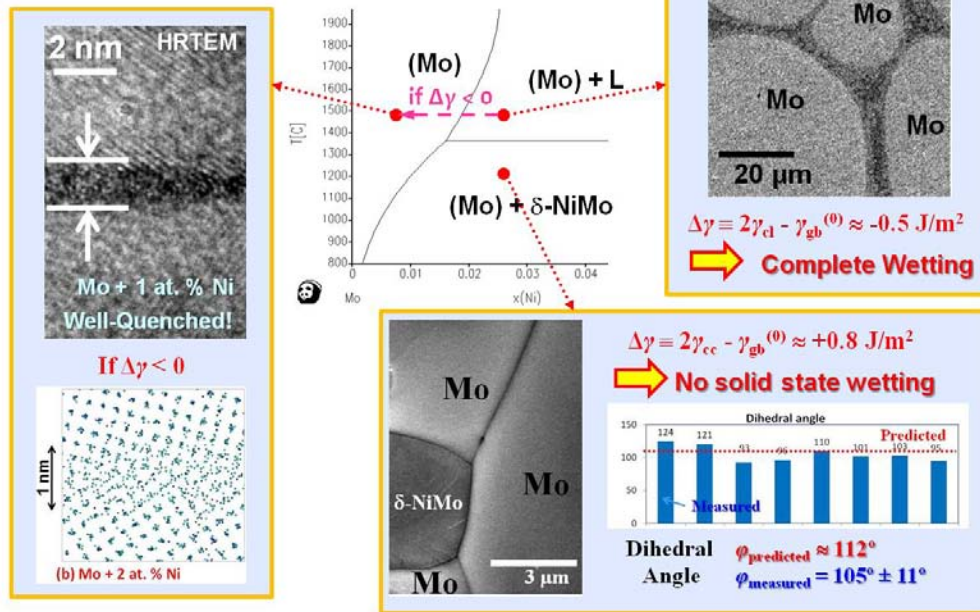


Fig. 13: SEM images reveal that (a) the crystalline δ -NiMo phase does not wet Mo GBs, but (b) the Ni-rich liquid phase does wet Mo GBs completely. (c) HRTEM and AES reveal the thermodynamic stabilization of ~ 1 -nm-thick quasi-liquid IGFs in the single-phase region (where the bulk liquid is no longer stable). Images reprinted from an AFOSR supported publication in *Appl. Phys. Lett.* [9].

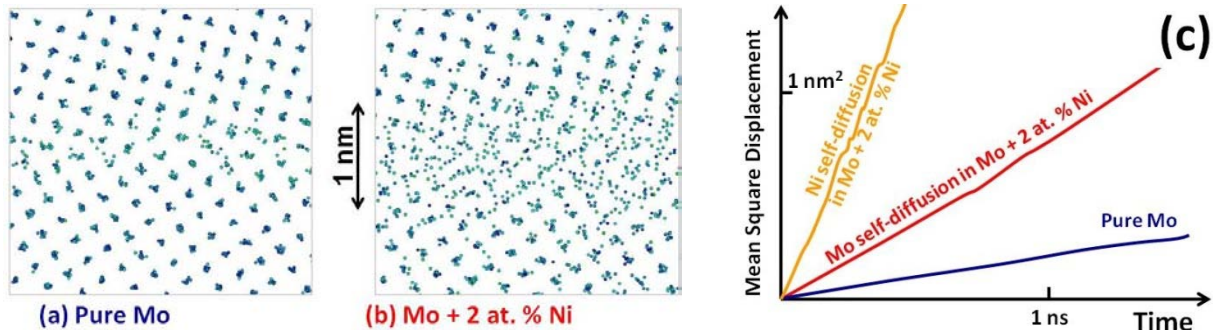


Fig. 14: Snapshots of the atomistic simulation illustrate that (b) a GB in Ni-doped Mo is significantly more disordered and wider than that in (a) pure Mo. (c) Simulation shows that GB diffusivity is significantly increased with Ni doping. Figures are courtesy of our collaborator, Professor Hao Zhang, Univ. Alberta in Canada.

Furthermore, we constructed a GB diagram for Ni-doped Mo, which is shown in the upper-right corner in Fig. 15. To verify the correctness of this computed GB diagram, we conducted well-controlled sintering experiments to extract GB diffusivity as a function of the temperature and overall composition. The experimental procedure and detailed results are documented in **Appendix C**. These experimental results can be well explained from the computed GB diagram. The key points are summarized in Fig. 15 and discussed below:

- Major jumps in measured GB diffusivities (labeled by the red stars in Fig. 15(A) and (B)) occur at a “GB solidus line” that corresponds to a computed λ_L value of ~ 0.5 nm. This GB

solidus line (i.e., the thick red dashed line in Fig. 15), where presumably quasi-liquid IGFs start to form, is distinct from the bulk solidus line. Since the densification represents an average effect of many GBs, a gradual transition in GB diffusivity was expected and observed.

- At the bulk solidus line where the bulk liquid appears, the measured (effective) GB diffusivities only jump moderately (labeled by the blue stars in Fig. 15(A) and (E)).
- Below the bulk peritectic temperature, there is no discontinuity in the measured GB diffusivity at the bulk solvus line (labeled by the light purple star in Fig. 15(B)).
- In pure Mo, the measured GB diffusivity increases with increasing temperature (Fig. 15(C)), which is well expected.
- In the single-phase region, the measured GB diffusivity appears to decrease with increasing temperature at a constant Ni fraction of 0.5 % (Fig. 15(D)). This counterintuitive result can be fully explained from the computed GB diagram. This abnormal behavior of decreasing GB diffusivity with increasing temperature is due to the fact that Mo-Ni has a “retrograde” phase diagram. With increasing temperature, this fixed composition of 0.5 % moves away to the metastable extension to the solidus line (i.e., the black dotted line in the computed GB diagram in Fig. 15). Consequently, the free energy penalty for forming undercooled liquid increases with increasing temperature. Consistently, the computed λ_L decreases with increasing temperature, which is shown in the inset of Fig. 15(D). **Thus, a GB can “solidify” with increasing temperature!**

The above comparisons clearly support the correctness and usefulness of our thermodynamic models and the computed GB diagram.

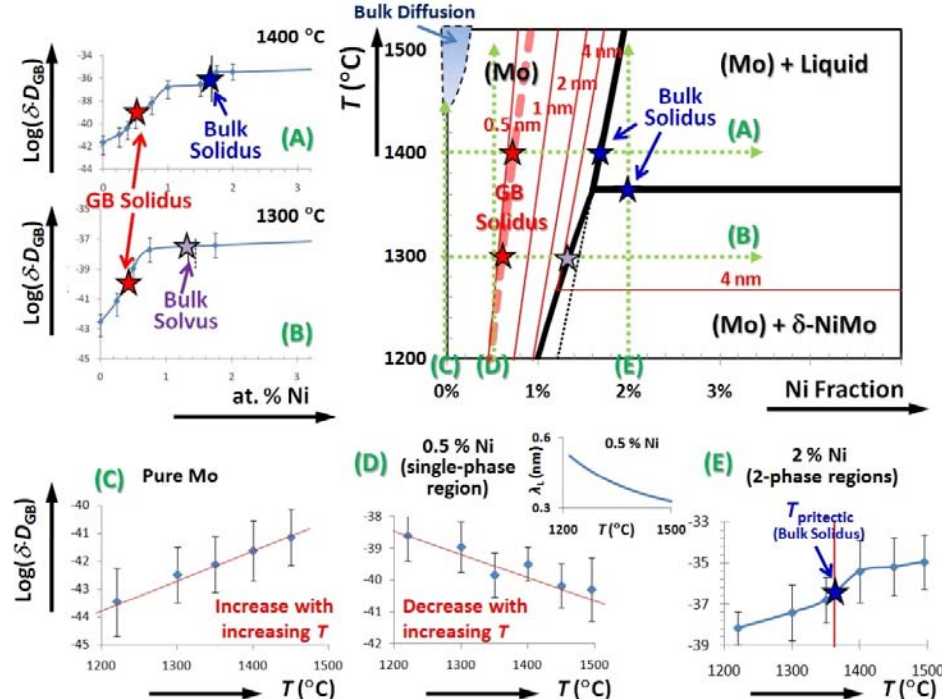


Fig. 15: Measured GB diffusivities (panels (A) to (E)) are compared to the computed GB diagram for Ni-doped Mo (shown in the upper-right corner) to validate the correctness and usefulness of our thermodynamic models.

3.5. Complexion: A Transformative Concept & Contributions via This Program

Tang *et al.* [32, 35] suggested an extension of the Gibbs definition of bulk phases to equilibrium GB features and designated them as "GB complexions". They predicted first-order and continuous GB transitions [32, 35], resulting in *abrupt changes* in GB-sensitive transport, mechanical and physical properties.

In 2007, Dillon and Harmer (Lehigh University) observed six distinct GB complexions in Al_2O_3 (Fig. 16a) [17, 36]. These six GB complexions can be grouped into three classes:

- Complexion I (monolayer adsorption), Complexion II (clean/crystalline GBs) and Complexion VI (complete wetting) are well known.
- Complexion V (1-2 nm IGFs), discussed in §2.3, are also widely observed.
- Complexion III (bilayers) and Complexion IV (trilayers) can be considered to be derivative complexions of nanoscale IGFs (in the PI's opinion).

Dillon *et al.* used the concept of GB complexions to solve an outstanding scientific problem regarding the origin of abnormal grain growth [17] and "demystify the role of sintering aids" [16]. They further proposed a provocative concept of the "kinetic engineering of materials via utilizing GB complexions" [17].

In our AFOSR-YIP, we proposed a phenomenological model [3, 4, 37] for Dillon-Harmer complexions from an analogy to the colloidal theory (Fig. 16b). The basic concepts can be explained as follows. By reducing the temperature, or dopant activity, a quasi-liquid IGF should become thinner as opposing grains experience attractive forces. As the film thickness approaches atomic sizes, an oscillation in excess free energy versus film thickness arises, resulting in free energy minima when the thickness corresponds to an integer of atomic sizes. Consequently, additional stable GB complexions with discrete characteristic thicknesses form.

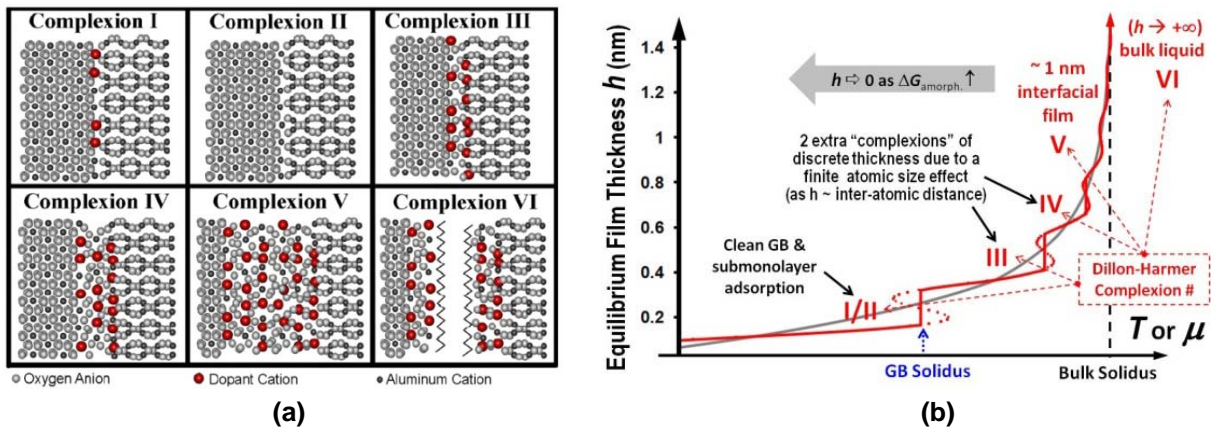


Fig. 16: (a) Schematic illustrations of six Dillon-Harmer Complexions in Al_2O_3 from Ref. [17]: *Complexion I* – the (Langmuir-McLean) monolayer adsorbates; *Complexion II* – clean/crystalline GBs; *Complexion III* – adsorption bilayers; *Complexion IV* – adsorption trilayers; *Complexion V* – ~ 1-2 nm thick IGFs; and *Complexion VI* – completely wetting films.

(b) A thermodynamic model developed in our AFOSR-YIP explaining the origins of the Dillon-Harmer complexions from atomic size effects [3, 4, 37]. Panel (b) is adapted from an AFOSR supported publication in *Appl. Phys. Lett.* [4].

4. Relevance to Aerospace Materials and Broader Impacts

Comprehending liquid-like GB “phases” is not only scientifically challenging, but also technologically important. In addition to critically affecting high-T properties and the materials fabrication processing, impurity-based GB “phases” can often retain upon cooling and affect low-T mechanical and physical properties. Table 2 lists selected technological relevance.

Table 2: Selected technological roles of impurity-based IGFs or analogous liquid-like GB complexions. This table was adapted from a recent critical review article written by the PI [1].

High-Temperature Material Properties	High- <i>T</i> strength, fracture behaviors, creep resistance, and oxidation of Si_3N_4 - and SiC - based structural ceramics	[54-62]
	Superplasticity of ZrO_2 -based ceramics	[63]
	WC-Co composites	[64]
	Refractory metal alloys	[2, 30]
Mechanical Properties and Chemical Stability	Toughness, strength, fatigue, and wear resistance of Si_3N_4 , SiC , and Al_2O_3 based structural ceramics	[65-71]
	Liquid metal embrittlement for <u>Ni</u> -Bi, <u>Cu</u> -Bi, and <u>Al</u> -Ga	[72-75]
	Corrosion of synroc	[76]
	GB embrittlement of <u>W</u> -Ni, <u>Cu</u> -Bi, and other systems	[42]
Solid-State Activated Sintering	<u>ZnO</u> - Bi_2O_3 ; <u>CeO</u> ₂ -CoO	[3, 4, 9, 44, 77, 78]
	<u>W</u> -Ni; <u>W</u> -Pd; <u>W</u> -Fe; <u>W</u> -Co; <u>Mo</u> -Ni	[2, 30, 79]
	<u>Ice</u> -impurities	[19, 20]
Abnormal Grain Growth	<u>Al</u> ₂ O ₃ -(Y_2O_3 + SiO_2); <u>Al</u> ₂ O ₃ -(other dopants)	[17, 31, 36]
	<u>Al</u> -Ga, <u>W</u> -Ni, and <u>ZnO</u> - Bi_2O_3	[80-83]
Electronic and Physical Properties	Ruthenate-based thick-film resistors	[84]
	<u>ZnO</u> - Bi_2O_3 based varistors	[29, 44, 85]
	(Ba, Sr) TiO_3 -based sensors and actuators	[86-91]
	Thermal conductivity in AlN	[92, 93]
	High- <i>T</i> _c superconductors	[94]

Controlling Microstructure: GB Diffusion vs. Migration:

Nanoscale IGFs often control densification [3, 4, 9, 44, 77, 78]. The presence of impurity-based liquid-like GB structures can also promote GB migration. This mechanism, which differs from the classical solute-drag model, has been observed for doped Al_2O_3 [17, 31, 36], ZnO- Bi_2O_3 [83], W-Ni [82], and Al-Ga [80, 81]. Dillon and Harmer [17, 36] further suggested that the existence of two or more GB complexions with significantly different GB mobilities will lead to detrimental abnormal grain growth. Practically, it is often desirable to achieve full densification with minimum grain growth (to make nanocrystalline or fine-grained materials) via pressure-less sintering (instead of using "brute force methods"). Here, we recommend using GB diagrams to predict a kinetic window where GB diffusion is significant, but GB migration is limited. This supports our **long-range scientific goal** of developing “GB diagrams” as a new tool for mechanism-informed materials design.

High-Temperature Structural Materials:

Quasi-liquid IGFs appear more frequently in high-temperature structural ceramics and refractory metals, because their formation will reduce the otherwise immense GB energies. In

general, the presence of impurity-based IGFs reduces the strength and creep resistance, but increase fracture toughness. Specifically:

- It is now well known that the control of IGFs is critical for achieving low- T toughness and yet optimizing high-temperature creep resistance for Si_3N_4 based ceramics [65, 67, 68].
- For SiC based ceramics, a recent study has demonstrated that drying/crystallizing IGFs is possible, leading to increased creep resistance at the expense of fracture toughness [95].
- IGFs also play critical roles in the mechanical properties and erosive wear behaviors of Al_2O_3 [70, 71] and the superplasticity of Y_2O_3 stabilized ZrO_2 [63].
- While the presence of IGFs generally reduce creep resistance, the formation of Complexion I in (at least) Y_2O_3 -doped Al_2O_3 significantly increases creep resistance [96].
- IGFs exist in WC-Co composites and affect their sintering and mechanical properties [64].
- IGFs with similar characteristics exist at hetero-phase interfaces (e.g., Al_2O_3 -TiN [97], BN-SiC [98], Al_2O_3 -metals [99]). They affect the mechanical properties of these composites.

Analogous IGFs in binary refractory metals (studied in this AFOSR-YIP) and in Mo-Si-B based multicomponent alloys (to be investigated in our new AFOSR project) serve as *relatively simple* model systems that can be used to establish and validate the basic high-temperature interfacial thermodynamic model. In future studies, we plan to extend the model to more complex ceramic materials (where electrostatic and vdW forces may complicate interfacial behaviors). We have a particular interest in analyzing ultra high temperature ceramics (UHTC).

GB-Controlled Oxidation, Corrosion and Embrittlement:

The presence of quasi-liquid IGFs may critically impact the GB-controlled oxidation and corrosion resistance. Recent studies have revealed the important role of nanoscale IGFs in the liquid metal embrittlement process [72-75]. Furthermore, impurity-based IGFs can often retain upon cooling. For metallic systems, they typically result in GB embrittlement. Here, using (abrupt) first-order GB transitions to design heat treatment procedures to alleviate such detrimental effects can be a potentially transformative approach.

Functional Ceramics:

IGFs can critically affect the tunable conductivities for ruthenate based thick-film resistors [84], non-linear I-V characteristics for ZnO - Bi_2O_3 based varistors [29, 85], functions of (Sr, Ba) TiO_3 based sensors and actuators [86-91], thermal conductivity of AlN substrates [92, 93], and critical currents of high T_c superconductors [94]. These functional ceramics also have a wide range of applications in the aerospace industry.

5. Executive Summary (Conclusions):

Impurity-based intergranular films or IGFs have been widely observed in structural and electronic ceramics, where they often control sintering, microstructural evolution (normal and abnormal grain growth), creep resistance, strength, fracture toughness, and some electronic properties. Under the support of this three-year AFOSR Young Investigator Program, we observed and systematically studied analogous quasi-liquid IGFs in W and Mo based binary refractory alloys.

Combined experimental and modeling studies of both W and Mo based systems unequivocally solved an outstanding scientific problem regarding the origin the solid-state activated sintering in refractory metals, which had puzzled the materials community for more than half a century. This study showed that the subsolidus enhanced densification is due to the increased mass transport in impurity-based liquid-like IGFs. These quasi-liquid IGFs are thermodynamic stabilized below the bulk solidus line, and their formation can be greatly promoted via minor addition of certain dopants (sintering aids). For the first time, quantitative predictions for the effectiveness of solid-state sintering aids have been made via a high-temperature interfacial thermodynamic model. This model quantitatively predicted the onset subsolidus activated sintering temperatures for Pd, Ni, Co, Fe, and Cu doped W. It systematically explained all major observations about activated sintering in Ni-doped Mo.

CalPhaD (Calculation of Phase Diagrams) methods were combined with a statistical thermodynamic model (a Miedema-type “macroscopic atom” model) to predict the thermodynamic stability of nanometer-thick undercooled liquid films sandwiched at grain boundaries (GBs). This model predicted that a “liquid precursor” could appear at GBs at as low as 60-85% of the bulk solidus lines in certain systems (such as Pd or Ni doped W). This model was further refined and validated via comparing with various experimental data. Furthermore, a phenomenological model was developed to consider atomic size effects, and this model produced a series of discrete “GB phases” with character similar to those six “complexions” observed by Dillon and Harmer.

We further proposed **a long-range scientific goal** of developing “GB diagrams” as a new materials science tool. Such GB diagrams can be used for **1)** optimizing fabrication pathways to utilize desired GB “phases” during processing to control microstructural evolution; **2)** designing heat treatment recipes to adjust GB structures to improve mechanical or physical properties; and **3)** forecasting GB-related high-temperature properties. Alternatively, failing to appreciate the presence of liquid-like GB structures at high temperatures can result in a significant variability in material fabrication and properties that may disqualify their successful aerospace applications.

Ni-doped Mo was selected for systematical evaluation via characterizing well-quenched specimens and thermodynamic modeling. In contrast to prior reports, we showed that the δ -NiMo phase does not wet Mo GBs in the solid state. In the solid-liquid two-phase region, the Ni-rich liquid wets Mo GBs completely. Furthermore, atomic-resolution HRTEM and AES characterization of well-quenched specimens unequivocally demonstrates that nanometer-thick quasi-liquid films persist at GBs into the single-phase region where the bulk liquid phase is no longer stable. To verify the correctness of a computed GB diagram for Ni-doped Mo, well-controlled sintering experiments were conducted to extract GB diffusivity as a function of the temperature and overall composition. These experimental results can be well explained from the

computed GB diagram. Specifically, major jumps in GB diffusivities occur at a distinct “GB solidus line”. In contrast, there are only moderate jumps in the effective GB diffusivities at the bulk solidus line where the bulk liquid appears, and there is no jump in measured GB diffusivity at the bulk solvus line below the bulk peritectic temperature. In pure Mo, the measured GB diffusivity increases with increasing temperature, which is well expected. However, with the addition of 0.5% Ni, the measured GB diffusivity appears to decrease with increasing temperature (although this composition lies in the single-phase region for all temperatures). This counterintuitive result can, in fact, be fully explained from the computed GB diagram. The modeling and experimental results illustrated that a GB can “solidify” with the increasing temperature at certain condition!

The formation of liquid-like GB structures is particularly important for high-temperature materials such as refractory metals and ceramics. This is because the GB energy typically scales with the melting temperature; greater GB energies can stabilize quasi-liquid IGFs to larger undercooling regions, thereby have greater impacts on microstructural evolution and high-temperature properties.

The feasibility and necessity of developing GB diagrams as new materials science tool for controlling microstructural evolution and forecasting high-temperature properties are proven by this AFOSR program on binary refractory alloys. There is a critical need to extend the developed high-temperature interfacial thermodynamic models, as well as the methods to compute GB diagrams, to multicomponent alloys to be practically useful. These models and methods should be further extended to more complex ceramic materials in future studies.

A List of People Involved in the Research Effort

- *Jian Luo*, the PI and project director (who received 1 summer month per year support and worked on modeling and design of experiments)
- *Xiaomeng (Jimmy) Shi*, a Ph.D. student (who received full support and worked solely on this AFOSR project on modeling and Mo-Ni experiments)
- *Jingou Yin*, a Ph.D. student (who received partial support and worked on sintering of W)
- *Archana Kayyar*, a Ph.D. student (who received partial support and worked on a regular solution model for GBs in binary alloys)

A Special Highlight (Student Award):

Jimmy Shi, a Ph.D. student supported by this AFOSR grant, was one of three students selected worldwide for a Diamond Award for 2009 Graduate Excellence in Material Sciences (GEMS) awards from the American Ceramic Society, Basic Science Division.

The GEMS awards are selected following a two-step process (written applications and oral presentations for the selected finalists at the annual Materials Science and Technology conference). Diamond awards are the highest catalog for the GEMS awards.

Please see the official awards page: <http://ceramics.org/acers-blog/2009-gems-awards/> as well as the following announcement in the 2010 January/February issue of *The American Ceramic Society Bulletin*.

The diagram illustrates the recognition of Jimmy Shi's achievement. On the left, a box labeled "Diamond Awards" contains his profile picture, name, and research title. A dashed arrow points from this box to the "2009 Graduate Excellence in Materials Science Awards" box on the right. This second box lists the Diamond and Sapphire award winners, with Shi's information appearing in the Diamond section. A second dashed arrow points from the "bulletin" image below to the same "2009 Graduate Excellence in Materials Science Awards" box, indicating that the award was also featured in the journal.

Diamond Awards

Jimmy Shi
Segregation, Disordering and Wetting at Molybdenum Grain Boundaries and Their Implications in Activated Sintering
Clemson University

2009 Graduate Excellence in Materials Science Awards (Presented by ACerS Basic Science Div.)

Diamond Awards

Jimmy Shi
Segregation, Disordering and Wetting at Molybdenum Grain Boundaries and Their Implications in Activated Sintering
Clemson University

Sapphire Awards

Weronika Walkosz
Interfaces of Silicon Nitride Ceramics: Direct Imaging and First-Principles Calculations
University of Illinois at Chicago

Hamid Azzizi-Alizamini
Phase Field Modeling of Austenite Formation from Ferrite-Carbide Aggregates
University of British Columbia

Craig Przybyla
Microstructure-Sensitive Extreme Value Probabilities of Fatigue in Advanced Engineering Alloys
Georgia Institute of Technology

Shaun Gittard
Two-Photon Polymerization of Organically Modified Ceramic Materials
North Carolina State University

Sapphire Awards

Sudhakar Shet
Bandgap-Reduced P-Type ZnO Films by Co-doping of Cu and Ga for Improving Photoelectro-chemical Response
New Jersey Institute of Technology

Yaodong Yang
Solid State Synthesis of Perovskite-Spinel Nanocomposites
Virginia Tech

Sarthak Havelia
Novel Approaches to the Growth of Epitaxial $BiMnO_3$ Thin Films
Carnegie Mellon University

bulletin
The American Ceramic Society Bulletin
89 [1], pp. 9 (Jan/Feb 2010)

A list of publications that acknowledged this AFOSR grant:

- X. Shi and J. Luo, "Grain Boundary Wetting and Prewetting in Ni-Doped Mo," *Applied Physics Letters*, 94, 251908 (2009).
- J. Luo and X. Shi, "Grain Boundary Disorder in Binary Alloys," *Applied Physics Letters*, 92, 101901 (2008).
- J. Luo, "Subsolidus Activated Sintering and Liquid-like Interface Complexions" (**invited review article**), *Current Opinion in Solid State and Materials Science*, 12, 81-88 (2008)
- J. Luo, "Stabilization of Nanoscale Quasi-Liquid Interfacial Films in Inorganic Materials: A Review and Critical Assessment" (**invited review article, image featured in the journal cover**), *Critical Reviews in Solid State and Materials Sciences*, 32, 67-109 (2007)
- V. K. Gupta, D. H. Yoon, H. M. Meyer III, and J. Luo, "Thin Intergranular Films and Solid-State Activated Sintering in Nickel-Doped Tungsten," *Acta Materialia*, 55, 3131-3142 (2007)
- J. Luo, S. J. Dillon and M.P. Harmer, "Interface-Stabilized Nanoscale Quasi-Liquid Films" (**invited overview**), *Microscopy Today*, 17 [4], 22-26, July 2009.
- Z. Wei, G. Zhang, H. Chen, J. Luo, R. Liu, and S. Guo, "A Simple Method for Evaluating Elastic Modulus of Thin Films by Nanoindentation," *Journal of Materials Research*, 24 [3], 777-791 (2009).
- R. H. French, V. A. Parsegian, R. Rodgornik, R. F. Rajiter, A. Jagota, J. Luo, D. Asthagiri, M. K. Chaudhury, Y.-M. Chiang, S. Granick, S. Kalinin, M. Kardar, R. Kjellander, D. C. Langreth, J. Lewis, S. Lustig, D. Wesolowski, J. Wetzlaufer, W.-Y. Ching, M. Finnis, F. Houlihan, O. A. von Lilienfeld, C. J. van Oss, and T. Zemb, "Long Range Interactions in Nanoscale Science" (**invited review article**), *Reviews of Modern Physics*, in press
- J. Luo, H. Qian, and X. Shi "Interface Stabilized Nanometer-Thick Disordered Films," a review chapter in the 2nd edition of *Encyclopedia of Nanoscience and Nanotechnology*, edited by H. S. Nalwa, American Scientific Publishers, in press.
- Xiaomeng Shi, "Grain Boundary Premelting and Activated Sintering in Binary Refractory Alloys," Ph.D. dissertation, Materials Science and Engineering, Clemson University, Clemson, South Carolina, USA, May 2010

A list of presentations that acknowledged this AFOSR grant:

- J. Luo, "Nanoscale Quasi-Liquid Interfacial Films: The Interplay of Premelting, Prewetting and Multilayer Adsorption," SYMPOSIUM: Computational Thermodynamics and Kinetics (organizers: Jeffrey J. Hoyt, Dallas Trinkle), 2010 TMS Annual Meeting & Exhibition, Seattle, WA, USA, February 14-18, 2010. (**Invited talk**)
- J. Luo, "Impurity-Based Nanoscale Quasi-Liquid Interfacial Films," Focused Session 3: Computational Design, Modeling, Simulation and Characterization of Ceramics and Composites, ICACC 10, The 34th International Conference and Exposition on Advanced Ceramics and Composites, Daytona Beach, Florida, January 24-29, 2010. (**Invited talk**)
- J. Luo, "Thermodynamic Stabilization of Subsolidus Quasi-Liquid Intergranular Films," SYMPOSIUM: Structural Transitions and Local Deformation Processes at and Near Grain

Boundaries, MS&T'09, Materials Science & Technology 2009 Conference, Pittsburgh, October 25-29. **(Invited talk)**

- X. Shi, J. Yin and J. Luo, "Segregation, Disorder and Wetting at Molybdenum Grain Boundaries and Their Implications in Activated Sintering," SYMPOSIUM: Powder Metallurgy Processing and Products, MS&T'09, Materials Science & Technology 2009 Conference, Pittsburgh, October 25-29. **(Student presentation)**
- J. Luo, "Liquid-Like Interfacial Complexions: Grain Boundaries vs. Free Surfaces and Metals vs. Ceramics," International Workshop on Interfaces, Bear Creek, PA, October 20-23, 2009. **(Invited talk)**
- M. P. Harmer and J. Luo, "Grain Boundary Complexions," ICCCI-3, The Third International Conference on the Characterization and Control of Interfaces for High Quality Advanced Materials, and Joining Technology for New Metallic Glasses and Inorganic Materials, Kurashiki, September 6-9, 2009. **(Invited talk, present for Prof. Martin Harmer)**
- J. Luo, "Nanoscale Liquid-Like Interfacial Films and Their Roles in Controlling Microstructural Evolution and High-Temperature properties," poster presentation, AFOSR Workshop on Aerospace Materials for Extreme Environments, St. Louis (Clayton), Missouri, August 3-5, 2009.
- J. Luo and X. Shi, "Grain boundary diagrams: from activated sintering to materials-by-design," The Role of Grain Boundary in Sintering, Symposium 1: Design, Modeling and Simulation of Ceramic Interfaces, The 8th Pacific Rim Conference on Ceramic and Glass Technology The 8th Pacific Rim Conference on Ceramic and Glass Technology, Vancouver, June 2, 2009. **(Invited talk)**
- J. Luo, H. Qian, and X. Shi, "Stabilization of Quasi-Liquid Interfacial Films: Adsorption, Disorder and Wetting," Ceramic Surfaces, Grain Boundaries and Interfaces, Materials and Technology 2008: Fundamentals and Characterization, Pittsburgh, PA, Oct 5-9, 2008. **(Invited talk)**
- J. Luo, "Interface-Stabilized Nanoscale Quasi-Liquid Films," The 5th International Conference on Advanced Materials and Processing (ICAMP-5), Harbin, China, September 2-5. **(Invited talk)**
- J. Luo, "Free-Surface Counterparts and Metallic Counterparts to Equilibrium Intergranular Films in Ceramics: Two Related Studies," Gordon Research Conference, Solid Studies in Ceramics, Proctor Academy, New Hampshire, August 10-15, 2008. **(Gordon Conference Invited Lecture)**
- J. Luo, "Subsolidus Quasi-Liquid Interfacial Films," International Workshop on Functionality of Interface (jointly sponsored by Max-Plank Institution and Chinese Academy of Science and co-organized by Dr. Hui Gu and Dr. Manfred Rühle), April 16-17, 2008, Shanghai, China. **(Invited talk)**
- J. Luo, H. Qian, X. Shi and V. K. Gupta, "Stabilization of Nanometer-Thick Subsolidus Quasi-Liquid Interfacial Films," oral presentation, Hume-Rothery Symposium - Nanoscale Phases, TMS 2008 Annual Meeting and Exhibition, New Orleans, LA, March 10, 2008. **(Invited talk)**

- X. Shi and J. Luo, "Segregation and Disorder at Tungsten Grain Boundaries in Well-Quenched Specimens," poster presentation, Materials and Technology 2008: Fundamentals and Characterization, Pittsburg, PA, Oct 5-9, 2008 (**Student presentation**)
- X. Shi and J. Luo, "Grain Boundary Wetting, Prewetting and Activated Sintering in Ni-Doped Mo," poster presentation, Gordon Research Conference, Solid Studies in Ceramics, Proctor Academy, New Hampshire, August 10-15, 2008 (**Student presentation**)
- J. Luo, "Nanoscale Quasi-Liquid Grain Boundary Films in Refractory Metals," AFOSR High Temperature Aerospace Materials program review meeting, May 12-16, 2008, Vienna, VA.
- J. Luo, X. Shi and V. K. Gupta, "A Quantitative Model for Solid-State Activated Sintering and Recent Observations," oral presentation, The 32nd International Conference & Exposition on Advanced Ceramics and Composites, Jan. 27-31, 2008
- X. Shi and J. Luo, "Solid-State Wetting and Activated Sintering in Ni-Doped Mo," oral presentation, International Symposium on Defects, Transport and Related Phenomena, Materials and Technology 2007: Fundamentals and Characterization, Detroit, MI, Sept 16-20, 2007. (**Student presentation**)
- X. Shi and J. Luo, "A Model for Grain Boundary Disorder and Solid-State Activated Sintering in Doped Tungsten," poster presentation, Gordon Research Conference, Solid Studies in Ceramics, Proctor Academy, New Hampshire, August 6-8 2007. (**Student presentation**)
- J. Luo, "Disordered Interfacial Films and Activated Sintering: Phenomenological Similarities among Ice, Ceramics and Refractory Metals," Refractory Metals 2007, 2007 TMS Annual Meeting and Exhibition, Orlando, FL, February 28, 2007
- J. Luo, "Liquid-Like Interfacial Complexions," Karlsruhe Institute of Technology, Institute for Ceramics in Mechanical Engineering, Karlsruhe, Germany, December 9, 2009. (**Invited seminar**)
- J. Luo, "Impurity-Based Quasi-liquid Interfacial Films: The Interplay of Premelting and Prewetting," The Materials Science Colloquium Lecture, the Max Planck Institute for Metals Research, Stuttgart, Germany, December 7, 2009. (**Invited colloquium lecture**)
- J. Luo, "Equilibrium Nanoscale Interfacial Films: Disorder, Adsorption and Wetting," Departmental Seminar, Lehigh University, Lehigh, PA, February 24, 2009. (**Invited seminar**)
- J. Luo, "Nanoscale Quasi-Liquid Interfacial Films," Harbin Institute of Technology, Harbin, China, September 5, 2008. (**Invited seminar**)
- J. Luo, "Interface-Stabilized Nanometer-Thick Disordered Films," University of South Carolina NanoCenter, April 4, 2007. (**Invited seminar**)
- J. Luo, "Interface-Stabilized Nanoscale Quasi-Liquid Films: from ice skating to materials by design," Mechanical Engineering Graduate Seminar Series, Louisiana State University, Baton Rouge, March 23, 2007. (**Invited seminar**)

References

- [1] Luo J. Stabilization of Nanoscale Quasi-Liquid Interfacial Films in Inorganic Materials: A Review and Critical Assessment. *Crit. Rev. Solid State Mater. Sci.* **2007**; 32:67.
- [2] Gupta VK, Yoon DH, Meyer III HM, Luo J. Thin Intergranular Films and Solid-State Activated Sintering in Nickel-Doped Tungsten. *Acta Mater.* **2007**; 55:3131.
- [3] Luo J. Liquid-Like Interface Complexion: From Activated Sintering to Grain Boundary Diagrams. *Current Opinion in Solid State and Materials Science* **2008**; 12:81.
- [4] Luo J, Shi XM. Grain Boundary Disorder in Binary Alloys. *Appl. Phys. Lett.* **2008** 92:101901
- [5] Sakidja R, Perepezko JH, Kim S, Sekido N. Phase Stability and Structural Defects in High-Temperature Mo-Si-B Alloys. *Acta Mater.* **2008**; 56:5223.
- [6] Dimiduk DM, Perepezko JH. Mo-Si-B Alloys: Developing a Revolutionary Turbine-Engine Material. *MRS Bulletin* **2003**; 28:639.
- [7] Middlemas MR, Cochran JK. Dense, Fine-Grain Mo-Si-B Alloys from Nitride-Based Reactions. *JOM* **2008**; 60:19.
- [8] Heilmayer M, Kruger M, Saage H, Rosler J, Mukherji D, Glatzel U, Volkl R, Huttner R, Eggeler G, Somsen C, Depka T, Christ HJ, Gorr B, Burk S. Metallic Materials for Structural Applications Beyond Nickel-Based Superalloys. *JOM* **2009**; 61:61.
- [9] Shi X, Luo J. Grain Boundary Wetting and Prewetting in Ni-Doped Mo. *Appl. Phys. Lett.* **2009**; 94:251908.
- [10] Yang Y, Chang YA. Thermodynamic Modeling of the Mo-Si-B System. *Intermetallics* **2005**; 13:121.
- [11] Jeurgens LPH, Sloof WG, Tichelaar FD, Mittemeijer EJ. Thermodynamic Stability of Amorphous Oxide Films on Metals: Application to Aluminum Oxide Films on Aluminum Substrates. *Phys. Rev. B* **2000**; 62:4707.
- [12] Reichel F, Jeurgens LPH, Mittemeijer EJ. The Thermodynamic Stability of Amorphous Oxide Overgrowths on Metals. *Acta Mater.* **2008**; 56:5894.
- [13] Luo J, Chiang Y-M. Wetting and Prewetting on Ceramic Surfaces. *Annu. Rev. Mater. Res.* **2008**; 38:227.
- [14] Fahrenholtz WG, Hilmas GE, Zhang SC, Zhu S. Pressureless Sintering of Zirconium Diboride: Particle Size and Additive Effects. *J. Am. Ceram. Soc.* **2008**; 91:1398.
- [15] Guo SQ, Kagawa Y, Nishimura T, Tanaka H. Pressureless Sintering and Physical Properties of Zrb2-Based Composites with Zrsi2 Additive. *Scripta Materialia* **2008**; 58:579.
- [16] Dillon SJ, Harmer MP. Demystifying the Role of Sintering Additives With "Complexion". *J. European Ceram. Soc.* **2008**; 28:1485.
- [17] Dillon SJ, Tang M, Carter WC, Harmer MP. Complexion: A New Concept for Kinetic Engineering in Materials Science. *Acta Mater.* **2007**; 55:6208.
- [18] Dash JG. Surface Melting. *Contemp. Phys.* **1989**; 30:89.
- [19] Dash JG, Fu H, Wetlaufer JS. The Premelting of Ice and Its Environmental Consequences. *Rep. Prog. Phys.* **1995**; 58:115.
- [20] Dash JG, Rempel AM, Wetlaufer JS. The Physics of Premelted Ice and Its Geophysical Consequences. *Rev. Mod. Phys.* **2006**; 78:695.
- [21] Rosenberg R. Why Is Ice Slippery? *Phys. Today* **2005**; 58(Dec.):50.
- [22] Hsieh TE, Balluffi RW. Experimental Study of Grain Boundary Melting in Aluminum. *Acta Metall.* **1989**; 37:1637.
- [23] Alsayed AM, Islam MF, Zhang J, Collings PJ, Yodh AG. Premelting at Defects within Bulk Colloidal Crystals. *Science* **2005**; 309:1207.
- [24] Cahn JW. Critical Point Wetting. *J. Chem. Phys.* **1977**; 66:3667.
- [25] Clarke DR. On the Equilibrium Thickness of Intergranular Glass Phases in Ceramic Materials. *J. Am. Ceram. Soc.* **1987**; 70:15.

[26] Clarke DR, Shaw TM, Philipse AP, Horn RG. Possible Electrical Double-Layer Contribution to the Equilibrium Thickness of Intergranular Glass Films in Polycrystalline Ceramics. *J. Am. Ceram. Soc.* **1993**; 76:1201.

[27] Bobeth M, Clarke DR, Pompe W. Diffuse Interface Description of Intergranular Films in Polycrystalline Ceramics. *J. Am. Ceram. Soc.* **1999**; 82:1537.

[28] Cannon RM, Rühle M, Hoffmann MJ, French RH, Gu H, Tomsia AP, Saiz E. Adsorption and Wetting Mechanisms at Ceramic Grain Boundaries. *Ceramic Transactions* **2000**; 118:427.

[29] Wang H, Chiang Y-M. Thermodynamic Stability of Intergranular Amorphous Films in Bismuth-Doped Zinc Oxide. *J. Am. Ceram. Soc.* **1998**; 81:89.

[30] Luo J, Gupta VK, Yoon DH, Meyer HM. Segregation-Induced Grain Boundary Premelting in Nickel-Doped Tungsten. *Appl. Phys. Lett.* **2005**; 87:231902.

[31] MacLaren I, Cannon RM, Gülgün MA, Voytovych R, Pogrion NP, Scheu C, Täffner U, Rühle M. Abnormal Grain Growth in Alumina: Synergistic Effects of Yttria and Silica. *J. Am. Ceram. Soc.* **2003**; 86:650.

[32] Tang M, Carter WC, Cannon RM. Grain Boundary Transitions in Binary Alloys. *Phys. Rev. Lett.* **2006**; 97:075502.

[33] French RH. Origin and Applications of London Dispersion Forces and Hamaker Constants in Ceramics. *J. Am. Ceram. Soc.* **2000**; 83:2117.

[34] Qian H, Luo J, Chiang Y-M. Anisotropic Wetting of ZnO by Bi_2O_3 with and without Nanometer-Thick Surficial Amorphous Films. *Acta Mater.* **2008**; 56:862.

[35] Tang M, Carter WC, Cannon RM. Diffuse Interface Model for Structural Transitions of Grain Boundaries. *Phys. Rev. B* **2006**; 73:024102.

[36] Dillon SJ, Harmer MP. Multiple Grain Boundary Transitions in Ceramics: A Case Study of Alumnia. *Acta Mater.* **2007**; 55:5247.

[37] Luo J, Dillon SJ, Harmer MP. Interface-Stabilized Nanoscale Quasi-Liquid Films. *Microscopy Today* **2009**; 17:22.

[38] Creuze J, Berthier F, Tetot R, Legrand B. Wetting and Structural Transition Induced by Segregation at Grain Boundaries: A Monte Carlo Study. *Phys. Rev. Lett.* **2001**; 86:5735.

[39] Udler D, Seidman DN. Congruent Phase Transition at a Twist Boundary Induced by Solute Segregation. *Phys. Rev. Lett.* **1996**; 77:3379.

[40] Yan Y, Chisholm MF, Duscher G, Maiti A, Pennycook SJ, Pantelides ST. Impurity-Induced Structural Transformation of a Mgo Grain Boundary. *Phys. Rev. Lett.* **1998**; 81:3675.

[41] Shao R, Chisholm MF, Duscher G, Bonnell DA. Low-Temperature Resistance Anomaly at SrTiO_3 Grain Boundaries: Evidence for an Interface-Induced Phase Transition. *Phys. Rev. Lett.* **2005**; 95.

[42] Straumal BB, Baretzky B. Grain Boundary Phase Transitions and Their Influence on Properties of Polycrystals. *Interf. Sci.* **2004**; 12:147.

[43] Coble RL, Cannon RM. Current Paradigms in Powder Processing. In: Palmour III H, Davis RF, Hare TM, editors. *Processing of Crystalline Ceramics*. NY: Plenum P., **1978**. p.151.

[44] Luo J, Wang H, Chiang Y-M. Origin of Solid State Activated Sintering in Bi_2O_3 -Doped ZnO. *J. Am. Ceram. Soc.* **1999**; 82:916.

[45] German RM. Activated Sintering of Refractory Metals by Transition Metal Additions. *Rev. Powder Metall. Phys. Ceram.* **1982**; 2:9.

[46] German RM. Diffusional Activated Sintering - Densification, Microstructure and Mechanical Properties. *Prog. Powder Met.* **1984**; 39:243.

[47] German RM. The Identification of Enhanced Sintering Systems through Phase Diagrams. *Mod. Dev. Powder Met.* **1985**; 15:253.

[48] German RM, Munir ZA. Enhanced Low-Temperature Sintering of Tungsten. *Metall. Trans.* **1976**; 7A:1873.

[49] Brophy JH, Shepard LA, Wulff J. The Nickel-Activated Sintering of Tungsten. In: Leszynski W, editor. *Powder Metallurgy*. Interscience, **1961**. p.113.

[50] Hwang KS, Huang HS. Identification of the Segregation Layer and Its Effects on the Activated Sintering and Ductility of Ni-Doped Molybdenum. *Acta Mater.* **2003**; 51:3915.

[51] German RM, Munir ZA. Hetero-Diffusion Model for Activated Sintering of Molybdenum. *J. Less-Common Metals* **1978**; 58:61.

[52] Hayden HW, Brophy JH. Activated Sintering of Tungsten with Group VIII Elements. *J. Electrochemical Soc.* **1963**; 110:805.

[53] Penisson JM, Vystavel T. Wetting of Molybdenum Grain Boundaries by Nickel: Effect of the Boundary Structure and Energy. *Acta Mater.* **2000**; 48:3303.

[54] Jin Q, Wilkinson DS, Weatherly GC. High-Resolution Electron Microscopy Investigation of Viscous Flow Creep in a High-Purity Silicon Nitride. *J. Am. Ceram. Soc.* **1999**; 82:1492.

[55] Tanaka I, Igashira K, Okamoto T, Niihara K, Cannon RM. High-Temperature Fracture Mechanism of Low-Ca Doped Silicon Nitride. *J. Am. Ceram. Soc.* **1995**; 78:673.

[56] Guo S, Hirosaki N, Yamamoto Y, Nishimura T, Kitami Y, Mitomo M. Microstructural Characterization and High-Temperature Strength of Hot-Pressed Silicon Nitride Ceramics with Lu_2O_3 Additives. *Philos. Mag. Lett.* **2003**; 83:357.

[57] Stemmer S, Roebben G, van der Biest O. Evolution of Grain Boundary Films in Liquid Phase Sintered Silicon Nitride During High-Temperature Testing. *Acta Mater.* **1998**; 46:5599.

[58] Chen D, Sixta ME, Zhang X-F, DeJonghe LC, Ritchie RO. Role of the Grain Boundary Phase on the Elevated-Temperature Strength, Toughness, Fatigue and Creep Resistance of Silicon Carbide Sintered with Al, B, and C. *Acta Mater.* **2000**; 48:4599.

[59] Pezzotti G, Kleebe H-J, Okamoto K, Ota K. Structure and Viscosity of Grain Boundary in High-Purity SiAlON Ceramics. *J. Am. Ceram. Soc.* **2000**; 83:2549.

[60] Pezzotti G, Kleebe H-J, Ota K. Grain-Boundary Viscosity of Polycrystalline Silicon Carbides. *J. Am. Ceram. Soc.* **1998**; 81:3293.

[61] Pezzotti G, Wakasugi T, Nishida T, Ota R, Kleebe H-J, Ota K. Chemistry and Inherent Viscosity of Glasses Segregated at Grain Boundaries of Silicon Nitride and Silicon Carbide Ceramics. *J. Non-Crystalline Solids* **2000**; 271:79.

[62] Cinibulk MK, Kleebe H-J. Effects of Oxidation on Intergranular Phases in Silicon Nitride Ceramics. *J. Mater. Sci.* **1993**; 28:5775.

[63] Primdahl S, Tholen A, Langdon TG. Microstructural Examination of a Superplastic Yttria-Stabilized Zirconia: Implications for the Superplasticity Mechanism. *Acta Metall. Mater.* **1995**; 43:1211.

[64] Jayaram V, Sinclair R. Detection of Thin Intergranular Cobalt Layers in WC-Co Composites by Lattice Imaging. *J. Am. Ceram. Soc.* **1983**; 66:C137.

[65] Becher PF, Painter GS, Sun EY, Hsueh CH, Lance MJ. The Importance of Amorphous Intergranular Films in Self-Reinforced Si_3N_4 Ceramics. *Acta Mater.* **2000**; 48:4493.

[66] Kleebe H-J. SiC and Si_3N_4 Materials with Improved Fracture Resistance. *J. European Ceram. Soc.* **1992**; 10:151.

[67] Becher PF, Painter GS, Lance MJ, Li S, Ikuhara Y. Direct Observations of Debonding of Reinforcing Grains in Silicon Nitride Ceramics Sintered with Yttria Plus Alumina Additives. *J. Am. Ceram. Soc.* **2005**; 88:1222.

[68] Becher PF, Sun EY, Hsueh CH, Painter GS, More KL. Role of Intergranular Films in Toughened Ceramics. *Key Eng. Mater.* **2000**; 175-176:97.

[69] Chen D, Zhang X-F, Ritchie RO. Effects of Grain-Boundary Structure on the Strength, Toughness, and Cyclic-Fatigue Properties of a Monolithic Silicon Carbide. *J. Am. Ceram. Soc.* **2000**; 83:2079.

[70] Brydson R, Twigg PC, Loughran F, Riley FL. Influence of Cao-Sio2 Ratio on the Chemistry of Intergranular Films in Liquid-Phase Sintered Alumina and Implications for Rate of Erosive Wear. *J. Mater. Res.* **2001**; 16:652.

[71] Svancarek P, Galusek D, Calvert C, Loughran F, Brown A, Brydson R, Riley F. A Comparison of the Microstructure and Mechanical Properties of Two Liquid Phase Sintered Aluminas Containing Different Molar Ratios of Calcia-Silica Sintering Additives. *J. European Ceram. Soc.* **2004**; 24:3453.

[72] Wolski K, Laporte V, Marie N, Biscondi M. About the Importance of Nanometer-Thick Intergranular Penetration in the Analysis of Liquid Metal Embrittlement. *Interf. Sci.* **2001**; 9:183.

[73] Marie N, Wolski K, Biscondi M. Intergranular Penetration and Embrittlement of Solid Nickel through Bismuth Vapour Condensations at 700°C. *J. Nucl. Mater.* **2001**; 296:282.

[74] Marie N, Wolski K, Biscondi M. Grain Boundary Penetration of Nickel by Liquid Bismuth as a Film of Nanometeric Thickness *Script Mater.* **2000**; 43:943.

[75] Pereiro-López E, Ludwig W, Bellet D, Cloetens P, Lemaignan C. Direct Evidence of Nanometric Invasionlike Grain Boundary Penetration in the Al/Ga System. *Phys. Rev. Lett.* **2005**; 95:215501.

[76] Cooper JA, Cousens DR, Myhra S, Smart RSC. Intergranular Films and Pore Surfaces in Synroc C: Structure, Composition, Dissolution Characteristics. *J. Am. Ceram. Soc.* **1986**; 69:347.

[77] Jud E, Huwiler CB, Gauckler LJ. Sintering Analysis of Undoped and Cobalt Oxide Doped Ceria Solid Solutions. *J. Am. Ceram. Soc.* **2005**; 88:3013.

[78] Jud E, Zhang Z, Sigle W, Gauckler LJ. Microstructure of Cobalt Oxide Doped Sintered Ceria Solid Solutions. *J. Electroceramics* **2006**; 16:191.

[79] Gupta VK, Yoon DH, Luo J, Meyer III HM. Preliminary Results of Activated Sintering Mechanism and Grain Boundary Prewetting/ Premelting in Nickel-Doped Tungsten. In: R. M. Lane MZH, S. Lu, editor. *Ceramic Nanomaterials and Nanotechnology IV*, vol. 172: The American Ceramic Society, **2005**. p.159.

[80] Gottstein G, Molodov DA. Grain Boundary Migration in Metals: Recent Developments. *Interf. Sci.* **1998**; 6:7.

[81] Weygand D, Brechet Y, Rabkin E, Straumal B, Gust W. Solute Drag and Wetting of a Grain Boundary *Philos. Mag. Lett.* **1997**; 76:133.

[82] Moon I-H, Kim K-Y, Oh S-T, Suk M-J. Nickel-Enhanced Grain Growth in Tungsten Wire. *J. Alloys Compd.* **1993**; 201:129.

[83] Choi JH, Hwang N-M, Kim DY. Pore-Boundary Separation Behavior During Sintering of Pure and Bi_2O_3 -Doped Zno Ceramics. *J. Am. Ceram. Soc.* **2001**; 84:1398.

[84] Chiang Y-M, Silverman LA, French RH, Cannon RM. Thin Glass Film between Ultrafine Conductor Particles in Thick-Film Resistors. *J. Am. Ceram. Soc.* **1994**; 77:143.

[85] Chiang Y-M, Wang H, Lee J-R. Hrem and Stem of Intergranular Films at Zinc Oxide Varistor Grain Boundaries. *J. Microscopy* **1998**; 191:275.

[86] Choi S-Y, Kang S-JL. Sintering Kinetics by Structural Transition at Grain Boundaries in Barium Titanate. *Acta Mater.* **2004**; 52:2937.

[87] Choi S-Y, Yoon D-Y, Kang S-JL. Kinetic Formation and Thickening of Intergranular Amorphous Films at Grain Boundaries in Barium Titanate. *Acta Mater.* **2004**; 52:3721.

[88] Kienzle O, Hutt S, Ernst F, Rühle M. Grain Boundaries in Strontium Titanate. *Ceram. Trans.* **2000**; 118:215.

[89] Chung S-Y, Kang S-JL. Intergranular Amorphous Films and Dislocations-Promoted Grain Growth in SrTiO_3 . *Acta Mater.* **2003**; 51:2345.

[90] Ernst F, Kienzle O, Rühle M. Structure and Composition of Grain Boundaries in Ceramics. *J. European Ceram. Soc.* **1999**; 19:665.

[91] Lee J-H, Kim J-J, Wang H, Cho S-H. Observation of Intergranular Films in BaB_2O_4 -Added BaTiO_3 Ceramics. *J. Mater. Res.* **2000**; 15:1600.

[92] Nakano H, Watari K, Urabe K. Grain Boundary Phase in Aln Ceramics Fired under Reducing N_2 Atmosphere with Carbon. *J. European Ceram. Soc.* **2003**; 23:1761.

[93] Callahan DL, Thomas G. Impurity Distribution in Polycrystalline Aluminum Nitride Ceramics *J. Am. Ceram. Soc.* **1990**; 73:2167.

[94] Ramesh R, Green SM, Thomas G. Microstructure Property Relations in the Bi(Pb)-Sr-Ca-Cu-O Ceramic Superconductors. In: Narlikar A, editor. *Studies of High Temperature Superconductors: Advances in Research and Applications*, vol. 5. Commack, NY: Nova Science Publ., **1990**. p.363.

[95] Zhang X-F, Sixta ME, DeJonghe LC. Grain Boundary Evolution in Hot-Pressed ABC-SiC. *J. Am. Ceram. Soc.* **2000**; 83:2813.

[96] Buban JP, Matsunaga K, Chen J, Shibata N, Ching WY, Yamamoto T, Ikuhara Y. Grain Boundary Strengthening in Alumina by Rare Earth Impurities. *Science* **2006**; 311:212.

[97] Schmid HK. Identification of Intergranular Phases in Ceramic Nanocomposites. *J. Microscopy* **1999**; 194:192.

[98] Knowles KM, Turan S. Boron Nitride-Silicon Carbide Interphase Boundaries in Silicon Nitride-Silicon Carbide Particulate Composites. *J. European Ceram. Soc.* **2002**; 22:1587.

[99] Avishai A, Kaplan WD. Intergranular Films at Metal-Ceramic Interfaces Part II – Calculation of Hamaker Coefficient. *Acta Mater.* **2005**; 53:1571.

[100] Majumdar S, Kapoor R, Raveendra S, Sinha H, Samajdar I, Bhargava P, Chakravarthy JK, Sharma IG, Suri AK. A Study of Hot Deformation Behavior and Microstructural Characterization of Mo-TZM Alloy. *J. Nucl. Mater.* **2009**; 385:545.

[101] Fan JL, Lu MY, Cheng HC, Tian JM, Huang BY. Effect of Alloying Elements Ti, Zr on the Property and Microstructure of Molybdenum. *International J. Refractory Metals & Hard Materials* **2009**; 27:78.

[102] El-Genk MS, Tournier JM. A Review of Refractory Metal Alloys and Mechanically Alloyed-Oxide Dispersion Strengthened Steels for Space Nuclear Power Systems. *J. Nucl. Mater.* **2005**; 340:93.

[103] Gorynin IV, Ignatov VA, Rybin VV, Fabritsiev SA, Kazakov VA, Chakin VP, Tsykanov VA, Barabash VR, Prokofyev YG. Effects of Neutron-Irradiation on Properties of Refractory-Metals. *J. Nucl. Mater.* **1992**; 191:421.

[104] Singh BN, Evans JH, Horsewell A, Toft P, Muller GV. Effects of Neutron Irradiation on Microstructure and Deformation Behaviour of Mono- and Polycrystalline Molybdenum and Its Alloys. *J. Nucl. Mater.* **1998**; 258:865.

[105] Kurishita H, Kitsunai Y, Shibayama T, Kayano H, Hiraoka Y. Development of Mo Alloys with Improved Resistance to Embrittlement by Recrystallization and Irradiation. *J. Nucl. Mater.* **1996**; 233:557.

[106] Schneibel JH, Kramer MJ, Easton DS. A Mo-Si-B Intermetallic Alloy with a Continuous Alpha-Mo Matrix. *Script Mater.* **2002**; 46:217.

[107] Schneibel JH, Ritchie RO, Kruzic JJ, Tortorelli PF. Optimizaton of Mo-Si-B Intermetallic Alloys. *Metall. Mater. Trans. A* **2005**; 36A:525.

[108] Meyer MK, Akinc M. Isothermal Oxidation Behavior of Mo-Si-B Intermetallics at 1450 Degrees C. *J. Am. Ceram. Soc.* **1996**; 79:2763.

[109] Meyer MK, Thom AJ, Akinc M. Oxide Scale Formation and Isothermal Oxidation Behavior of Mo-Si-B Intermetallics at 600-1000 Degrees C. *Intermetallics* **1999**; 7:153.

[110] Nunes CA, Sakidja R, Dong Z, Perepezko JH. Liquidus Projection for the Mo-Rich Portion of the Mo-Si-B Ternary System. *Intermetallics* **2000**; 8:327.

[111] Ito K, Kumagai M, Hayashi T, Yamaguchi M. Room Temperature Fracture Toughness and High Temperature Strength of T_2/Mo_{ss} and $(Mo,Nb)_{ss}/T_1/T_2$ Eutectic Alloys in the Mo-Si-B System. *Script Mater.* **2003**; 49:285.

[112] Choe H, Schneibel JH, Ritchie RO. On the Fracture and Fatigue Properties of Mo-Mo₃Si-Mo₅SiB₂ Refractory Intermetallic Alloys at Ambient to Elevated Temperatures. *Metall. Mater. Trans. A* **2003**; 34:225.

[113] Schneibel JH, Liu CT, Easton DS, Carmichael CA. Microstructure and Mechanical Properties of Mo-Mo₃Si-Mo₅SiB₂ Silicides. *Mater. Sci. Eng., A* **1999**; 261:78.

[114] Supatarawanich V, Johnson DR, Liu CT. Effects of Microstructure on the Oxidation Behavior of Multiphase Mo-Si-B Alloys. *Mater. Sci. Eng.* **2003**; 344:328.

[115] Sakidja R, Park JS, Hamann J, Perepezko JH. Synthesis of Oxidation Resistant Silicide Coatings on Mo-Si-B Alloys. *Script Mater.* **2005**; 53:723.

[116] Sakidja R, Perepezko JH. Phase Stability and Alloying Behavior in the Mo-Si-B System. *Metall. Mater. Trans. A* **2005**; 36A:507.

[117] Sakidja R, Perepezko JH. Alloying and Microstructure Stability in the High-Temperature Mo-Si-B System. *J. Nucl. Mater.* **2007**; 366:407.

[118] Jehanno P, Heilmair M, Kestler H, Boning M, Venskutonis A, Bewlay B, Jackson M. Assessment of a Powder Metallurgical Processing Route for Refractory Metal Silicide Alloys. *Metall. Mater. Trans. A* **2005**; 36A:515.

[119] Mandal P, Thom AJ, Kramer MJ, Behrani V, Akinc M. Oxidation Behavior of Mo-Si-B Alloys in Wet Air. *Mater. Sci. Eng. A* **2004**; 371:335.

[120] Katrych S, Grytsiv A, Bondar A, Rogl P, Velikanova T, Bohn M. Structural Materials: Metal-Silicon-Boron - on the Melting Behavior of Mo-Si-B Alloys. *J. Alloys Compd.* **2002**; 347:94.

[121] Hayashi T, Ito K, Ihara K, Fujikura M, Yamaguchi M. Creep of Single Crystalline and Polycrystalline T-2 Phase in the Mo-Si-B System. *Intermetallics* **2004**; 12:699.

[122] Nomura N, Suzuki T, Yoshimi K, Hanada S. Microstructure and Oxidation Resistance of a Plasma Sprayed Mo-Si-B Multiphase Alloy Coating. *Intermetallics* **2003**; 11:735.

[123] Jehanno P, Heilmaier M, Saage H, Boning M, Kestler H, Freudenberger J, Drawin S. Assessment of the High Temperature Deformation Behavior of Molybdenum Silicide Alloys. *Mater. Sci. Eng., A* **2007**; 463:216.

[124] Mitra R, Srivastava AK, Prasad NE, Kumari S. Microstructure and Mechanical Behaviour of Reaction Hot Pressed Multiphase Mo-Si-B and Mo-Si-B-Al Intermetallic Alloys. *Intermetallics* **2006**; 14:1461.

[125] Jain P, Alur AP, Kumar KS. High Temperature Compressive Flow Behavior of a Mo-Si-B Solid Solution Alloy. *Script Mater.* **2006**; 54:13.

[126] Paswan S, Mitra R, Roy SK. Isothermal Oxidation Behaviour of Mo-Si-B and Mo-Si-B-Al Alloys in the Temperature Range of 400-800 Degrees C. *Mater. Sci. Eng. A* **2006**; 424:251.

[127] Paswan S, Mitra R, Roy SK. Oxidation Behaviour of the Mo-Si-B and Mo-Si-B-Al Alloys in the Temperature Range of 700-1300 Degrees C. *Intermetallics* **2007**; 15:1217.

[128] Behrani V, Thom AJ, Kramer MJ, Akinc M. Microstructure and Oxidation Behavior of Nb-Mo-Si-B Alloys. *Intermetallics* **2006**; 14:24.

[129] Yamauchi A, Yoshimi K, Kurokawa K, Hanada S. Synthesis of Mo-Si-B in Situ Composites by Mechanical Alloying. *J. Alloys Compd.* **2007**; 434:420.

[130] Thom AJ, Kramer MJ, Mandal P, Akinc M. Wet Air and Simulated Combustion Gas Exposures of Mo-Si-B Alloys. *Script Mater.* **2005**; 53:915.

[131] Kruzic JJ, Schneibel JH, Ritchie RO. Ambient- to Elevated-Temperature Fracture and Fatigue Properties of Mo-Si-B Alloys: Role of Microstructure. *Metall. Mater. Trans. A* **2005**; 36A:2393.

[132] Wang F, Shan AD, Dong XP, Wu JS. Microstructure and Oxidation Resistance of Laser-Remelted Mo-Si-B Alloy. *Script Mater.* **2007**; 56:737.

[133] Wang F, Shan AD, Dong XP, Wu JS. Microstructure and Oxidation Behavior of Directionally Solidified Mo-Mo₅SiB₂ (T2)-Mo₃Si Alloys. *J. Alloys Compd.* **2008**; 462:436.

[134] Wang F, Shan M, Shan AD, Wu JS. Microstructure and Oxidation Behavior of Mo-Si-B Ternary Silicide. *Rare Metal Materials and Engineering* **2006**; 35:1920.

[135] Liu Y, Kramer MJ, Thom AJ, Akinc M. Oxidation Behavior of Multiphase Nb-Mo-Si-B Intermetallics. *Metall. Mater. Trans. A* **2005**; 36A:601.

[136] Krueger M, Franz S, Saage H, Heilmaier M, Schneibel JH, Jehanno P, Boning M, Kestler H. Mechanically Alloyed Mo-Si-B Alloys with a Continuous Alpha-Mo Matrix and Improved Mechanical Properties. *Intermetallics* **2008**; 16:933.

[137] Li Z, Peng LM. Ultra-High Temperature Mo-Si-B Alloys - Synthesis, Microstructural and Mechanical Characterization. *Mater. Lett.* **2008**; 62:2229.

[138] Middlemas MR, Cochran JK. Oxidation Behavior of Mo-Si-B Alloys Produced by Reaction Synthesis. *TMS 2008 Supplemental Proceedings*, **2008**. vol. 3, p.177.

[139] Middlemas MR, Cochran JK. A Nitride Based Reaction for the Formation of a Three Phase Mo-Si-B Alloy. *Advanced Metallic Composite and Alloys for High Performance Applications* (TMS 2008, ed. A. Pandey et al.), **2007**. p.63.

[140] Rockett C, Middlemas M, Cochran J. Flexure Strength of Mo-Si-B Alloys Reacted from Mo, Si₃N₄, and BN. *Advanced Metallic Composite and Alloys for High Performance Applications* (TMS 2008, ed. A. Pandey et al.), **2007**. p.95.

[141] Middlemas MR, Cochran JK. Oxidation Behavior of Mo-Si-B Alloys Produced by Reaction Synthesis. *TMS 2008 Supplemental Proceedings*, **2008**. vol. 3., p.177.

[142] Rosales I, Schneibel JH. Stoichiometry and Mechanical Properties of Mo₃Si. *Intermetallics* **2000**; 8:885.

[143] Kruzic JJ, Schneibel JH, Ritchie RO. Fracture and Fatigue Resistance of Mo-Si-B Alloys for Ultrahigh-Temperature Structural Applications. *Script Mater.* **2004**; 50:459.

[144] Alur AP, Chollacoop N, Kumar KS. High-Temperature Compression Behavior of Mo-Si-B Alloys. *Acta Mater.* **2004**; 52:5571.

[145] Alur AP, Chollacoop N, Kumar KS. Creep Effects on Crack Growth in a Mo-Si-B Alloy. *Acta Mater.* **2007**; 55:961.

[146] Jehanno P, Heilmaier M, Saage H, Heyse H, Boning M, Kestler H, Schneibel JH. Superplasticity of a Multiphase Refractory Mo-Si-B Alloy. *Script Mater.* **2006**; 55:525.

[147] Parthasarathy TA, Mendiratta MG, Dimiduk DM. Oxidation Mechanisms in Mo-Reinforced Mo₅Si₂(T-2)-Mo₃Si Alloys. *Acta Mater.* **2002**; 50:1857.

[148] de Boer FR, Boom R, Mattens WCM, Miedema AR, Niessen AK. *Cohesion in Metals: Transition Metals Alloys*. Amsterdam: North-Holland, **1988**.

[149] Benedictus R, Böttger A, Mittemijer EJ. Thermodynamic Model for Solid-State Amorphization in Binary Systems at Interfaces and Grain Boundaries. *Phys. Rev. B* **1996**; 54:9109.

[150] Shimizu I, Takei Y. Temperature and Compositional Dependence of Solid-Liquid Interfacial Energy: Application of the Cahn-Hilliard Theory. *Physica B-Condensed Matter* **2005**; 362:169.

[151] Shimizu I, Takei Y. Thermodynamics of Interfacial Energy in Binary Metallic Systems: Influence of Adsorption on Dihedral Angles. *Acta Mater.* **2005**; 53:811.

[152] Kattner UR. The Thermodynamic Modeling of Multicomponent Phase Equilibria. *JOM* **1997**; 49:14.

[153] Kobayashi R, Warren JA, Carter WC. A Continuum Model of Grain Boundaries. *Phys. D* **2000**; 140:141.

[154] Zhang H, Srolovitz DJ, Douglas JF, Warren JA. Grain Boundaries Exhibit the Dynamics of Glass-Forming Liquids. *Proceedings of the National Academy of Sciences of the United States of America* **2009**; 106:7735.

[155] Lavine MC. Of Grains and Glasses. *Science* **2009**; 324:858.

[156] Keblinski P, Phillpot SR, Wolf D. Thermodynamic Criterion for the Stability of Amorphous Intergranular Films in Covalent Materials. *Phys. Rev. Lett.* **1996**; 77:2965.

[157] Keblinski P, Phillpot SR, Wolf D, Gleiter H. On the Thermodynamic Stability of Amorphous Intergranular Films in Covalent Materials. *J. Am. Ceram. Soc.* **1997**; 80:717.

[158] Blaine DC, Park SJ, German RM. Linearization of Master Sintering Curve. *J. Am. Ceram. Soc.* **2009**; 92:1403.

[159] Park SJ, Suri P, Olevsky E, German RM. Master Sintering Curve Formulated from Constitutive Models. *J. Am. Ceram. Soc.* **2009**; 92:1410.

[160] Garg P, Park SJ, German RM. Effect of Die Compaction Pressure on Densification Behavior of Molybdenum Powders. *International J. Refractory Metals & Hard Materials* **2007**; 25:16.

[161] Blaine DC, Park SJ, Suri P, German RM. Application of Work-of-Sintering Concepts in Powder Metals. *Metall. Mater. Trans. A* **2006**; 37A:2827.

[162] Park SJ, Martin JM, Guo JF, Johnson JL, German RM. Densification Behavior of Tungsten Heavy Alloy Based on Master Sintering Curve Concept. *Metall. Mater. Trans. A* **2006**; 37A:2837.

[163] Blaine DC, Guroskik JD, Park SJ, Heaney DF, German RM. Master Sintering Curve Concepts as Applied to the Sintering of Molybdenum. *Metall. Mater. Trans. A* **2006**; 37A:715.

[164] Kemp PB, German RM. Grain-Growth in Liquid-Phase-Sintered W-Mo-Ni-Fe Alloys. *J. Less-Common Metals* **1991**; 175:353.

[165] German RM, Labombard CA. Sintering Molybdenum Treated with Ni, Pd and Pt. *International J. Powder Metall.* **1982**; 18:147.

[166] Kim GS, Kim HG, Kim DG, Oh ST, Suk MJ, Do Kim Y. Densification Behavior of Mo Nanopowders Prepared by Mechanochemical Processing. *J. Alloys Compd.* **2009**; 469:401.

[167] Nizhenko VI, Petrishchev VY, Skorokhod VV. Densification Kinetics of Mo-Ni-Sn Composites in Liquid-Phase Sintering. *Powder Metallurgy and Metal Ceramics* **2008**; 47:288.

[168] Kim Y. Consolidation Behavior and Hardness of P/M Molybdenum. *Powder Technology* **2008**; 186:213.

[169] Chen I-W, Wang XH. Sintering Dense Nanocrystalline Ceramics without Final Stage Grain Growth. *Nature* **2000**; 404:168.

[170] Tang M, Ramos AV, Jud E, Chung SY, Gautier-Soyer M, Cannon RM, Carter WC, Chiang YM. Nanometer-Scale Wetting of the Silicon Surface by Its Equilibrium Oxide. *Langmuir* **2008**; 24:1891.

- [171] Sturm D, Heilmaier M, Schneibel JH, Jehanno P, Skrotzki B, Saage H. The Influence of Silicon on the Strength and Fracture Toughness of Molybdenum. *Mater. Sci. Eng., A* **2007**; 463:107.
- [172] Heilmaier M. et al., MRS Fall Meeting. Boston, MA, **2006**.
- [173] Mishin Y, Boettinger WJ, Warren JA, McFadden GB. Thermodynamics of Grain Boundary Premelting in Alloys. I. Phase-Field Modeling. *Acta Mater.* **2009**; 57:3771.
- [174] Alfthan Sv, Kaski K, Sutton AP. Molecular Dynamics Simulations of Temperature-Induced Structural Transitions at Twist Boundaries in Silicon. *Phys. Rev. B* **2007**; 76:245317.
- [175] Zhang XF, Wang RM. Short-Range Order in Nanoscale Amorphous Intergranular Films in Liquid-Phase Sintered Silicon Carbide. *Appl. Phys. Lett.* **2006**; 89:211902.
- [176] Divinski S, Lohmann M, Herzig C, Straumal B, Baretzky B, Gust W. Grain Boundary Melting Phase Transition in the Cu-Bi System. *Phys. Rev. B* **2005**; 71:104104.
- [177] Straumal BB, Noskovich OI, Semenov VN, Shvindlerman LS, Gust W, Predel B. Premelting Transition on 38<100> Tilt Grain Boundaries in (Fe- 10 At. % Si)-Zn Alloys,. *Acta Metall. Mater.* **1992**; 40:795.
- [178] Rabkin EI, Semenov VN, Shvindlerman LS, Straumal BB. Penetration of Tin and Zinc Along Tilt Grain Boundaries 43° [100] in Fe-5 At.% Si Alloy: Premelting Phase Transition? *Acta Metall. Mater.* **1991**; 39:627.
- [179] Noskovich OI, Rabkin EI, Semenov VN, Straumal BB, Shvindlerman LS. Wetting and Premelting Phase Transitions in 38° [100] Tilt Grain Boundary in (Fe-12 At.% Si)-Zn Alloy in the Vicinity of the A2-B2 Bulk Ordering in Fe-12 At.% Si Alloy *Acta Metall. Mater.* **1991**; 39:3091.
- [180] Straumal BB, Rabkin E, Lojkowski W, Gust W, Shvindlerman LS. Pressure Influence on the Grain Boundary Wetting Phase Transition in Fe-Si Alloys. *Acta Mater.* **1997**; 45:1931.
- [181] Qian H, Luo J. Nanoscale Surficial Films and a Surface Transition in V₂O₅-TiO₂-Based Ternary Oxide Systems. *Acta Mater.* **2008**; 56:4702.

Appendices

The following three appendices are adapted, in part, from the relevant chapters in the doctoral dissertation of Xiaomeng (Jimmy) Shi, entitled “Grain Boundary Premelting and Activated Sintering in Binary Refractory Alloys” (Ph.D., Materials Science and Engineering, May 2010, Clemson University, Clemson, South Carolina, USA).

Appendix A:

Experimental Procedures

(A.1) Raw Materials

High purity molybdenum (99.999%) with an average particle size of 20 μm was purchased from Alfa Aesar. To achieve a homogeneous distribution of nickel in molybdenum, nickel chloride ($\text{NiCl}_2 \cdot 6\text{H}_2\text{O}$, Alfa Aesar) was mixed with molybdenum in a solution/suspension. Then, the slurry was dried in an oven at 90 °C. Afterwards, the powders were annealed in a tube furnace at 600 °C for 1 hour under flowing Ar + 5% H_2 to reduce nickel chloride to nickel.

The physical properties of purchased nickel and molybdenum are listed in Table A.1. The binary phase diagram of Ni-Mo is shown in Fig. A.1. We investigated the GB phenomena and sintering behaviors in three phase regimes: the single-phase regime (BCC), the sub-peritectic two-phase regime (BCC + δ -NiMo), and the solid-liquid two-phase regime (BCC + liquid).

Table A.1 Physical properties of nickel and molybdenum.

Element	Nickel (Ni)	Molybdenum (Mo)
Atomic number	28	42
Atomic weight	58.69	95.94
Density (20 °C g/cm ³)	8.90	10.28
Crystal structure	FCC	BCC
Atomic radius (nm)	0.125	0.139
Ionic radius (nm)	0.069	0.062 (+6e), 0.070 (+4e)
Most common valance	2+	4+, 6+
Melting point (°C)	1455	2623

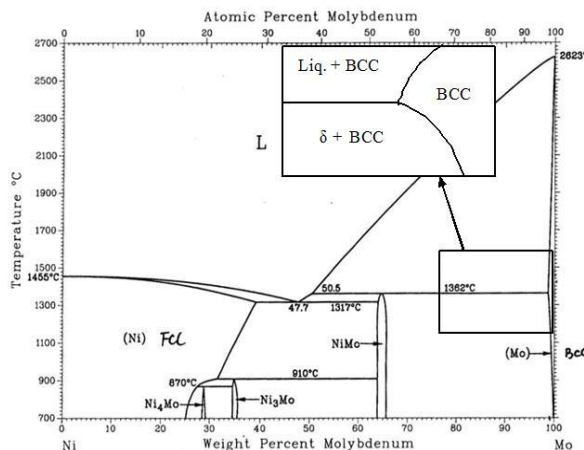


Figure A.1 Phase diagram of the Ni-Mo system. The inset is an enlarged view of the regimes where we conducted experiments.

(A.2) Specimens Preparation

Ni-Mo green specimens were prepared using a standard powder metallurgy method. The calcined Ni-doped Mo powders were grinded gently using a spatula or mortar. Thereafter, cylinder-shape specimens were prepared at 280 MPa using a hand press. The pressed green specimens had a diameter of ~6.36 mm and an average height of 8-9 mm. To prevent the formation of a transient liquid and to ensure the chemical homogeneity, all green specimens were pre-sintered at 1100 °C for 12 hours in flowing Ar + 5% H₂. Then, the specimens were placed in an oil-quench furnace at a desired temperature and isothermally sintered for 3 hours. Afterwards, the specimen was dropped into room-temperature silicone oil in less than 1 second inside the quench chamber under vacuum. The well-quenched specimens were characterized by a scanning electron microscope (SEM, Hitachi 4800) and a HRTEM (Hitachi 9500, 300 kV).

For sintering experiments, the pre-sintering was conducted at 1000 °C for 1 hour and isothermal sintering was carried out in another quench furnace. The lower pre-sintering temperature and shorter pre-sintering time enable us to have a bigger window to extract the GB diffusivity via densification data.

(A.3) Oil-Quench Furnace and Quenching Experiments

A high-temperature quench furnace was built, which is shown in Fig. A.2. Only one specimen may be placed on the sample holder for this furnace for each run. The sample holder is comprised of an alumina tube and a spiral-shape Mo wire container (Fig. A.3). After isothermal sintering was completed, we pulled the quench handle to let the specimen to fall into quench oil (diffusion pump silicone oil), which should happen within approximately 1 second.

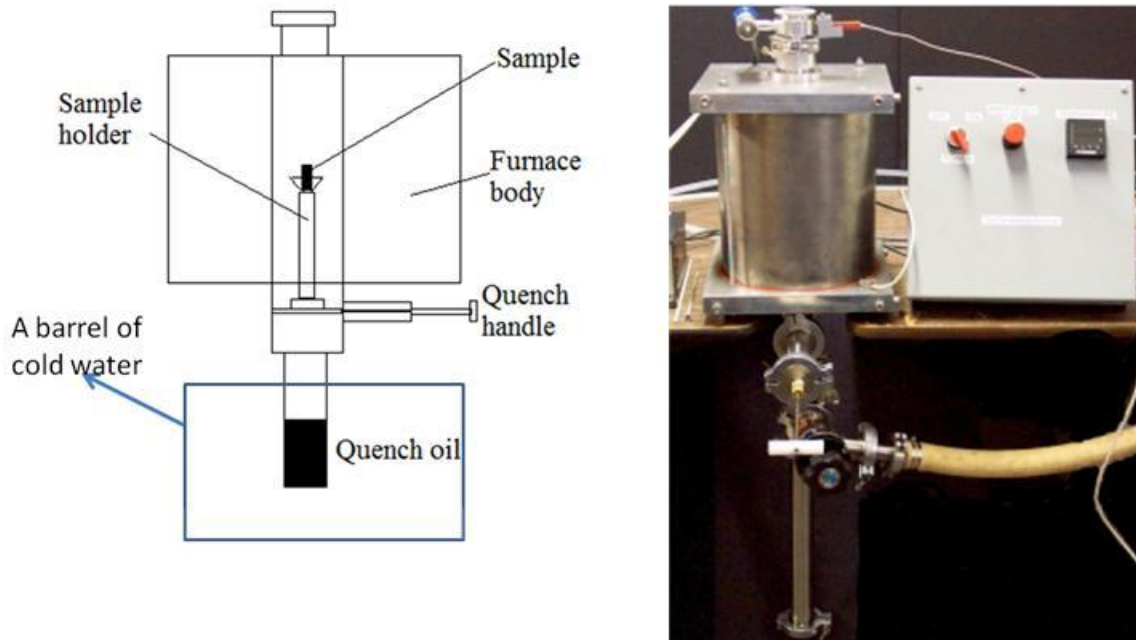


Figure A.2 (a) Schematic illustration and **(b)** picture of the oil-quench furnace.



Figure A.3 The specimen holder for the oil-quench furnace.

(A.4) Gas-Quench Furnace and Sintering Experiments

We assembled a second furnace for specially designed sintering experiments to extract GB diffusivity as a function of temperature and overall composition potential. A schematic of this furnace is shown in Fig. A.4. It is a vertical tube furnace. When the furnace was running, Ar + 5% H₂ gas is flowing through the system to protect specimens from oxidation. This furnace is unique in that a mechanism of loading/unloading samples was built so that the specimens can be inserted into the hot zone of the furnace after the furnace reaches pre-set temperature. The specimens can also be taken out for gas quench after sintering by pulling out the crucible back to the cold zone. Thus, the effects of heating and cooling ramps are minimized. In all experiments, a second thermocouple was placed in the crucible to monitor the actual temperature.

The density of the sample was determined by measuring the dimension and mass. The green specimens were cylindrical, but these specimens deformed to truncated cone shape after sintering. Therefore three measurements were conducted at different heights to calculate the volume.

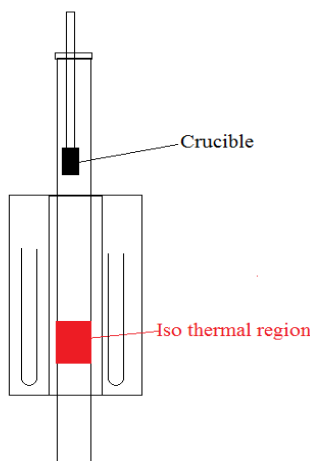


Figure A.4 Schematic illustration of the gas-quench furnace.

(A.5) Extraction of Diffusivity Data

Through measuring the density (and grain size) as a function of time during sintering, we can calculate the densification rates. Then, the bulk or GB diffusivity can then be determined by fitting the well established sintering models. The relevant sintering models are described here. According to Coble, densification is divided into three stages: the initial stage, the intermediate stage, and the final stage (Fig. A.5) [7]. The relevant sintering models are discussed below.

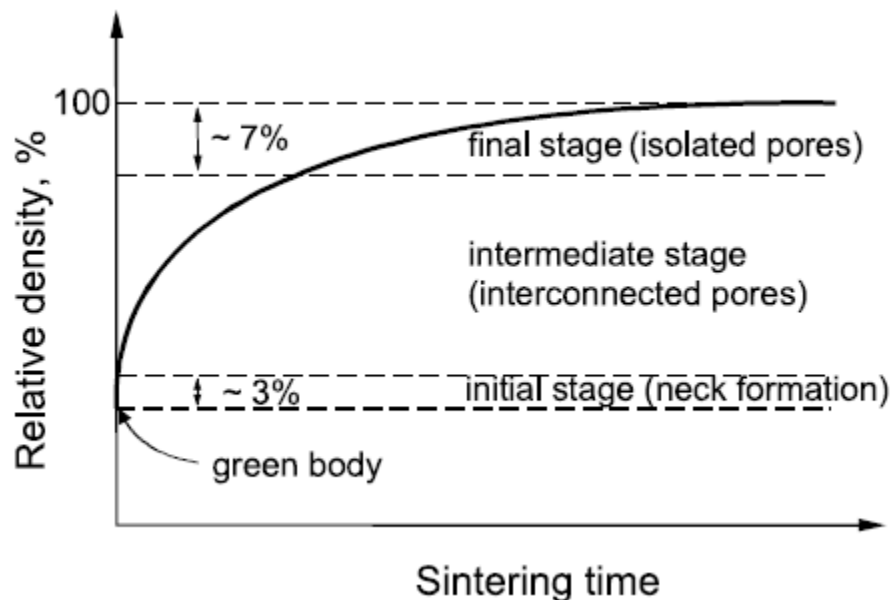


Figure A.5 Typical relative density vs. time during sintering [7].

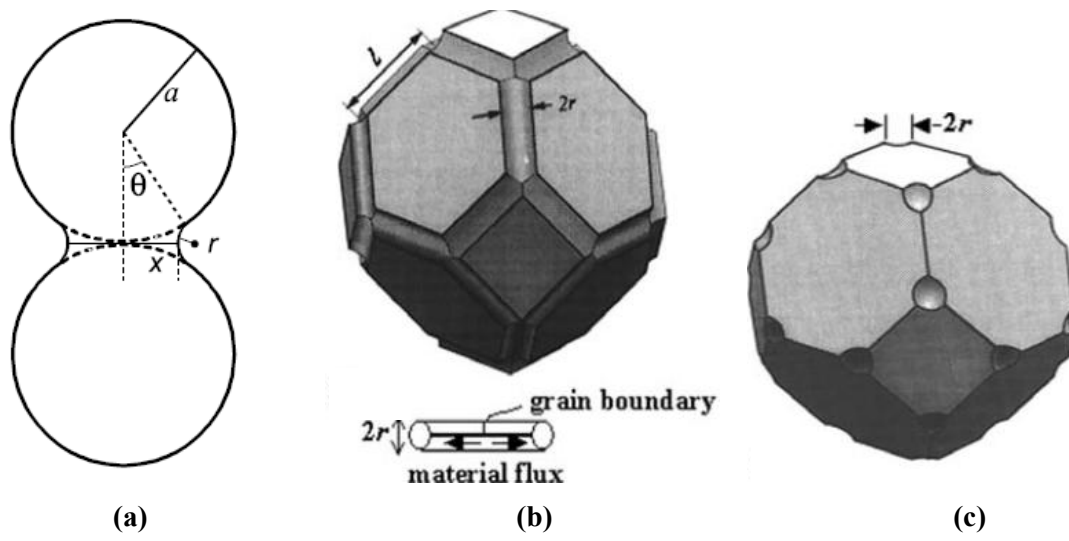


Figure A.6 Models for (a) initial, (b) intermediate, and (c) final stage sintering [7].

Initial-Stage Sintering:

The initial stage sintering is often modeled using a two-sphere model as shown in Fig. A.6(a). The Johnson model [5] is the most widely used for the initial stage of sintering. The key assumptions are:

- Transport due to dislocation or small angle grain boundary is negligible;
- The grain geometry can be represented by two round grains in contact with each other;
- The surface and GB energy are isotropic;
- Vacancy concentration potentials are equal for bulk diffusion and GB diffusion; and
- The densification rate is small ($\Delta L/L_0 < 0.05$).

In the Johnson model, the densification vs. time is represented by:

$$\frac{\Delta L}{L_0} = \left[K \frac{\gamma_s \Omega D}{kTG^p} \right]^m t^m \quad (\text{A.1})$$

where:

$$K = (A.1-6.9)*8; m = \sim 0.4-0.5, p = 3, D = D_{XL}; \text{ for bulk diffusion dominant sintering};$$

and

$$K = (1.6-3)*16; m = \sim 0.3, p = 4, D = \delta D_{GB} \text{ for GB diffusion dominant case.}$$

In the above equations, $\Delta L/L_0$ is the linear shrinkage; γ_s is the surface energy; Ω is the volume of single vacancy; D_{XL} is the bulk diffusivity; D_{GB} is the GB diffusivity; δ is the GB width (which is arbitrarily selected to be 1 nm in most prior studies); k is the Boltzmann constant; T is the sintering temperature; and G is the grain size. German also proposed a similar model [3,6].

Intermediate-Stage Sintering:

In the intermediate stage (Fig. A.6 (b)), a continuous interconnected pore channel forms and shrinkage is large, but grain growth is expected to be mild because GBs are pinned by the pore channels. Coble developed a model for intermediate-stage sintering [1], with the following key assumptions:

- GBs are the sink of vacancies and pores are the source of vacancies;
- The grain geometry is represented by a tetrakaidecahedra (Fig. A.6(b)) with a continuous pore channel at triple-grain junctions; and
- The pore channels have cylindrical.

If the intermediate stage sintering is controlled by **bulk diffusion**, the porosity (P_v) and its derivative with respect to time can be expressed as:

$$P_v - P_v^0 = -336 \frac{D_{XL} \gamma_s \Omega}{kTG^3} t \quad (\text{A.2})$$

$$\frac{dP}{dt} = -336 \frac{D_{XL} \gamma_s \Omega}{kTG^3} \quad (\text{A.3})$$

On the other hand, if the intermediate stage sintering is controlled by **GB diffusion**, the porosity and its derivative with respect to time can be expressed as:

$$P_v^{\frac{3}{2}} - P_v^{0\frac{3}{2}} = -1281 \frac{\delta D_{GB} \gamma_s \Omega}{kTG^4} t \quad (A.4)$$

$$\frac{dP_v^{\frac{3}{2}}}{dt} = -1281 \frac{\delta D_{GB} \gamma_s \Omega}{kTG^4}$$

The above equations assume a constant grain size. Here P_v is porosity and it is defined as:

$$P_v = (1 - \rho_{relative}) \quad (A.5)$$

where $\rho_{relative}$ is the relative density.

Final-Stage Sintering:

After the interconnected pore channels break up and pores become isolated, the sintering enters the final stage (Fig. A.6 (c)). Coble also developed a final-stage sintering model [1]. This model is not discussed here because we did not use final-stage sintering in our experiments to extract GB diffusivities.

(A.6) TEM Specimen Preparation

HRTEM was employed to characterize the structure of GB. To prepare ~3 mm self-supporting TEM specimens, we

- (1) used Buehler low-speed diamond saw to cut a sintered sample into thin pellets which had the same diameter as the sintered sample (~5.8 mm) and was ~ 1 mm in thickness;
- (2) polished the cut pellets on both sides on emery papers of grits 320, 400, 600, 800, and 1000 (in a sequence) to reduce the thickness to about 0.2 mm;
- (3) used a South Bay Technology (SBT) abrasive disc cutter to cut ~3 mm diameter discs;
- (4) further polished the disc (0.2 mm thick and ~3 mm in diameter) on emery paper of grit 1000 and then diamond lapping film/diamond paste with 9 μm , 3 μm and 1 μm particle sizes (in a sequence), to produce a final foil of ~50 μm thick;
- (5) used a Fischione (Model 150D) precision dimple grinder to dimple grind the 50 μm thick foil on both side with a dimple of about 22 μm in depth until the thinnest section in the center was about a few microns;^{*} and
- (6) employed a Fischione Model 1010 low angle argon ion mill to further thin the center of the foil until a perforation appear in the foil and good electron transparency was achieved.

For ion-milling process, key adjustable parameters include accelerating voltage, milling current, milling angle and milling time. Table A.2 listed a few optimized milling recipes that produced good TEM foils for Mo-Ni specimens. We used the Hitachi-9500 300 kV HRTEM to image our specimen. If the electron transparency was not good enough, additional ion-milling can

^{*} For hard metals such as Mo or W, it is recommended to reduce thickness to ~50 μm . For other soft metals or ceramics with high ion-milling etch rates, ~100 μm is generally recommended

[†] Although people generally leave about 20 μm thick foil in the center of the specimen and use a ion-mill to perforate it, in our case of hard metals with low ion-milling etching rates, we must keep the final thickness in the center of the specimens as thin as possible to reduce milling time.

be carried out to further thin the specimen. Usually, good HRTEM images can be obtained if one can find a large field of transparent region from the hole in the center to the peripheral edge.

Table A.2 Representative ion-milling recipes for Ni-Mo specimens.

Recipe #1

Accelerating Voltage	Milling Current	Milling Angle	Stage Temperature	Milling Time
5 kV	5.5 mA	12°	Liquid N ₂	90 mins
5 kV	5.5 mA	9°	Liquid N ₂	30 mins
5 kV	5.5 mA	5°	Liquid N ₂	30 mins

Recipe #2

Accelerating Voltage	Milling Current	Milling Angle	Stage Temperature	Milling Time
5 kV	5.5 mA	12°	Liquid N ₂	120 mins
5 kV	5.5 mA	9°	Liquid N ₂	60 mins
5 kV	5.5 mA	5°	Liquid N ₂	30 mins

(A.7) Auger Electron Spectroscopy and Specimen Preparation

Auger Electron Spectroscopy (AES) was used to identify elemental composition of surfaces by measuring the energies of Auger electrons. Compositional depth profiling was performed by using an independent ion beam to sputter the specimen surface while collecting the Auger electron spectrum. The Auger experiments were conducted at Oak Ridge National Laboratory (ONRL) via the High Temperature Materials Laboratory (HTML) user facility program using a PHI 680 SAM in collaboration with Dr. H. M. Meyer III.

To prevent any contamination, the specimens were fractured *in situ* in an ultra high vacuum (UHV) chamber. Analysis of GBs is possible because the Ni-doped Mo sintered specimens are known to undergo brittle intergranular fracture. A compositional depth profiling was conducted. The sputtering rate was calibrated to be 2 nm per minute for a SiO₂ standard at the same sputtering conditions.

Fig. A.7 shows schematically a specimen fixture for *in situ* fracture in the Auger chamber. The procedure to make AES specimens is described as follows:

- (1) A Buehler low-speed diamond saw was used to cut ~1 mm thick disc from sintered sample.
- (2) The same diamond saw was employed to cut rectangular specimens of ~1 mm × 1 mm × 3.5-5 mm.
- (3) Two notches were made using this diamond saw on midsection of specimen.
- (4) After going through a rigorous clean procedure (described below), the notched specimen was fixed into stainless tube on both ends using SEM-grade conductive epoxy.
- (5) The epoxy-fixed specimen was cured in a 90 °C oven for 6-8 hours. After cool down, the specimen was wrapped with foam carefully and packed in a plastic box.

To minimize the carbon contamination in AES specimen introduced by the cutting fluid, a special clean procedure was implemented to all the notched specimens before making epoxy fixture. The specimens were

- (1) ultrasonically cleaned with acetone for 20 mins to remove all the polar organic contamination and then let dry fully;

- (2) ultrasonically cleaned with toluene for 20 mins to remove all the non-polar organic contamination and then let dry fully;
- (3) ultrasonically cleaned with hexane for 20 mins to remove all the non-polar organic contamination and then let dry fully;
- (4) ultrasonically cleaned with ethanol for 20 mins;
- (5) soaked in ethanol overnight 24 hours to remove all the polar organic and hydrophilic contamination; and
- (6) dried in a 90 °C oven for 3 hours to evaporate all the residue organic contaminant.

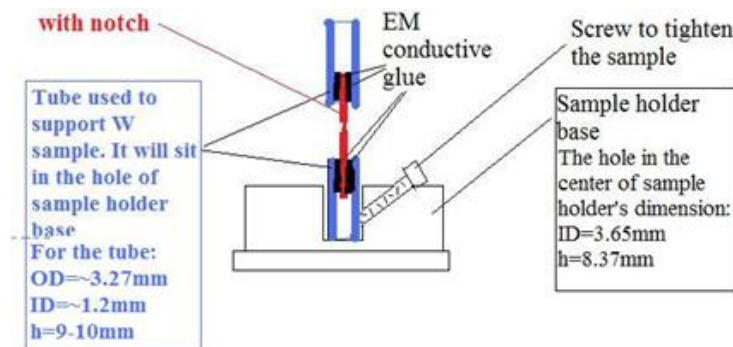


Figure A.7 Schematic illustration of an AES specimen fixture for *in situ* fracture.

(A.8) Grain Boundary Wetting Experiments

A solid-state wetting experiment was performed using a Mo alloy with 12.5 at. % Ni. This Ni content represents ~15 vol. % of δ -NiMo compound phase at the sintering temperature ($T = 1344$ and 1495 °C). Ni (99.999%; Alfa) and Mo (99.999%; Alfa) powders were mixed in distilled de-ionized water and dried. The mixture was compacted in a die at 280 MPa to produce green specimen with ~ 6.35 mm in diameter and 8-9 mm in height. Thereafter, specimen was presintered at 1100 °C for 12 hours and then isothermally sintered at a desired temperature for 2 hours in flowing Ar + 5% H₂. The sintered specimens were polished and characterized with a Hitachi S-4800 SEM equipped with an Oxford EDX detector.

(A.9) Grain Size Measurements

Grain size evolution of specimen was analyzed. A Hitachi S-4800 field emission SEM and Olympus optical microscope were used to measure the grain size. The specimens were polished to mirror finish on emery papers and alumina slurries (or diamond paste). Thereafter, they were etched at room-temperature with 30% volume hydrogen peroxide to make grain boundaries visible. The specific procedure for producing polished and etched samples for grain size analysis is described as follows:

- (1) A Buehler low speed diamond saw was used to cut discs from sintered pellets.
- (2) The specimens were then roughly polished with emery papers of grit sizes of 240, 400, 600, 800, 1000 in a sequence (while always orienting the scratches normal to the direction of prior polishing).

- (3) Then, specimens were finely polished with alumina suspensions in water (or diamond pastes) to get a mirror finish.
- (4) The polished Ni-Mo specimens were etched at room-temperature using hydrogen peroxide for 45 second to 1 min.

(A.10) References for Appendix A

- [1] RL Coble. *J. App. Phys.* 32 (1961) 787.
- [2] RM German. *Liquid Phase Sintering*, Plenum Press, New York, 1985.
- [3] RM German, ZA Munir. *J. Less-Common Met*, 58 (1978) 61.
- [4] RM German, P Suri, SJ Park. *J. Mater. Sci.* 44 (2009) 1.
- [5] DL Johnson. *J. Appl. Phys.* 40 (1969) 192.
- [6] JL Johnson, RM German. *Metall. Mater. Trans.* 27A (1996) 441.
- [7] SL Kang. *Sintering*, Butterworth-Heinemann, 2004.
- [8] WD Kingery. *J. Appl. Phys.* 30 (1959) 301.

Appendix B: Thermodynamic Models

(B.1) Phenomenological Thermodynamic Model

A phenomenological thermodynamic model can be proposed as an extension to a premelting model for unary systems [1,2,3]. In this model for binary alloys, the excess GB energy (referred to a mixture of equilibrium bulk phases) of a subsolidus liquid-like IGF in a binary A-B alloy is expressed as:

$$\sigma^x(h) \equiv G^S - (\mu_A \Gamma_A + \mu_B \Gamma_B) = 2\gamma_{cl} + \Delta G_{amorph} h + \sigma_{interfacial}(h), \quad (B.1)$$

where G^S is excess free energy according to the Gibbs definition, μ is the bulk potential, Γ is the adsorption (GB excess), h is the film thickness, γ_{cl} is the interfacial energy of the crystal-liquid interface (which is well defined when the two interfaces are well separated or $h \rightarrow +\infty$), $\Delta G_{amorph} \equiv G_{liquid} - G_{crystal}$ is the volumetric free energy for forming an undercooled liquid (assuming a uniform film), and $\sigma_{interfacial}$ is the *interfacial potential* (where $d\sigma_{interfacial}/dh$ is the well-known Derjaguin disjoining pressure). The interfacial potential ($\sigma_{interfacial}(h)$) represents the interactions of two interfaces when the film is thin, and it is the sum of all short- and long-range interfacial interactions using $h = +\infty$ as the reference point. By definition,

$$\begin{cases} \sigma_{interfacial}(0) = (\gamma_{gb}^{(0)} - 2\gamma_{cl}) \equiv -\Delta\gamma \\ \sigma_{interfacial}(+\infty) = 0 \end{cases}, \quad (B.2)$$

where we define $\gamma_{gb}^{(0)} \equiv \sigma^x(0)$ as the excess free energy of a “dry” GB, which is in general different from the equilibrium γ_{gb} . The equilibrium GB energy (γ_{gb}) corresponds to the global minimum in $\sigma^x(h)$, which specifies an “equilibrium” thickness:

$$\begin{cases} \frac{d\sigma^x(h)}{dh} \Big|_{h=h_{eq.}} = 0 \\ \gamma_{gb} \equiv \sigma^x(h_{eq.}) \end{cases}. \quad (B.3)$$

One may further define a dimensionless *interfacial coefficient* as

$$f(h) \equiv 1 + \frac{\sigma_{interfacial}(h)}{\Delta\gamma}, \quad (B.4)$$

which satisfies

$$\begin{cases} f(0) = 0 \\ f(+\infty) = 1 \end{cases}. \quad (B.5)$$

Then, Eq. (B.1) can be rewritten as:

$$\Delta\sigma(h) \equiv \sigma^x(h) - \gamma_{gb}^{(0)} = \Delta\gamma \cdot f(h) + \Delta G_{amorph}h. \quad (\text{B.6})$$

A liquid-like IGF of thickness h can be thermodynamically more stable than a dry GB if $\Delta\sigma(h) < 0$. As such, an estimation of the IGF thickness can be given as:

$$h_{eq} = \frac{\Delta\gamma}{\Delta G_{amorph}} \cdot f(h_{eq}) < \frac{\Delta\gamma}{\Delta G_{amorph}^*} \equiv \lambda_L^* \quad (\text{B.7})$$

Here the subscript “L” is used to denote that ΔG_{amorph} is calculated using a reference composition on the stable or metastable liquidus line. (Possible strategies of selecting this hypothetic reference film composition are discussed in §B.2, among which this assumption leads a theoretically elegant treatment of the phenomenological model.) If the interfacial coefficient takes a simple exponentially decaying form with a characteristic coherent length of ξ (as what is commonly assumed for the premelting theories for one-component metals):

$$f(h) \approx 1 - e^{-h/\xi}, \quad (\text{B.8})$$

minimizing $\Delta\sigma(h)$ leads to:

$$h_{EQ} \approx \xi \cdot \ln(\lambda_L^* / \xi), \quad (\text{B.9})$$

(B.2) Through-Thickness Gradients, Film Composition and Simplifications

Through-thickness compositional and structural gradients generally exist in an IGF. Correspondingly, ΔG_{amorph} is calculated after a (somewhat subjective) selection of a reference film composition (for a hypothesized uniform film of undercooled liquid as a reference state); the remaining volumetric free energies, along with the excess free energies associated with the compositional and structural gradients, is then be considered in the interfacial potential so that the thermodynamic treatment remains rigorous. Prior studies have assumed this reference composition to be the average film composition [4,5] or the composition that maximizes a particular figure of merit (such as the λ discussed below). In either of the above conventions, this reference composition becomes a function of film thickness, approaching the (stable or metastable) liquidus composition (X_L) as $h \rightarrow +\infty$. An alternative, and perhaps theoretically more elegant, strategy is to select a constant reference film composition (independent of h). In this case, this reference composition must be X_L to ensure that $\sigma_{\text{interfacial}}(+\infty) = 0$, even if the average film composition can be significantly different from X_L when the film is thin.

Furthermore, the equilibrium γ_{cl} should consider the effects of the near-interface gradients in composition (adsorption) and structure (partial ordering), which are generally difficult to quantify. An useful strategy is to define a new “un-relaxed” $\gamma_{cl}^{(0)} (> \gamma_{cl})$ for a hypothesized “step” interface between a crystal and a perfect liquid (without any adsorption and near-interface ordering), which can be easier to quantify (as discussed in the following section). Then, we can define a new thermodynamic variable with respect to a hypothesized uniform film of a perfect liquid, as:

$$\lambda_X(X_{film}) \equiv \frac{\gamma_{gb}^{(0)} - 2\gamma_{cl}^{(0)}(X_{film})}{\Delta G_{amorph}(X_{film})}. \quad (B.10)$$

Two particular λ 's that can be quantified are:

$$\begin{cases} \lambda \equiv \underset{(0 < X_{film} < 1)}{\text{Max}} \{ \lambda_X(X_{film}) \} \\ \lambda_L \equiv \lambda_X(X_L) \end{cases} \quad (B.11)$$

It is easy to demonstrate that:

$$\lambda_L < \lambda; \quad \lambda_L < \lambda_L^*, \quad (B.12)$$

and

$$\begin{cases} \lim_{\lambda \rightarrow +\infty} \frac{\lambda_L}{\lambda} \rightarrow 1 \\ \frac{\lambda_L^*}{\lambda_L} = \frac{\gamma_{gb}^{(0)} - 2\gamma_{cl}^{(0)}}{\gamma_{gb}^{(0)} - 2\gamma_{cl}^{(0)}}. \end{cases} \quad (B.13)$$

All three λ 's represent the thermodynamic tendency for stabilizing subsolidus liquid-like IGFs, and they scale the actual film thickness. Since the exact form of the interfacial potential is generally unknown, none of them can guarantee more prediction power than others. While λ_L^* appears to be conceptually more rigorous, λ and λ_L are generally easier to quantify. In an earlier publication [6], we quantified λ via a numerical method. More recently, we derived an analytical solution for λ_L for regular solutions [7] (and in this appendix we further generalize it to subregular solutions), which is practically useful.

In summary, λ_L , which is the maximum thickness of a stable IGF assuming an uniform film composition of X_L and no interfacial interactions, appears to be the most convenient thermodynamic variable to be used practically. Thus, it will be used here. To compute λ_L as a function of temperature and bulk composition, interfacial energies (γ 's) and bulk free energies (to compute ΔG_{amorph}) need to be quantified via statistical models or computational thermodynamic methods, which are discussed in following sections.

(B.3) Estimation of Interfacial Energies via Statistical Models

The interfacial energies (γ 's) can be estimated by either lattice-gas models or Miedema type “macroscopic atom” models.

Lattice-Gas Models:

In the lattice gas-model, the crystal-liquid interfacial energy can be expressed as [8]:

$$\gamma_{cl}^{(0)} = \gamma_{\langle A \rangle - \{A\}} X_A^S + \gamma_{\langle B \rangle - \{B\}} X_B^S + \frac{m_1 \omega_L (X_A^L X_B^S + X_A^S X_B^L)}{V^{2/3}} - \frac{m_1 \omega_L X_A^L X_B^L}{V^{2/3}} - \frac{m_1 \omega_S X_A^S X_B^S}{V^{2/3}} \quad (B.14)$$

where $\gamma_{<A>-\{A\}}$ and $\gamma_{-\{B\}}$ represent the solid-liquid interfacial energies of pure A or B respectively; X_A^S and X_A^L are atomic fractions of A in solid and liquid, respectively; similarly, X_B^S and X_B^L are atomic fractions of B in solid and liquid, respectively ($X_A^S + X_B^S = 1$; $X_A^L + X_B^L = 1$); ω_L and ω_S are the regular solution parameters for solid and liquid, respectively; m_1 is the fraction of the (liquid type) bonds that are “cross” the interface; V is molar volume; $V^{2/3}$ is molar area; R is gas constant; and T is temperature. Essentially, the estimation of solid-liquid interfacial energy by Eq. (B.14) is through calculating the bond energies. Here the key assumptions (simplifications) are:

- The solid-liquid interface can be represented by a step function (i.e., adsorption at the interface and near-interface ordering are not considered); thus only the bonds between the first layer of the liquid and first layer of the solid contribute to the interfacial energy;
- These bonds at the interface is liquid type; and
- The reference state is bulk binary solutions (assuming that the bulk solid is in a thermodynamic equilibrium with the bulk liquid phase).

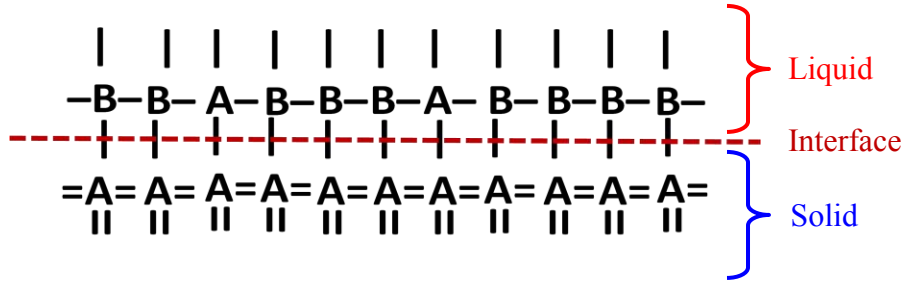


Figure B.1 Schematic illustration of the lattice-gas model for a liquid-solid interface of an A-B binary system. Assuming that the solubility of B in solid is negligible ($X_B^S = 0$).

If the solubility of B in A crystal is negligible ($X_B^S = 0$; $X_A^S = 1$), Eq. (B.14) can be simplified to:

$$\gamma_{cl}^{(0)} = \gamma_{<A>-\{A\}} + \frac{m_1 \omega_L}{V^{2/3}} (1 - X_A^L)^2 \quad (B.15)$$

where the first term is due to the enthalpic contribution; the second term is the interaction contribution (a “chemistry” term resulted from the formation of a different number of A-B bonds at the interfaces as compared that in the bulk liquid). The above lattice-gas model is schematically illustrated in Fig. B.1.

The above model can be further modified by considering the adsorption and compositional gradients at the solid-liquid interfaces, which are discussed by Shimizu and Takei [9,10]. An entropic term associated with ordering at the interfaces (discussed below in the Benedictus model) can also be added.

“Macroscopic Atom” Models:

Instead of using the lattice-gas type models described above, we adopt and modify a Miedema type “macroscopic atom” model to estimate interfacial energies. The “macroscopic atom” model is developed on a similar base as lattice-gas models, and it is more realistic to represent actual transition metal alloys. This “macroscopic atom” model has the following features (that are useful for achieving our objectives):

- It considers the different molar volumes for A and B;
- It represents average interfaces without anisotropic effects (while the lattice-gas models considers the anisotropic effects via the coordination numbers); and
- It provides a systematical method to evaluate all required thermodynamic parameters (for all binary transition metal alloys as well as some other alloys).

Benedictus *et al.* reported a systematical approach to evaluate interfacial energies based on the Miedema type “macroscopic atom” model, and the entropic contribution is added into the model [11]. In this model, the interfacial energy for an A crystal (assuming that the solubility of B in A crystal is negligible) and a binary A-B liquid is expressed as:

$$\gamma_{cl}^{(0)} = \underbrace{\frac{H_A^{\text{fuse}}}{C_0 V_A^{2/3}}}_{\text{Enthalpic}} + \underbrace{\frac{\Delta H_{A \text{ in } B}^{\text{interface}} F_B^A}{C_0 V_A^{2/3}}}_{\text{Interaction}} + \underbrace{\frac{1.9RT}{C_0 V_{A/B}^{2/3}}}_{\text{Entropic}} \quad (\text{B.16a})$$

where H_A^{fuse} is the fusion enthalpy of A; $\Delta H_{A \text{ in } B}^{\text{interface}}$ is the enthalpy of solution (similar as shown in the Miedema model); $C_0 \approx 4.5 \times 10^8$; V is the molar volume (neglecting thermal expansion); R is the gas constant; and F_B^A represents the “area” fraction A-B bonds at the interface, which is expressed as:

$$F_B^A = \frac{X_B V_B^{2/3}}{(1-X_B)V_A^{2/3} + X_B V_B^{2/3}}, \quad (\text{B.17})$$

where X_B is the atomic fraction of B in the liquid phase.

In Eq. (B.16a), liquid-crystal interfacial energy is comprised of enthalpic, interaction, and entropic contributions, which are articulated in Ref. [11].

It is important to note that the interaction term in Eq. (B.16a) is derived assuming that the reference states are solid pure A and pure B (which is valid for the discussion of solid-state amorphization -- the initial objective for Benedictus *et al.*’s work). In our case, however, we wish to use the thermodynamic equilibrium state as the reference state. To achieve this, we may assume that the reference state is set by the bulk liquid (by assuming the bulk solid A, with negligible solutes of B, is in a thermodynamic equilibrium with the bulk liquid). In other words, the reference state for the interaction term is set by a hypothetical liquid-liquid interface, which should have zero excess interfacial energy but the “macroscopic atom” model would produce the following interfacial energy:

$$\gamma_{\text{liq-liq.}}^{(\text{Inter. Ref.})} = \frac{\Delta H_{A \text{ in } B}^{\text{interface}}}{C_0 V_A^{2/3}} [2F_B^A \cdot (1-F_B^A)], \quad (\text{B.16b})$$

where $[2F_B^A \cdot (1 - F_B^A)]$ represents the “area” fraction of A-B bonds for this hypothetical liquid-liquid interface (which should produce zero excess interaction energy by definition). Thus, Eq. (B.16a) should be revised to

$$\gamma_{cl}^{(0)} = \underbrace{\frac{H_A^{\text{fuse}}}{C_0 V_A^{2/3}}}_{\text{Enthalpic}} + \underbrace{\left[\frac{\Delta H_{A \text{in } B}^{\text{interface}} F_B^A}{C_0 V_A^{2/3}} - \frac{1}{2} \gamma_{\text{liq-liq.}}^{\text{(Inter. Ref.)}} \right]}_{\text{Interaction}} + \underbrace{\frac{1.9RT}{C_0 V_{A/B}^{2/3}}}_{\text{Entropic}} \quad (\text{B.16c})$$

Or:

$$\gamma_{cl}^{(0)} = \underbrace{\frac{H_A^{\text{fuse}}}{C_0 V_A^{2/3}}}_{\text{Enthalpic}} + \underbrace{\frac{\Delta H_{A \text{in } B}^{\text{interface}} (F_B^A)^2}{C_0 V_A^{2/3}}}_{\text{Interaction}} + \underbrace{\frac{1.9RT}{C_0 V_{A/B}^{2/3}}}_{\text{Entropic}} \quad (\text{B.16d})$$

Here, we use Mo-Ni as an example. Specific to this system of our interest, the liquid-crystal interfacial energy was derived from Eq. (B.16d) and determined as

$$\gamma_{cl}^{Ni-Mo} = [0.138 - 0.160(F_{Ni}^{Mo})^2 + 8.92 \times 10^{-5}T] \text{ J/m}^2 \quad (\text{B.18})$$

where

$$F_{Ni}^{Mo} = \frac{X_{Ni} V_{Ni}}{X_{Ni} V_{Ni} + X_{Mo} V_{Mo}} = \frac{X_{Ni}}{1.253 - 0.253 X_{Ni}} \quad (\text{B.19})$$

The average GB energy of Mo, $\gamma_{gb}^{(0)}$, in polycrystalline materials was determined by using the Turnbull’s estimation [12,13,14,15]:

$$\gamma_{gb}^{(0)} \approx 1/3 \cdot \gamma_{Mo}^s \quad (\text{B.20})$$

The surface energy of Mo at $T = 0\text{K}$ was estimated by enthalpy of evaporation:

$$\gamma_{Mo}^s = \frac{H_{Mo}^{\text{vap}}}{C_0 V_{Mo}^{2/3}} \quad (\text{B.21})$$

In reality, surface energy is temperature-dependent, where both the thermal expansion effect and entropy effect need to be considered.

$$\gamma_{Mo}^s(T_1) = \frac{(\gamma_{Mo}^s V_{Mo}^{2/3})^{T=0K} + b_{Mo} T_1}{(V_{Mo}^{2/3})^{T=T_1}} \quad (\text{B.22})$$

b_{Mo} is a materials-dependent constant. Furthermore, structure relaxation at free surface will also reduce its excess energy. Nevertheless, these effects are relatively small (as compared with the approximations associated with Eq. (B.20)), and they are generally more difficult to quantify. Thus they were neglected in our calculation for simplicity. Combining Eq. (B.20) and (B.21) gives an estimation of $\gamma_{gb}^{(0)} \approx 1.0 \text{ J/m}^2$.

The limitations of this model include:

- Adsorption at liquid-crystal interfaces is not considered. This is addressed, in part, in lattice-gas model by Shimizu & Takei.[9,10]

- Anisotropic effects are not considered. This is considered in a sophisticated lattice-gas model by Wynblatt *et al.* [16].
- Segregation within the lattice at GBs is not considered. This can be considered by Wynblatt *et al.*'s model [16].
- The “asymmetric effects,” which are not addressed here in regular solution type models, is discussed by in subregular solution model by Antion and Chatain [17].

(B.4) Estimation of the Free Energy Penalty for Forming An Undercooled Liquid

CalPhiD Methods:

The Calculation of Phase Diagram (CalPhiD) methods were adopted to determine the free energy penalty to form an undercooled liquid (ΔG_{amorph}). CalPhiD is a well established method to compute bulk phase diagrams from (usually empirically-fitted) thermodynamic functions of free energies. The Gibbs free energy of a phase Φ in a binary A-B system can be expressed as:

$$G^\Phi = \sum_{i=A,B} X_i {}^0 G_i^\Phi + RT \sum_{i=A,B} X_i \ln X_i + {}^{xs} G^\Phi \quad (\text{B.23})$$

where ${}^0 G_i^\Phi$ is the Gibbs free energy of the pure element i ($= A$ or B) that is present in Φ phase; X_i is the atomic fraction of element i ; ${}^{xs} G^\Phi$ is the excess Gibbs free energy, which can be empirically expressed in a Redlich-Kister polynomial:

$${}^{xs} G^\Phi = X_A X_B \sum_{j=0}^n L_j^\Phi (X_A - X_B)^j. \quad (\text{B.24})$$

Here, L_j^Φ 's are empirically-fitted parameters for the phase Φ . If $n = 0$, the phase Φ is a regular solution, and Eq. (B.24) is reduced to

$${}^{xs} G^\Phi = L_0^\Phi X_A X_B \equiv \omega X_A X_B. \quad (\text{B.25})$$

where ω ($= L_0^\Phi$) is the regular solution parameter. If $\omega = 0$, the phase Φ is an ideal solution (${}^{xs} G^\Phi = 0$).

If $n = 1$, the phase Φ is a sub-regular solution. Eq. (B.24) can be rewritten as

$${}^{xs} G^\Phi = L_0^\Phi X_A X_B + L_1^\Phi X_A X_B (X_A - X_B). \quad (\text{B.26})$$

Gibbs free energy functions for compounds and ordered solutions can be constructed using different models, which are discussed in Ref. [18]. For a given binary A-B system, the Gibbs free energy functions can be developed for all possible phases. Then a bulk phase diagram can be constructed by minimizing the total free energy of the system. In two-phase regions, the equilibrium states can be found graphically via a well-established “common tangent construction” method.

For the Ni-Mo binary system (as the first computation example), four phases (BCC, FCC, δ -NiMo, and liquid phases) are considered. The excess Gibbs energies of them were determined

and the Gibbs free energies of different phases are listed in Table B.1(a) [19] and Table B.1(b) [20].

Table B.1(a) Gibbs free energies of the different phases in the Ni-Mo system [19].

Phase	Gibbs free energy, J/mol
Liquid phase	$X_{Ni}^o G_{Ni}^{liq} + X_{Mo}^o G_{Mo}^{liq} - T\Delta S_{conf.} + X_{Ni}X_{Mo}[-46540 - 19.53T - 2915(X_{Mo} - X_{Ni})]$
Mo-rich BCC	$X_{Ni}^o G_{Ni}^{BCC} + X_{Mo}^o G_{Mo}^{BCC} - T\Delta S_{conf.} + 46422X_{Ni}X_{Mo}$
Ni-rich FCC	$X_{Ni}^o G_{Ni}^{FCC} + X_{Mo}^o G_{Mo}^{FCC} - T\Delta S_{conf.} + X_{Ni}X_{Mo}[-4803.7 - 5.96T - 10880(X_{Mo} - X_{Ni})]$
δ -NiMo	$24^o G_{Ni}^{FCC} + 32^o G_{Mo}^{BCC} - 212100 + 1089T - 142T \ln(T)$

Note: $\Delta S_{conf} = X_{Ni} \ln X_{Ni} + X_{Mo} \ln X_{Mo}$.

Table B.1(b) Gibbs free energies of the different phases in the Ni-Mo system [20].

Phase	Gibbs free energy, J/mol
Liquid phase	$X_{Ni}^o G_{Ni}^{liq} + X_{Mo}^o G_{Mo}^{liq} - T\Delta S_{conf.} + X_{Ni}X_{Mo}[-39597 + 15.935T - 7373(X_{Mo} - X_{Ni}) + (-12123 + 5.551T)(X_{Mo} - X_{Ni})^2]$
Mo-rich BCC	$X_{Ni}^o G_{Ni}^{BCC} + X_{Mo}^o G_{Mo}^{BCC} - T\Delta S_{conf.} + X_{Ni}X_{Mo}[27691 + 18792(X_{Mo} - X_{Ni})]$
Ni-rich FCC	$X_{Ni}^o G_{Ni}^{FCC} + X_{Mo}^o G_{Mo}^{FCC} - T\Delta S_{conf.} + X_{Ni}X_{Mo}[-8916 + 3.591T + (5469 - 0.249T)(X_{Mo} - X_{Ni}) + (-1549 - 2.741T)(X_{Mo} - X_{Ni})^2]$
δ -NiMo	$24^o G_{Ni}^{FCC} + 20^o G_{Mo}^{BCC} + 12^o G_{Mo}^{BCC} - 169981 + 1154.981T - 155.484T \ln(T) + 24^o G_{Ni}^{FCC} + 20^o G_{Ni}^{FCC} + 12^o G_{Mo}^{BCC} - 154106 + 2855.001T - 394.923T \ln(T) - 199.856T + 0.3367 \cdot [(-829211 + 825.923T) + 0.3571 \cdot (-417368 + 326.504T)]$

Note: $\Delta S_{conf} = X_{Ni} \ln X_{Ni} + X_{Mo} \ln X_{Mo}$.

Table B.1(c) Comparison of phase diagram data comparison by the two groups of thermodynamic functions listed in Table B.1(a) and Table B.1(b), respectively.

Key markers	Experimental value	Krisk's [19]	Zhou <i>et al.</i> 's [20]
$T_{peritectic}$, °C	1362 [21,22]	1364	1345
Solidus line and solvus line of BCC	From ref. [23,24]	Good fit	No validation

The thermodynamic functions in Table B.1(b) is more sophisticated than those in Table B.1(a) by considering entropic contribution to the Gibbs free energy of δ -NiMo compound. Consequently, the thermodynamic functions listed Table B.1(b) achieved better accuracy for predicting FCC phase and intermetallic compounds. However, the thermodynamic functions in Table B.1(a) lead to better predictions for the solidus and solvus lines of the Mo-rich BCC and the peritectic temperature, which are our primary concerns. Therefore, we used Table B.1 for our calculations.

When the thermodynamic functions of all phases are known, we can construct binary phase diagram by drawing common tangent line and finding equilibrium phases. Constructions for two representative temperatures of the Mo-Ni binary system are shown in Fig. B.2.

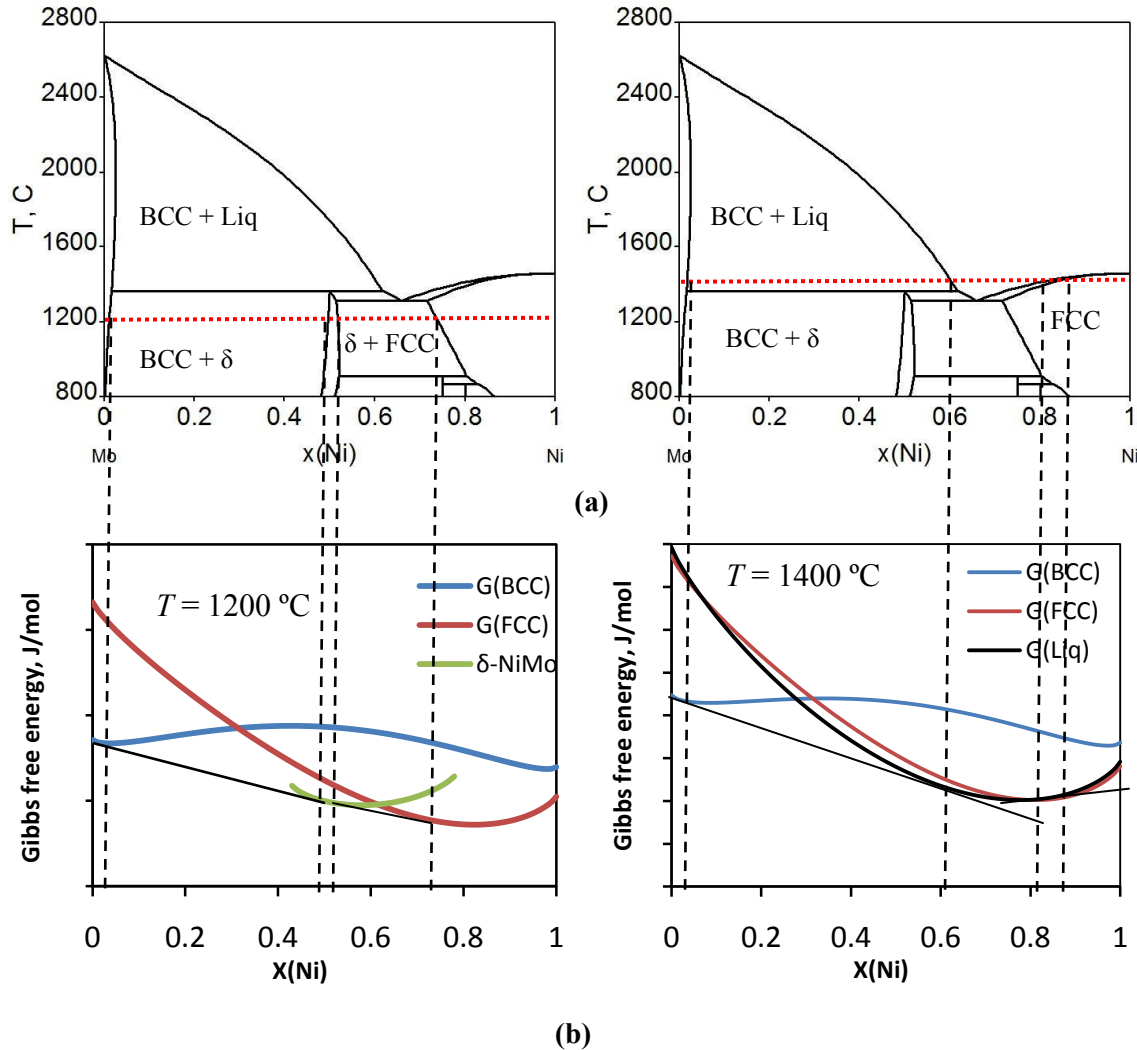


Figure B.2 Schematic illustration of phase diagram constructions: **(a)** The Mo-Ni binary phase diagram. **(b)** Plots of Gibbs free energies of different phases vs. Ni atomic fraction for $1200 \text{ °C} (< T_{\text{peritectic}})$ and $1400 \text{ °C} (> T_{\text{peritectic}})$, in which common tangent lines were drawn to find the phase boundaries.

Determination of ΔG_{amorph} and λ_L :

The CalPhaD method was used to compute ΔG_{amorph} and then λ . Again, we used Mo-Ni as the first computation example. *From now on, the subscript “Ni” is dropped for brevity, all the X’s (X , X_{film} , X_S , X_L) in equations are referred to as atomic fraction of Ni in Ni-Mo binary system with the following definitions.*

- X : the Ni fraction (general)
- X_{film} : the Ni fraction of IGF
- X_0 : the Ni fraction of the bulk (BCC) phase (which sets the bulk chemical potentials)
- X_S : the Ni fraction on the solidus line or (if $T < T_{\text{preitecic}}$) its metastable extension
- X_L : the Ni fraction on the liquidus line or (if $T < T_{\text{preitecic}}$) its metastable extension
- X_{solvus} : the Ni fraction on the solvus line (for $T < T_{\text{preitecic}}$)

In particular, analytical expressions for λ_L can be obtained for Ni-doped Mo with two assumptions. First, the IGF has a uniform composition that is equal to the composition on the liquidus line or its metastable extension. Second, the solid (BCC) phase is a regular or sub-regular solution so its mixing Gibbs energy is given by

$$\Delta G_{\text{Solid}}^{\text{MIX}} = RT[X_0 \ln X_0 + (1 - X_0) \ln(1 - X_0)] + L_0^S X_0 (1 - X_0) + L_1^S X_0 (1 - X_0)(1 - 2X_0), \quad (\text{B.27})$$

where X_0 is the Ni atomic fraction in the solid phase; L_0^S ($=\omega$) and L_1^S are sub-regular (or regular) solution parameters. In our calculations, the solid phase is the BCC phase because the FCC phase is unstable in this composition region of interest.

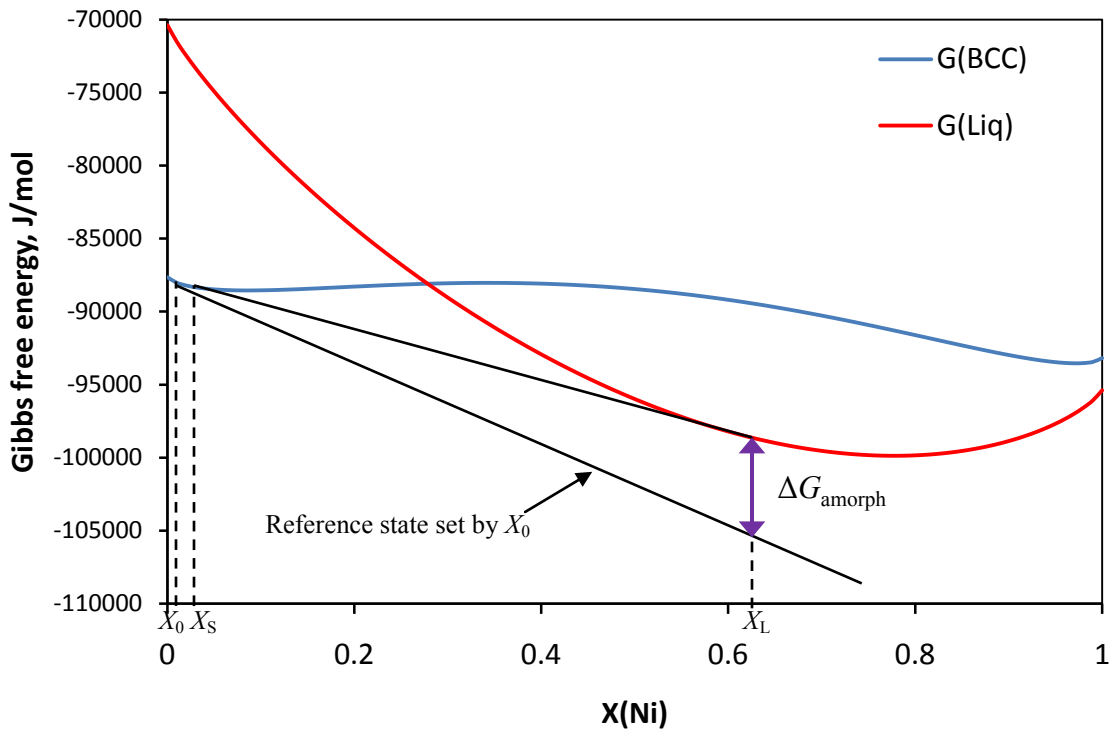
First, we will determine the ΔG_{amorph} in the single-phase (BCC) regime. Fig. B.3 shows an example at $T = 1400$ °C ($T > T_{\text{peritecic}}$), in which we assume that the composition of the bulk BCC phase (X_0) is lower than the bulk solidus composition (X_S). The ΔG_{amorph} is defined as the difference between formation energy of the liquid phase (the red line in Fig. B.3(a)) and the reference state set by the chemical potential of the bulk phase of a composition X_0 (the black straight line labeled in Fig. B.3(a)). This reference state is given by:

$$G^{\text{Ref}}(X) = X_{\text{film}} \cdot \mu_{\text{Ni}} + (1 - X_{\text{film}}) \cdot \mu_{\text{Mo}} = G_{\text{bcc}}^f(X_0) + (X_{\text{film}} - X_0) \frac{dG_{\text{bcc}}^f}{dX} \bigg|_{X=X_0}, \quad (\text{B.28})$$

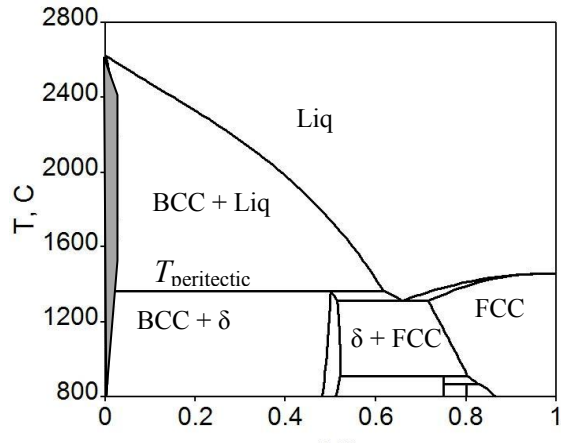
which corresponds to the tangent line extended from X_0 in Fig. B.3 (a). Thus, the free energy penalty to form a metastable liquid of composition X_L (being labeled by a purple double arrow in Fig. B.3(a)) is given by:

$$\Delta G_{\text{amorph}} \approx G_{\text{liq}}^f(X_L) - \left[G_{\text{bcc}}^f(X_0) + (X_L - X_0) \frac{dG_{\text{bcc}}^f}{dX} \bigg|_{X=X_0} \right], \quad (\text{B.29})$$

where G_{liq}^f and G_{bcc}^f are the formation free energies of liquid and solid BCC phases, respectively.



(a)



(b)

Figure B.3 (a) The representation of $\Delta G_{\text{amorph}}(X_L)$ in the plots of Gibbs free energies vs. Ni fraction for a case of $X_0 < X_S$ and $T = 1400$ °C ($> T_{\text{peritectic}}$), where X_0 is the bulk composition. X_S and X_L are equilibrium solidus and liquidus compositions, respectively. **(b)** The corresponding bulk phase diagram, where the single-phase regime of interest is shaded.

By definition, ΔG_{amorph} vanishes if the composition of solid BCC phase is on the bulk

solidus line ($X_0 = X_S$), which is the case represented the common tangent line between X_S and X_L in Fig. B.3 (a); thus

$$G_{liq}^f(X_L) = G_{bcc}^f(X_S) + (X_L - X_S) \frac{dG_{bcc}^f}{dX} \bigg|_{X_S} . \quad (\text{B.30})$$

Combining Eqs. (B.27-B.30) while assuming $X_{\text{film}} = X_L$ gives:

$$\begin{aligned} \Delta G_{\text{amorph}} = RT & \left[X_L \ln \frac{X_s}{X_0} + (1 - X_L) \ln \frac{1 - X_s}{1 - X_0} \right] - \\ & (X_S - X_0) \left[2X_L (L_0^{BCC} + 3L_1^{BCC}) - (L_0^{BCC} + 3L_1^{BCC} + 6L_1^{BCC}) (X_S + X_0) + 4L_1^{BCC} (X_S^2 + X_S X_0 + X_0^2) \right] \end{aligned} \quad (\text{B.31})$$

If the solid BCC phase is a regular solution ($L_1^{BCC} = 0$; $L_0^{BCC} = \omega$), it can be reduced to

$$\Delta G_{\text{amorph}} = RT \left[X_L \ln \frac{X_s}{X_0} + (1 - X_L) \ln \frac{1 - X_s}{1 - X_0} \right] - \omega (X_S - X_0) (2X_L - X_S - X_0) . \quad (\text{B.32})$$

Second, in the single BCC phase regime below $T_{\text{peritectic}}$, the calculation is almost the same as that described above for $T > T_{\text{peritectic}}$. The same equations are used, and the only difference is that X_S and X_L are now the Ni fractions on the metasatble extensions of the solidus and liquidus lines, as illustrated in Fig. B.4 (for an example for $T = 1200$ °C). Note that now the solid solubility corresponds to the solvus line X_{solvus} (instead of X_S , which is on the metastable extension of solidus line) for $T > T_{\text{peritectic}}$.

Finally, in the sub-peritectic two-phase regime, $\Delta G_{\text{amorph}}(X_L)$ is a constant at a specific temperature and it does not depend on the overall bulk composition (because the bulk chemical potential is a constant). Therefore, $\Delta G_{\text{amorph}}(X_L)$ can be determined by using Eq. (B.32) or (B.31) and assuming $X_0 = X_{\text{solvus}}$:

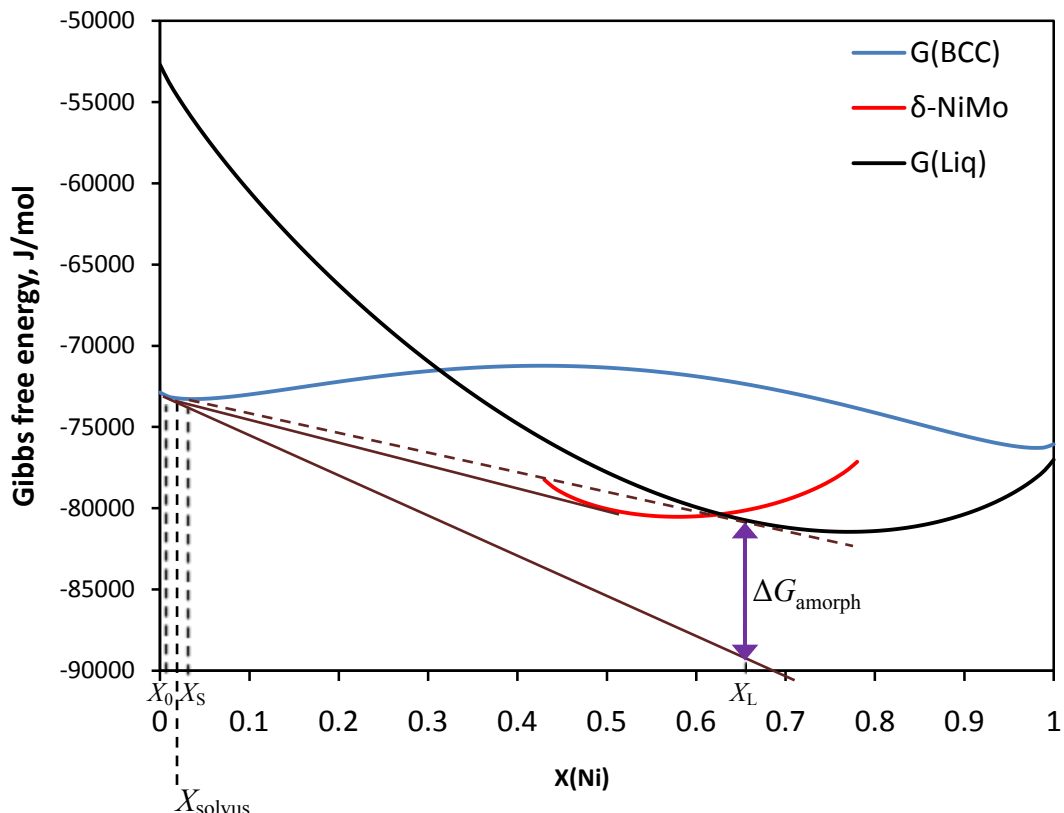
$$\Delta G_{\text{amorph}} = RT \left[X_L \ln \frac{X_s}{X_{\text{solvus}}} + (1 - X_L) \ln \frac{1 - X_s}{1 - X_{\text{solvus}}} \right] - \omega (X_S - X_{\text{solvus}}) (2X_L - X_S - X_{\text{solvus}}) \quad (\text{B.33})$$

for a regular solution, or

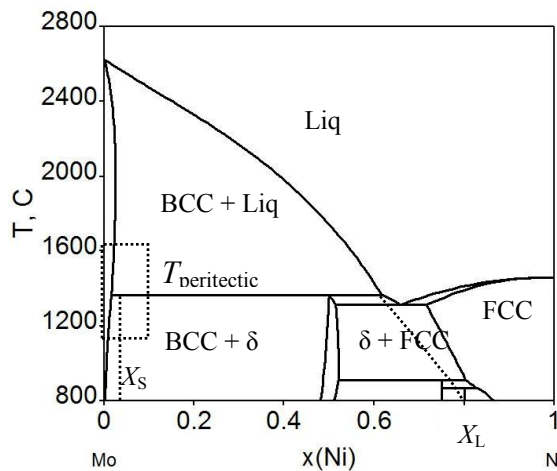
$$\begin{aligned} \Delta G_{\text{amorph}} = RT & \left[X_L \ln \frac{X_s}{X_{\text{solvus}}} + (1 - X_L) \ln \frac{1 - X_s}{1 - X_{\text{solvus}}} \right] - \\ & (X_S - X_{\text{solvus}}) \left[2X_L (L_0^{BCC} + 3L_1^{BCC}) - (L_0^{BCC} + 3L_1^{BCC} + 6L_1^{BCC}) (X_S + X_{\text{solvus}}) + 4L_1^{BCC} (X_S^2 + X_S X + X_{\text{solvus}}^2) \right] \end{aligned} \quad (\text{B.34})$$

for a sub-regular solution.

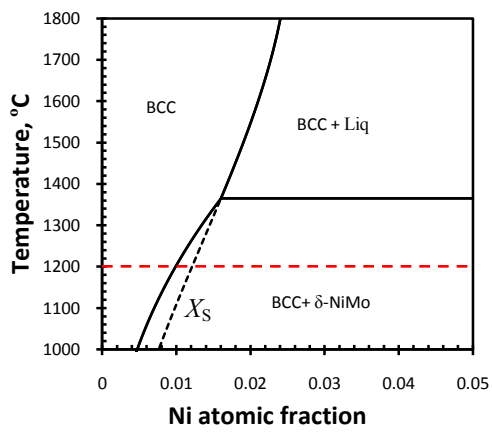
Furthermore, in the sub-peritectic two-phase regime, λ_L 's are horizontal lines, and lines of constant λ_L can be constructed graphically by finding the intersections of constant λ_L lines and the solvus line, as illustrated in Fig. B.5(c).



(a)



(b)



(c)

Figure B.4 (a) The representation of ΔG_{amorph} (X_L) in the plots of Gibbs free energies vs. Ni atomic fraction for a case of $X_0 < X_{\text{solvus}}$ and $T = 1200$ °C ($< T_{\text{peritectic}}$), where X_S is the composition on the metastable extension of the solidus line; **(b)** and **(c)** are the corresponding bulk phase diagram and an expanded view. Bulk solidus and liquidus composition (X_S and X_L respectively) are extended into metastable region as dashed line.

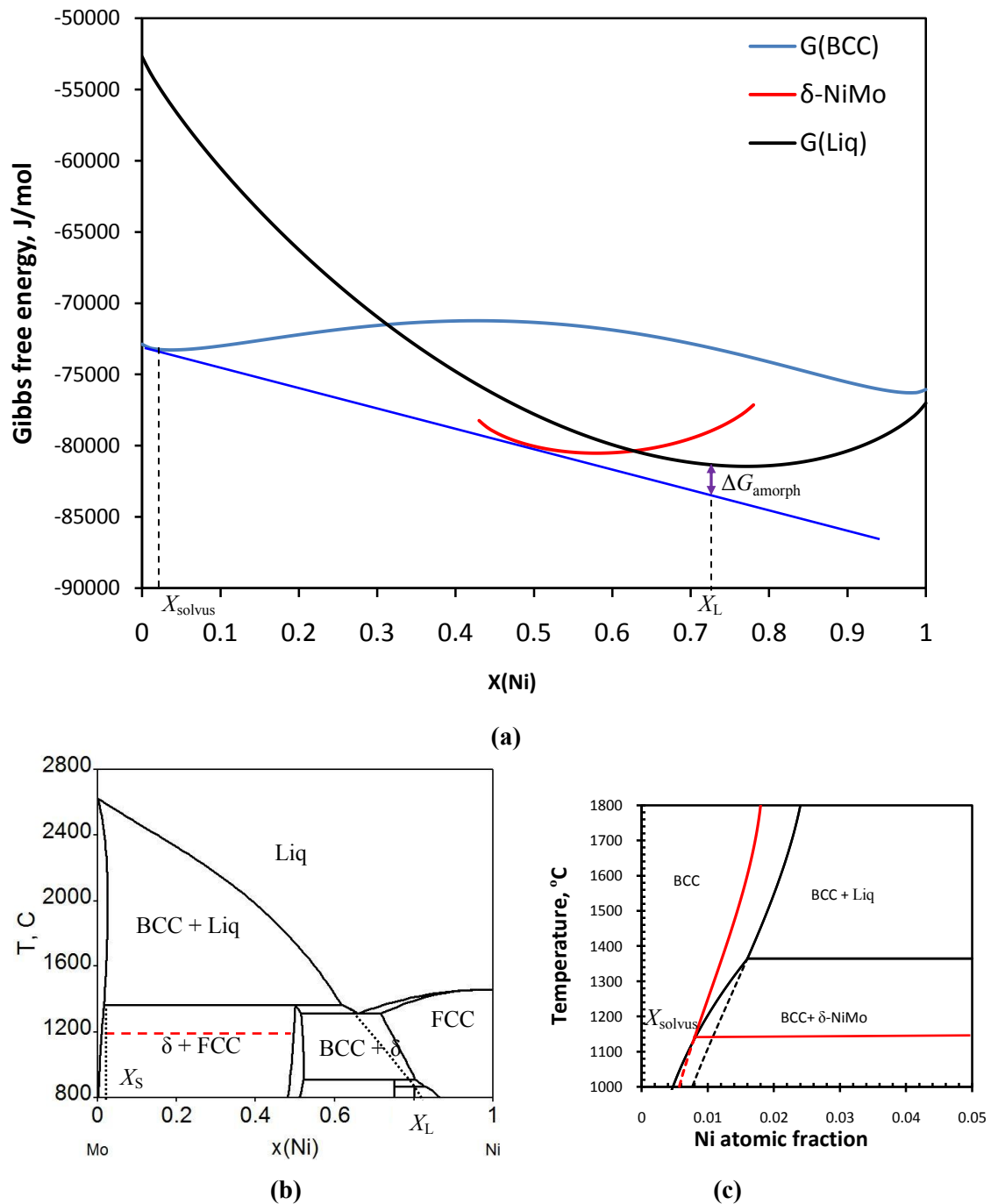


Figure B.5 (a) Illustration of determining ΔG_{amorph} at $T = 1200^{\circ}\text{C}$ in the sub-peritectic two phase regime; (b) Ni-Mo binary phase diagram. The red dashed line represents regime of calculation. (c) Construction of lines of constant λ_L .

(B.5) Computation Resulted for Ni-Doped Mo

We plotted lines of constant computed λ_L in the bulk phase diagram of the Mo-Ni system. This represents a computed “GB diagram,” where λ_L represents the maximum thickness of a quasi-liquid IGF of composition X_L that can be stabilized at Mo GB (an average random GB) without the consideration of interfacial forces and through-thickness compositional and structural gradients. It represents the thermodynamic tendency for a Mo GB to disorder. λ_L (or λ) is not the actual IGF thickness, but it should scale the thickness of the actual (thermodynamically stable) quasi-liquid IGF.

Fig. B.7 further shows computed of λ_L and λ vs. Ni atomic fraction at three representative temperatures. The same trends are found for λ_L and λ (although $\lambda_L < \lambda$); and both are divergent as bulk Ni composition approach to the solidus line (or its metastable extension). For $T < T_{\text{peritectic}}$, λ_L and λ level off at the bulk solvus line $X_0 = X_{\text{solvus}}$, above which the bulk chemical potential is a constant (despite any change in the overall bulk composition in the BCC-NiMo two phase region).

In the single-phase region, computed λ_L (or λ) increases with increase in bulk composition. Above the peritectic temperature, computed λ_L (or λ) is divergent at the bulk solidus temperature. Below the peritectic temperature, computed λ_L (or λ) levels off at the bulk solvus temperature, and it becomes a constant in the BCC-NiMo twp-phase regime.

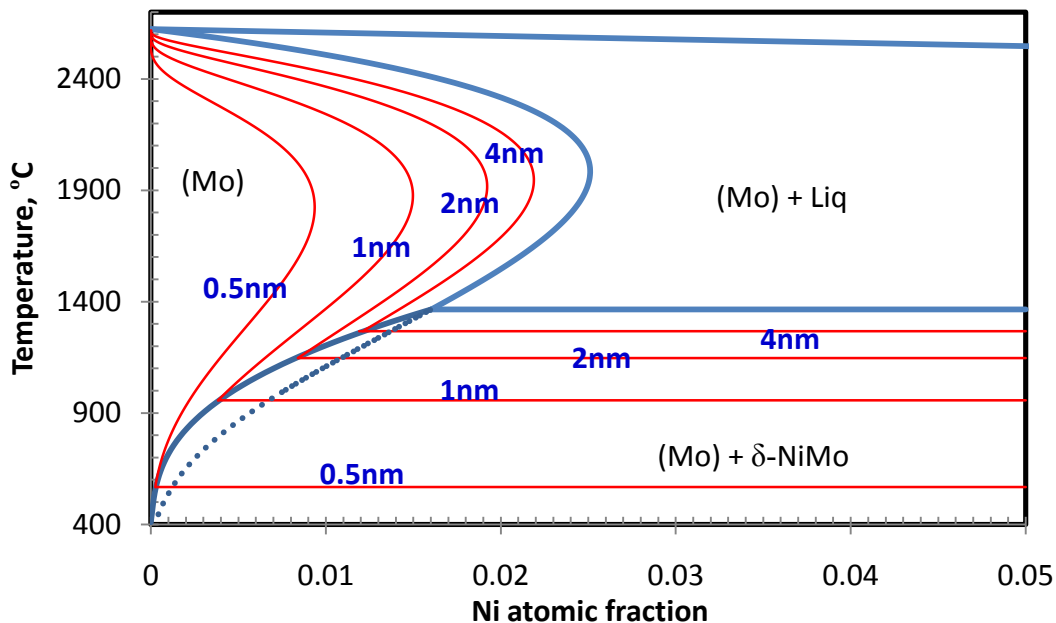


Figure B.6 Computed “grain boundary diagram” for Ni-doped Mo, where computed lines of constant λ_L are plotted in the binary bulk phase diagram. Note that λ_L is the maximum thickness of a quasi-liquid IGF of composition X_L that can be stabilized at an average (random) Mo GB without the consideration of interfacial forces, and it represents a thermodynamic tendency for an average, random, Mo GB to disorder.

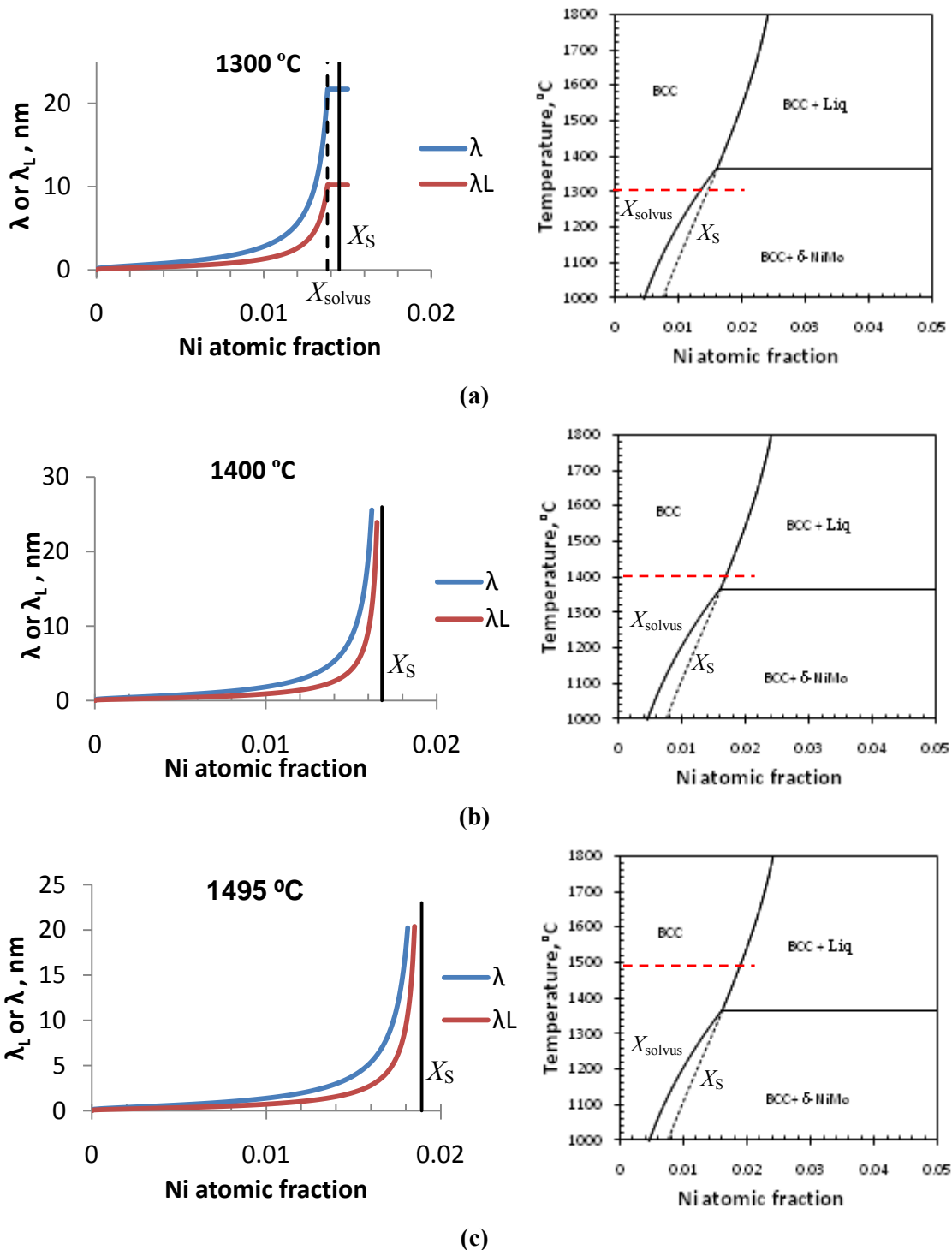


Figure B.7 Plots of λ_L and λ vs. Ni atomic fraction at (a) 1300 °C (a), (b) 1400 °C and (c) 1495 °C, respectively. The dashed vertical line in (a) represents bulk solvus composition; the solid vertical lines represent the bulk solidus compositions (or the composition on the metastable extension of the solidus line for 1300 °C in (a)).

(B.5) Computation Results for Several Doped W Alloys

Similar computations can be conducted for other binary transition metal systems. Computed “GB diagrams” (noting that these are “ λ diagrams”) of Pd, Ni, Fe, and Co doped W are shown in Fig. B-8. These computations were conducted using the CalPhaD data listed in Table B.2. Fig. 2 and Fig. 9 in the narrative are colored versions of this GB diagrams, respectively. The correctness of these computations is validated by comparing with experimentally observed onset sintering temperatures and direct HRTEM characterization, which are discussed in the narrative of this technical report. Computation has also been conducted for Cu-doped W; the results shown that IGFs cannot form. Consistently, it was well known that Cu has no effect for activated sintering of W.

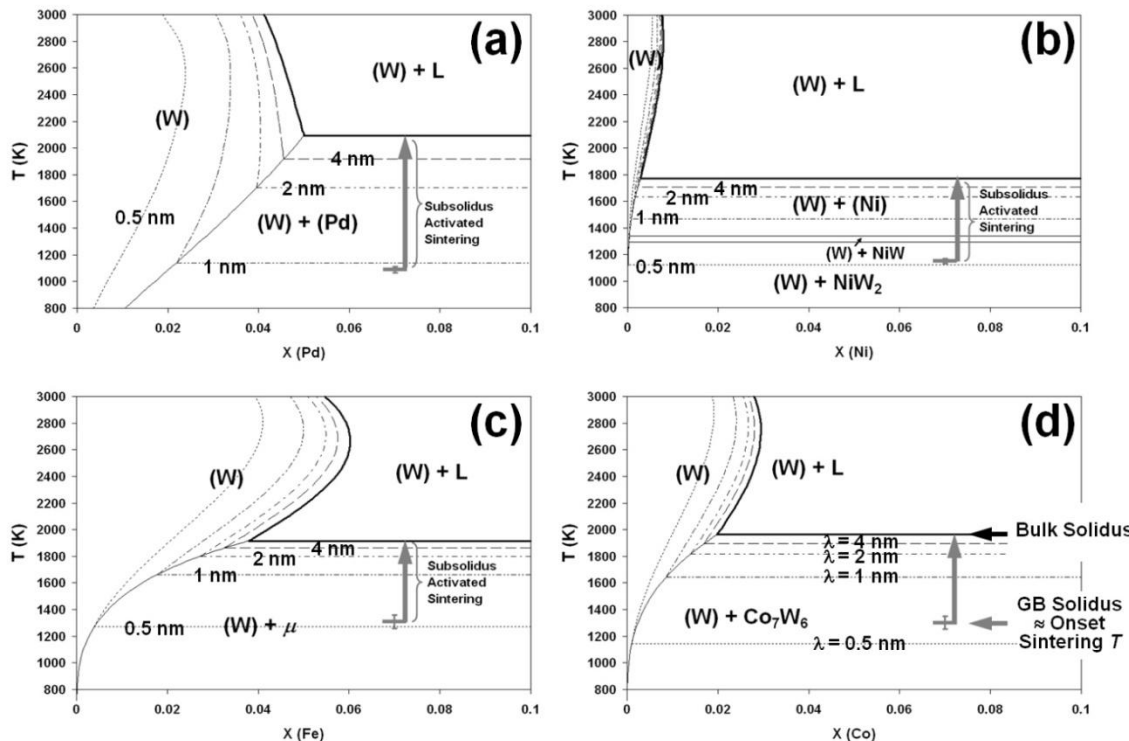


Figure B.8: Computed “GB diagrams” (λ diagrams) of (a) Pd-doped W, (b) Ni-doped W, (c) Fe-doped W, and (d) Co-doped W. In each bulk phase diagram, a series of dashed and dotted lines were plotted to represent the conditions that 4, 2, 1 and 0.5 nm thick quasi-liquid IGFs can be thermodynamically stable at GBs. The ranges of subsolidus activated sintering are also labeled.

Reprinted from an AFOSR supported publication [*Curr. Opin. Solid State Mater. Sci.* 12:81-88 (2008)]

Table B.2 Binary thermodynamic functions used in the calculations.

	Phase	Gibbs free energy (J·mol ⁻¹)	Ref.
W-Ni	Liquid	$X_{Ni}^o G_{Ni}^{liq} + X_W^o G_W^{liq} - T\Delta S_{conf.} + X_{Ni} X_W [16290 - 10.25T - 22450(X_{Ni} - X_W)]$	25
	BCC	$X_{Ni}^o G_{Ni}^{bcc} + X_W^o G_W^{bcc} - T\Delta S_{conf.} + X_{Ni} X_W (78432)$	
	FCC	$X_{Ni}^o G_{Ni}^{fcc} + X_W^o G_W^{fcc} - T\Delta S_{conf.} + X_{Ni} X_W [2556 + 11.6T - 52900(X_{Ni} - X_W)] + G_{mag.}$	
	$\frac{1}{5} Ni_4W$	$\frac{4}{5}^o G_{Ni}^{fcc} + \frac{1}{5}^o G_W^{bcc} - 2572.4 - 0.9494T$	
	$\frac{1}{2} NiW$	$\frac{1}{2}^o G_{Ni}^{fcc} + \frac{1}{2}^o G_W^{bcc} - 4442.95 + 1.5T$	
	$\frac{1}{3} NiW_2$	$\frac{1}{3}^o G_{Ni}^{fcc} + \frac{2}{3}^o G_W^{bcc} - 2963.02 + T$	
W-Co	Liquid	$X_{Co}^o G_{Co}^{liq} + X_W^o G_W^{liq} - T\Delta S_{conf.} + X_{Co} X_W (-42606.6 + 15.5064T)$	26
	BCC	$X_{Co}^o G_{Co}^{bcc} + X_W^o G_W^{bcc} - T\Delta S_{conf.} + X_{Co} X_W (54648)$	
	FCC	$X_{Co}^o G_{Co}^{fcc} + X_W^o G_W^{fcc} - T\Delta S_{conf.} + X_{Co} X_W [-13038 + 8.038T - 11832(X_{Co} - X_W)]$	
	$\frac{1}{13} Co_6W_7$	$\frac{6}{13}^o G_{Co}^{fcc} + \frac{7}{13}^o G_W^{bcc} - 3796.9 - 0.6526T$	
W-Fe	Liquid	$X_{Fe}^o G_{Fe}^{liq} + X_W^o G_W^{liq} - T\Delta S_{conf.} + X_{Fe} X_W [-3607 + 5.65T - 5450(X_{Fe} - X_W)]$	27, 28
	BCC	$X_{Fe}^o G_{Fe}^{bcc} + X_W^o G_W^{bcc} - T\Delta S_{conf.} + X_{Fe} X_W [41544 - 12621(X_{Fe} - X_W)] + G_{mag.}$	
	FCC	$X_{Fe}^o G_{Fe}^{fcc} + X_W^o G_W^{fcc} - T\Delta S_{conf.} + X_{Fe} X_W [25977 - 3.36T - 7258.6(X_{Fe} - X_W)] + G_{mag.}$	
	μ -phase	$y_{Fe}^3^o G_{FeW:Fe}^{\mu} + y_W^3^o G_{FeW:W}^{\mu} + 4(y_{Fe}^3 \ln y_{Fe}^3 + y_W^3 \ln y_W^3)$ where: y_{Fe}^3 and y_W^3 are the site fraction of element Fe and W on sublattice 3. $^o G_{FeW:Fe}^{\mu} = (7^o G_{Fe}^{fcc} + 2^o G_W^{bcc} + 4^o G_{Fe}^{bcc} - 14300 + 26.7T)/13$ $^o G_{FeW:W}^{\mu} = (7^o G_{Fe}^{fcc} + 2^o G_W^{bcc} + 4^o G_{W}^{bcc} - 53450 + 19T)/13$	
	$\frac{1}{3} Fe_2W$	$\frac{2}{3}^o G_{Fe}^{fcc} + \frac{1}{3}^o G_W^{bcc} - 4500 + 1.66667T$	
W-Pd	Liquid	$X_{Pd}^o G_{Pd}^{liq} + X_W^o G_W^{liq} - T\Delta S_{conf.} + X_{Pd} X_W (13868.7 + 10.9322T)$	29
	BCC	$X_{Pd}^o G_{Pd}^{bcc} + X_W^o G_W^{bcc} - T\Delta S_{conf.} + X_{Pd} X_W (9386.8 + 14.6329T)$	
	FCC	$X_{Pd}^o G_{Pd}^{fcc} + X_W^o G_W^{fcc} - T\Delta S_{conf.} + X_{Pd} X_W (-13144 + 16.6866T)$	

(B.6) References for Appendix B

- [1] JG Dash. *Contemporary Phys.* 30 (1989) 89.
- [2] JG Dash, H Fu, JS Wettlaufer. *Rep. Prog. Phys.* 58 (1995) 115.
- [3] JG Dash, AM Rempel, JS Wettlaufer. *Rev. Mod. Phys.* 78 (2006) 695.
- [4] J Luo, Y- Chiang, RM Cannon. *Langmuir* 21 (2005) 7358.
- [5] J Luo. *Crit. Rev. Solid State Mater. Sci.* 32 (2007) 67.
- [6] J Luo, X Shi. *Appl. Phys. Lett.* 92 (2008) 101901.
- [7] X Shi, J Luo. *Appl. Phys. Lett.* 94 (2009)

- [8] N Eustathopoulos, MG Nicholas, B Drevet. *Wettability At High Temperatures* (1999) 420 Pergamon (Elsevier Science Ltd.), Oxford, UK.
- [9] I Shimizu, Y Takei. *Acta Mater.* 53 (2005) 811.
- [10] I Shimizu, Y Takei. *Phys. B* 362 (2005) 169.
- [11] R Benedictus, A Böttger, EJ Mittemijer. *Phys. Rev. B* 54 (1996) 9109.
- [12] AR Miedema, FJA den Broeder. *Z. Met.* 70 (1979) 14.
- [13] FR de Boer, R Boom, WCM Mattens, AR Miedema, AK Niessen. *Cohesion in Metals: Transition Metals Alloys*, North-Holland, Amsterdam, 1988.
- [14] F Spaepen. *Acta Met.* 23 (1975) 729.
- [15] F Spaepen, RB Meyer. *Scrip. Met.* 10 (1976) 257.
- [16] P Wynblatt, D Chatain. Metallurgical and Materials Transactions A (Physical Metallurgy and Materials Science) 37A (2006) 2595.
- [17] D Chatain, C Antion. *Surf.Sci.* 601 (2007) 2232.
- [18] N Saunders, AP Midownik. *CALPHAD: A Comprehensive Guide*, Pergamon, New York, 1998.
- [19] K Frisk. *CALPHAD* 14 (1990) 311.
- [20] SH Zhou, Y Wang, C Jiang, JZ Zhu, L- Chen, Z- Liu. *Mater. Sci. Eng. A* 397 (2005) 288.
- [21] TB Massalski, H Okamoto. *Binary Alloy Phase Diagrams*, ASM International, Ohio., 1990.
- [22] TB Massalski, JL Murray, LH Bennett, H Baker. *Binary Alloy Phase Diagrams*, ASM International, Ohio. (1986) 2224.
- [23] SL Kang, Y Song, WA Kaysser, H Hofman. *Z. Met.* 75 (1986) 86.
- [24] REW Casselton, W Hume-Rothery. *J. Less-Common Met.* 7 (1964) 212.
- [25] P Gustafson, A Gabriel, I Ansara, *Z. Met.* 78 (1987) 151.
- [26] AF Guillermet, *Metall. Trans. A* 20, (1989) 935.
- [27] P Gustafson, A. *Metall. Trans. A* 18 (1987) 175.
- [28] P Gustafson, *Z. Metall.* 79 (1988) 388.
- [29] SK Lee, DN Lee, *CALPHAD* 10 (1986) 61.

Appendix C: Sintering and GB Diffusivities of Ni-Doped Mo

This appendix documents a study to investigate the sintering behaviors of Ni-doped Mo, in which we extracted GB diffusivities systematically. The objectives are twofold:

- We extracted GB diffusivities to provide indirect, yet systematical, experimental evidence to systematically validate the thermodynamic models and computed GB diagrams developed in this AFOSR-YIP.
- Good model-experimental agreements provided further evidence to quantitatively support the proposed solid-state activated sintering mechanism, i.e., the subsolidus accelerated sintering is due to the enhanced diffusion in quasi-liquid IGFs.

The experimental procedures are described in Appendix A. The XRD confirmed that all the Ni was transformed to δ -NiMo compound (Fig. C.1), excluding the possibility of forming a transient liquid.

Sintering temperatures were 1220 °C, 1300 °C, 1350 °C, 1400 °C, 1450 °C, and 1495 °C, respectively, while the peritectic temperature is 1362 °C. Different Ni atomic fractions were selected so that it covered all three phase regimes. The selected experimental conditions are schematically illustrated in Fig. C.2.

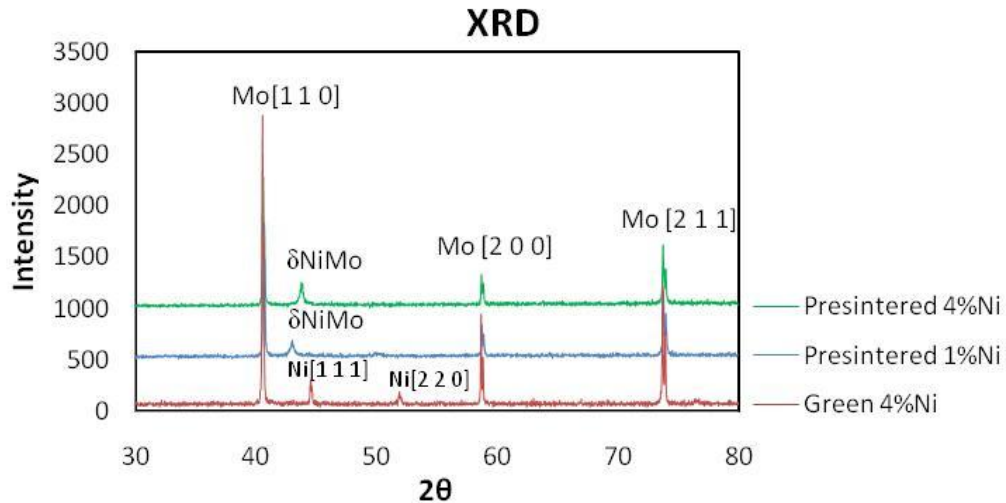


Figure C.1 XRD spectra of Ni-doped Mo. Almost all the Ni has been transformed to δ -NiMo compound after presintering at 1000 °C for 1 hour.

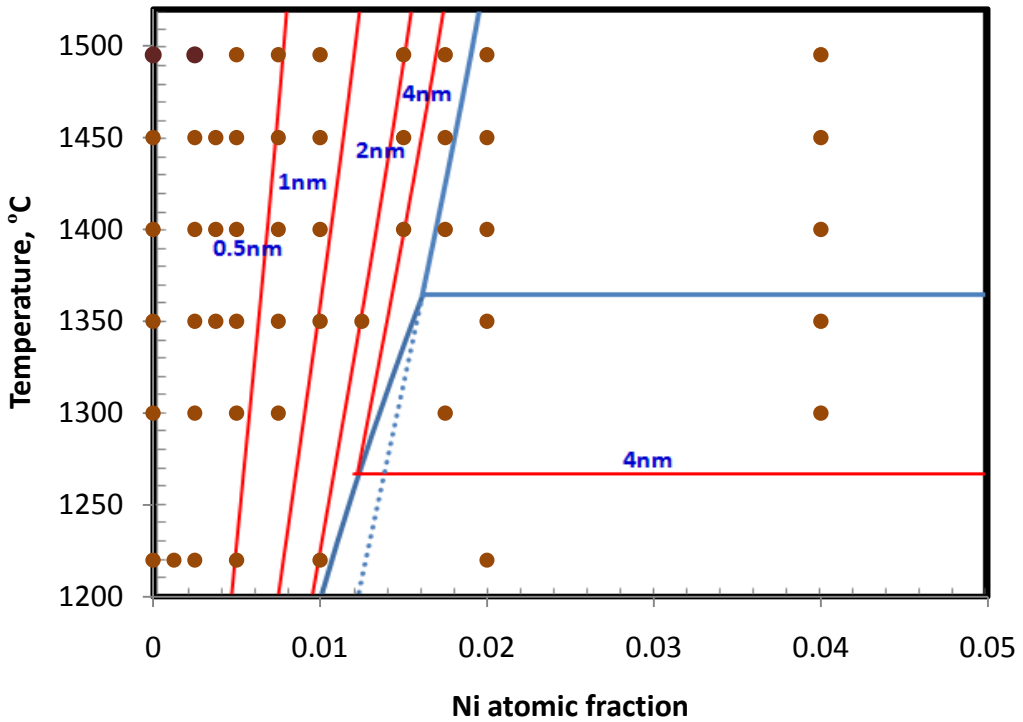


Figure C.2 The selected sintering temperatures and compositions are marked in the Mo-Ni binary phase diagram.

(C.1) Densification and Grain Growth

The densification data for isothermal sintering at eight temperatures are documented in “§C.5 Tables of Densification Data”. Several representative plots of relative density vs. sintering time are shown in Fig. C.3 and Fig. C.4. The densification rate generally increases with increasing Ni content or temperature.

The error bars were determined by following methods. We selected a few representative conditions to prepare 3-4 specimens to obtain means and standard deviations of the measured densities (to represent specimen-to-specimen variations). Based on these measurements, we found that the standard deviation is about 0.005 of the relative density (or 0.0013 in the linear shrinkage, $\Delta L/L_0$) for specimens generally. These error bars were then used as estimated errors bars for other measurements.

The measured grain sizes of samples with different Ni contents and sintering temperatures are shown in Table C.2. The grain growth is almost negligible (within the range of experimental errors) for moderate doping level (≤ 1.5 at % Ni) or at low temperatures (≤ 1300 °C). For the regime where the grain growth is not negligible (the region that is the left-bottom corner by the red line in Table C.2), the effects of grain growth were considered when we extracted the GB diffusivity data via fitting the sintering models.

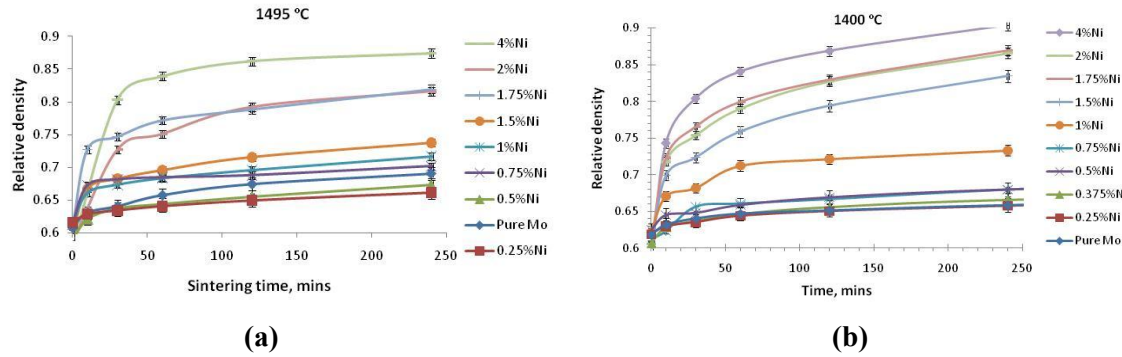


Figure C.3 Relative density vs. sintering time at (a) 1490 °C and (b) 1400 °C ($T_{\text{preitecic}} = 1362$ °C).

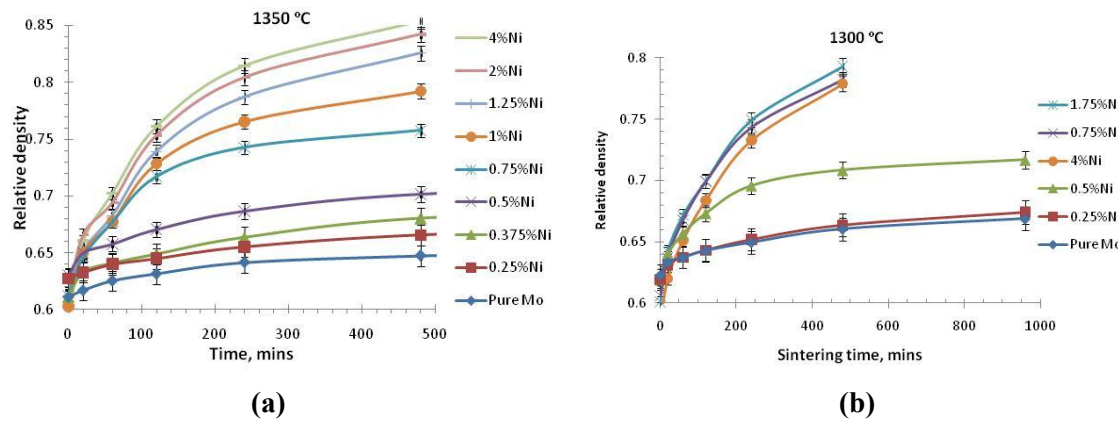


Figure C.4 Relative density vs. sintering time at (a) 1350 °C and (b) 1300 °C ($T_{\text{preitecic}} = 1362$ °C).

Table C.1 Measured grain sizes of Ni-doped Mo samples.

Ni at. %	Sintering temperature, °C	1300 °C	1400 °C	1450 °C	1495 °C
	Sintering time, mins	Grain size, µm	Grain size, µm	Grain size, µm	Grain size, µm
1	0	22.3 ± 7.0	22.3 ± 7.0	22.3 ± 7.0	22.3 ± 7.0
	180	-----	-----	-----	24.4 ± 5.3
	360	-----	-----	-----	28.0 ± 5.4
1.5	0	25.51 ± 11.0	25.51 ± 11.0	25.51 ± 11.0	25.51 ± 11.0
	60	-----	-----	-----	26.6 ± 5.4
	120	-----	23.0 ± 3.3	-----	-----
	240	-----	-----	24.2 ± 3.6	26.3 ± 6.2
1.75	0	26.0 ± 8.6	26.0 ± 8.6	24.0 ± 7.2	26.0 ± 8.6
	30	-----	-----	-----	25.9 ± 4.3
	60	-----	28.8 ± 4.1	-----	26.1 ± 6.5
	120	-----	32.6 ± 5.0	35.1 ± 3.6	40.5 ± 8.0
	240	-----	58.2 ± 12.5	56.5 ± 7.5	55.2 ± 7.0
2	0	29.6 ± 9.6	29.6 ± 9.6	29.6 ± 9.6	29.6 ± 9.6
	60	-----	35.5 ± 5.1	-----	-----
	120	-----	45.9 ± 8.1	-----	-----
	150	23.0 ± 4.1	52 ± 8.1	60.0 ± 9.8	64.9 ± 7.8
4	60	-----	33.8 ± 5.1	-----	-----
	120	-----	54.6 ± 6.0	-----	-----
	240	-----	64.7 ± 9.4	-----	-----

(C.2) Determination of the Controlling Densification Mechanism

The GB diffusivity can be extracted from sintering data only if the densification is controlled by GB diffusion. We can determine whether densification is controlled by GB diffusion (vs. bulk diffusion) by obtain the exponent m for the power law fitting of the initial stage densification kinetics. According to Johnson's model [2] and Kang's sintering theory [3], the linear shrinkage ($\Delta L/L_0$) in the initial stage follows a power law:

$$\frac{\Delta L}{L_0} = \left[K \frac{\gamma_s \Omega D}{kTG^p} \right]^m t^m. \quad (\text{C.1a})$$

The experimentally fitted exponent number m can be used to discriminate what the sintering mechanism is in control [2]. If $m = \sim 0.4-0.5$, the densification is controlled by bulk diffusion, where $K = 6$, $p = 3$, and $D = D_{XL}$. Eq (C.1a) becomes

$$\frac{\Delta L}{L_0} = \left[6 \frac{\gamma_s \Omega D}{kTG^3} \right]^{1/2} t^{1/2}. \quad (\text{C.1b})$$

If $m = \sim 0.33$, the densification is controlled by GB diffusion, where $K = 12$, $p = 4$, and $D = \delta D_{GB}$. Eq. (C.1a) becomes

$$\frac{\Delta L}{L_0} = \left[12 \frac{\gamma_s \Omega D}{kTG^4} \right]^{1/3} t^{1/3}. \quad (\text{C.1c})$$

The index m can be determined experimentally by finding the slope the double logarithmical plot of linear shrinkage vs. time via linear regressions, which are illustrated in Fig. C.5.

The exponents (m 's) were calculated and listed in Table C.2. Only in two samples (pure Mo and 0.25 at % Ni doped Mo, both sintered at 1495 °C), the densification was controlled by bulk diffusion, where GB diffusivity were not measurable. These two specimens are labeled in Fig. C.6 by “X”. In all other specimens, the densification was GB diffusion-controlled, and the GB diffusivities can be extracted. This sintering mechanism map (Fig. C.6) is consistent with a prior report [4].

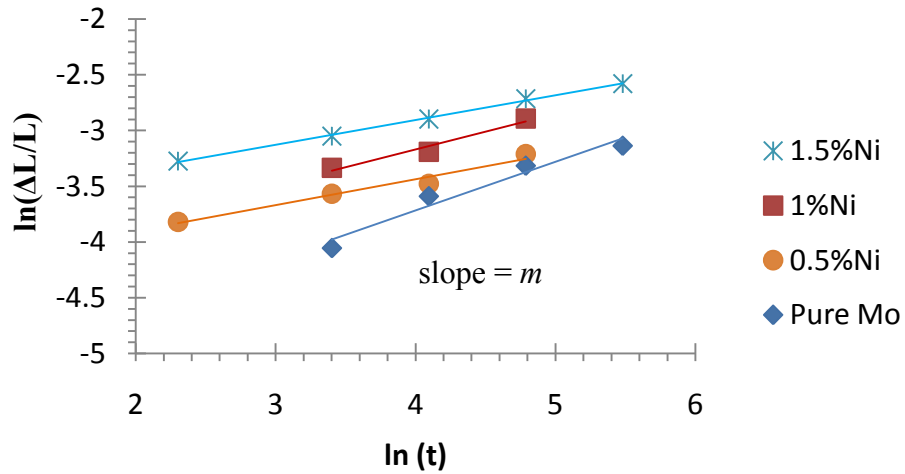


Figure C.5 Double logarithmical plots of linear shrinkage vs. sintering time for samples sintered at 1495 °C. The slopes correspond to the exponents (m 's).

Table C.2 Fitted exponents (m 's)

Ni %\nIndex m	Pure Mo	0.25%	0.5%	1.0%	1.5%
1495 °C	0.44 ± 0.06	0.37 ± 0.02	0.23 ± 0.03	0.32 ± 0.02	0.22 ± 0.03
1450 °C	0.31 ± 0.11	0.23 ± 0.03	0.22 ± 0.03	0.29 ± 0.02	0.20 ± 0.03
1400 °C	0.29 ± 0.06	0.24 ± 0.01	0.26 ± 0.02	0.25 ± 0.04	0.23 ± 0.07
1350 °C	0.28 ± 0.03	0.23 ± 0.03	0.31 ± 0.02	0.36 ± 0.03	-----
1300 °C	0.29 ± 0.06	0.23 ± 0.02	0.28 ± 0.07	-----	-----
1220 °C	0.29 ± 0.06	0.35 ± 0.03	0.26 ± 0.07	0.33 ± 0.08	-----

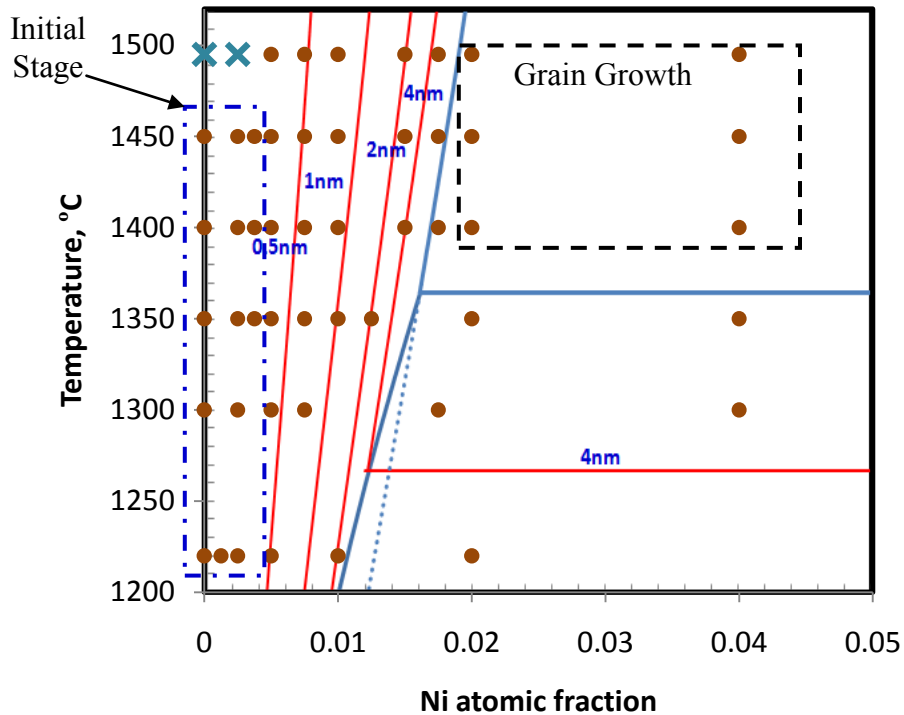


Figure C.6 The experimental conditions are marked in the Mo-Ni bulk phase diagram. The blue “X” indicates where densification is controlled by bulk diffusion. The region where GB diffusivities were determined by fitting the initial stage sintering model and the region where grain growth is not negligible are also indicated in this diagram.

(C.3) Extraction of GB Diffusivities

The sintering models had been discussed systematically in Appendix A. We extracted GB diffusivities from densification data. When it is possible, the intermediate-stage sintering data (linear shrinkage $> 4\%$) are used for better accuracy. In the case of pure Mo and low doping levels (Ni atomic % < 0.5), the total densification is not sufficient to apply the intermediate-stage sintering model, the initial stage densification data were used to obtain GB diffusivities.

For a few cases where both initial and intermediate stage sintering data exist, both Johnson (initial stage) and Coble (intermediate stage) models are used to extract GB diffusivities and the results are listed in Table C.3. The GB diffusivities determined by both models are rather consistent.

We also compared the GB diffusivities determined by the German model (for liquid-phase sintering) and the Coble model (for nominal GB diffusivity via solid-state sintering model) in Table C.4. It can be shown that these two models were roughly equivalent. The calculated results from these two models are in fact consistent.

Table C.3 Comparison of GB diffusivities extracted from the Johnson initial-stage model and the Coble intermediate-stage sintering model.

T, °C	1220	1300	1350	1400	1450	1495
Ni at. %	0.25	0.5	0.5	0.5	0.75	0.5
From initial stage data	1.89E-18	0.97E-17	4.81E-18	7.13E-18	1.74E-17	9.27E-18
From intermediate stage data	1.34E-18	1.20E-17	4.96E-18	6.01E-18	2.36E-17	3.18E-18

Table C.4 Comparison of GB diffusivities determined by using the German and the Coble model for specimens sintered in the liquid-phase sintering region.

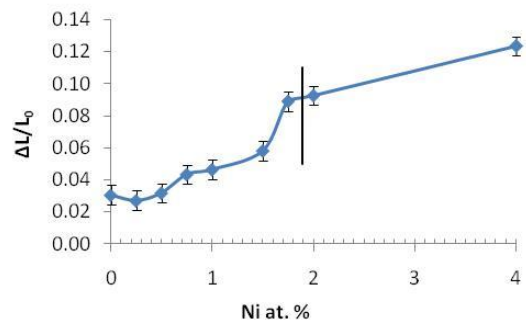
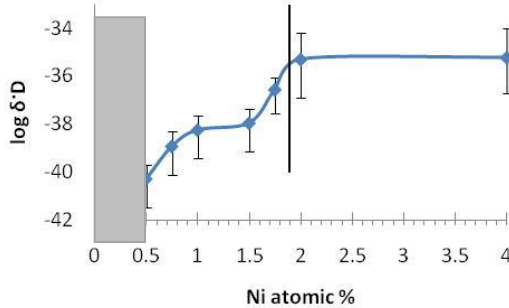
T, °C	1450	1450	1495	1495
Ni at. %	2	4	2	4
The German model	5.21E-16	9.69E-16	6.70E-16	1.58E-15
The Coble model	9.84E-16	13.7E-16	9.86E-16	1.21E-15

(C.4) Results and Comparisons

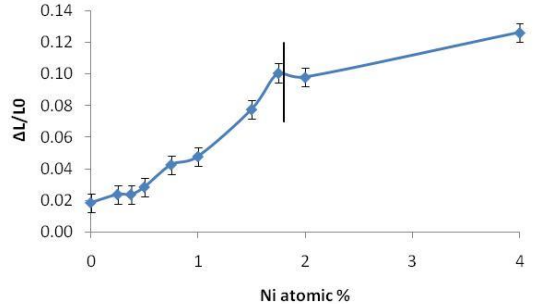
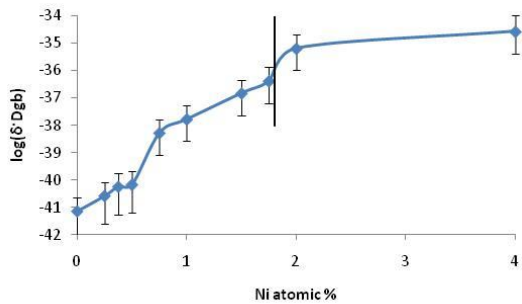
Plots of extracted GB diffusivities vs. Ni contents for six different temperatures between 1220 °C and 1495 °C are shown in Fig. C.7.

Plots of extracted GB diffusivities vs. temperatures are shown in Fig. C.8 (for 2 at. % Ni, in the two-phase regions) and Fig. C.9 (0-1 at. % Ni, in the single-phase region).

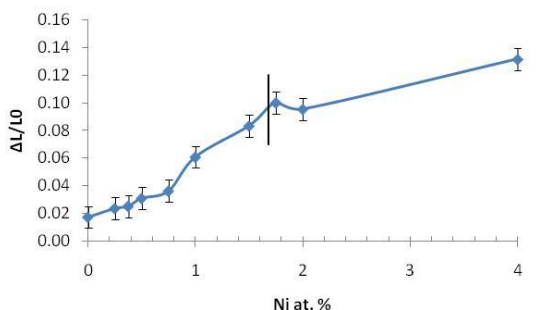
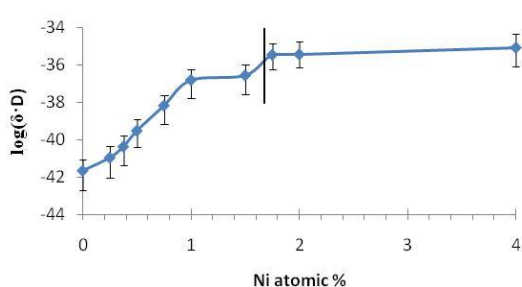
1495 °C:



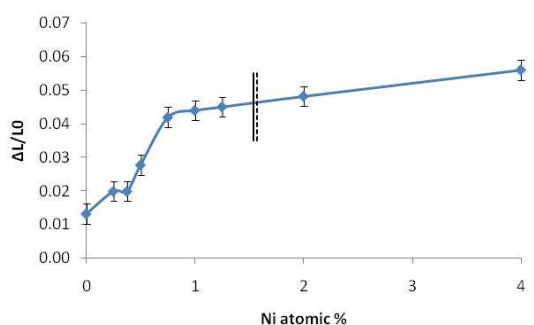
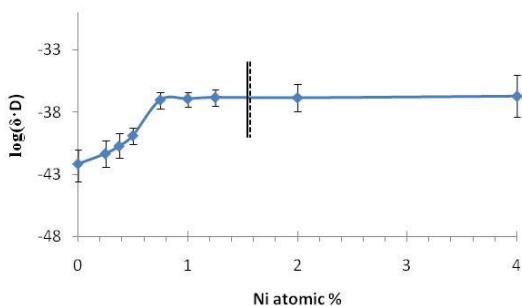
1450 °C:



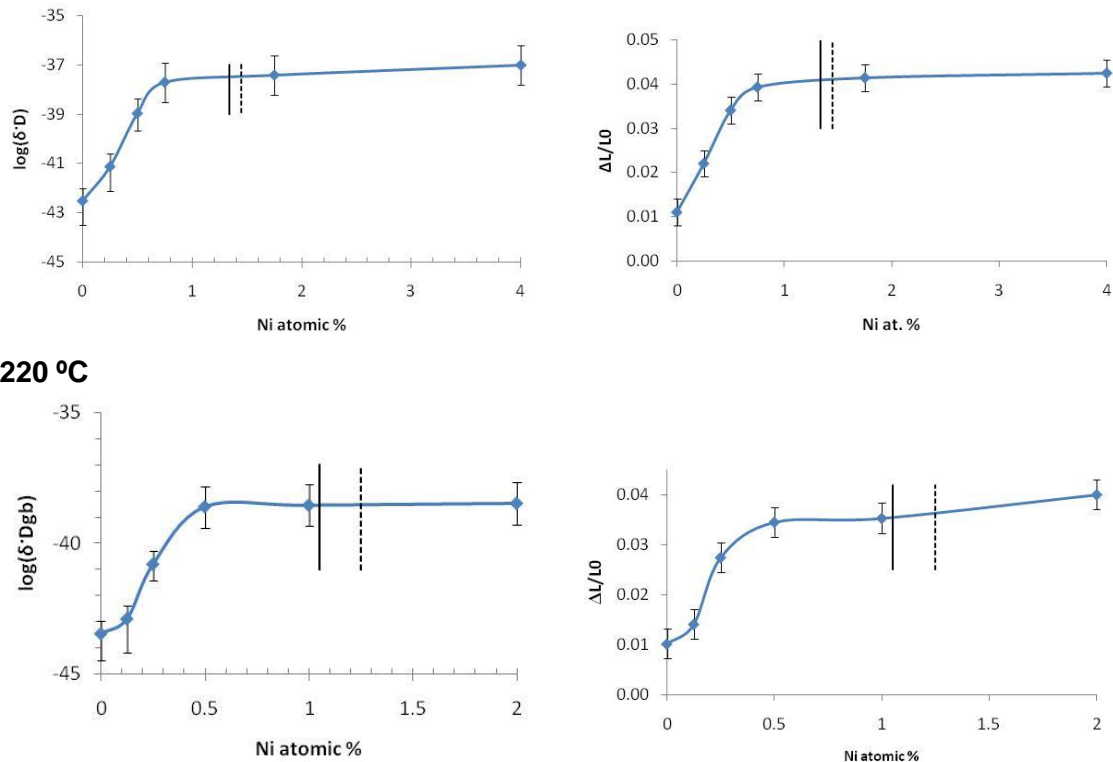
1400 °C:



1350 °C:



1300 °C:



1220 °C

Figure C.7 (Left) Plots of GB diffusivities vs. Ni contents. (Right) Plots of linear shrinkages (after 2-hour isothermal sintering) vs Ni contents. The solid vertical lines represent bulk solidus composition (for $T > T_{\text{pritectic}} = 1362$ °C) or solvus composition (for $T < T_{\text{pritectic}} = 1362$ °C). the dashed vertical lines represent metastable solidus composition (for $T < T_{\text{pritectic}} = 1362$ °C).

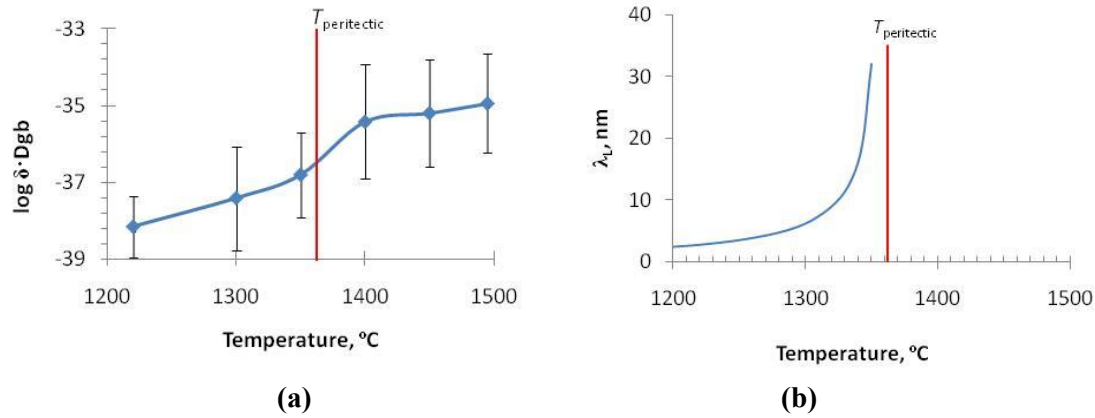


Figure C.8 (a) GB diffusivity vs temperature for 2 at. % Ni doped Mo (in two-phase regions: BCC + δ -Ni-Mo for $T < T_{\text{pritectic}}$ or BCC + liquid for $T > T_{\text{pritectic}}$).
(b) Associated computed λ_L vs. temperature.

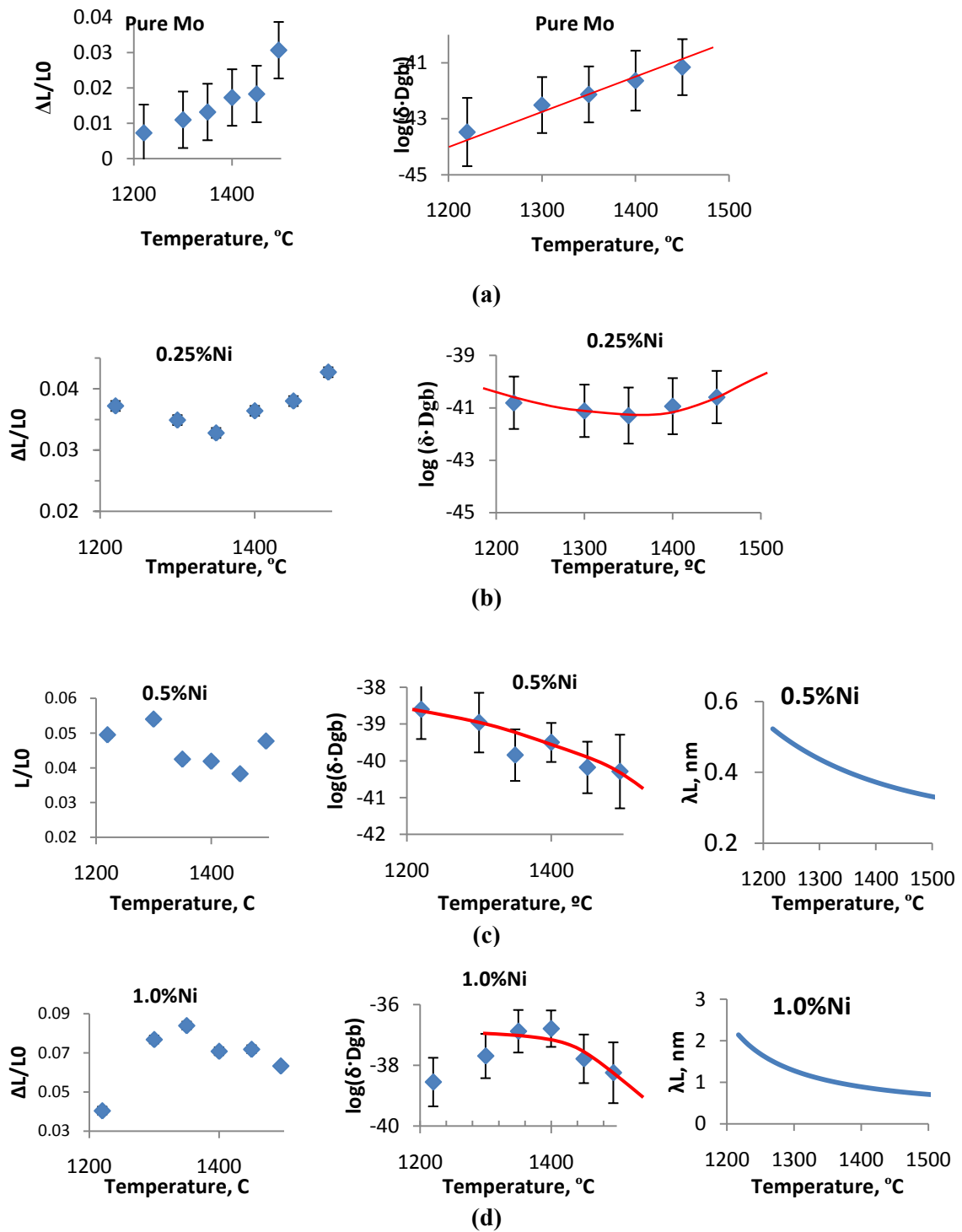


Figure C.9 Temperature dependence of linear shrinkage (after 2 hrs) and GB diffusivity in the single-phase regime for (a) pure Mo, (b) Mo + 0.25% Ni, (c) Mo + 0.5% Ni, and (d) Mo + 1% Ni. The plots of λ_L 's vs. temperatures are also shown.

The comparisons between measured GB diffusivities and the computed GB diagram are summarized in Fig. C.10. The major jumps in GB diffusivities, which are labeled by the red stars in Fig. C.10(A) and (B), occur at a distinct “GB solidus line” that corresponds to a computed λ_L value of ~ 0.5 nm. This GB solidus line, where presumably quasi-liquid IGFs start to form, is marked as a thick red dashed line in Fig. C.10. Since the densification represents an average effect of many GBs with different crystallographic misorientations and inclinations, a gradual transition in GB diffusivity was expected and observed. In contrast, the measured (effective) GB diffusivities only jump moderately at the bulk solidus line where the bulk liquid appears; these are labeled by the blue stars in Fig. C.10 (A) and (E). Furthermore, below the bulk peritectic temperature, there is no discontinuity in the measured GB diffusivity at the bulk solvus line, which is labeled by the light purple star in Fig. C.10(B). This result is fully expected.

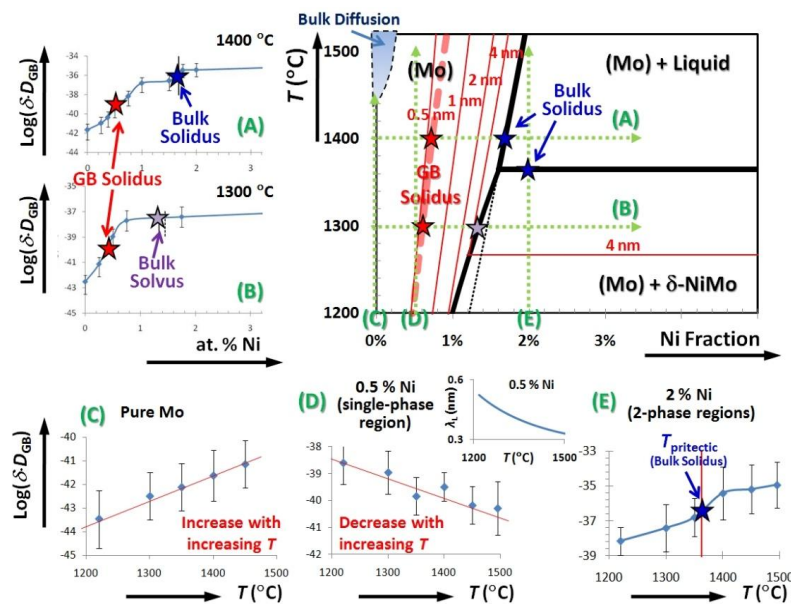


Figure C.10 All trends in the measured GB diffusivities can be explained based on the computed GB diagram for Ni-doped Mo.

The measured GB diffusivity increases with increasing temperature for pure Mo, as shown in Fig. C.10(C). This trend is well expected. However, the measured GB diffusivity appears to decrease with increasing temperature at a constant Ni fraction of 0.5 % (which lies in the single-phase region for all temperatures), as shown in Fig. C.10(D). While this result is highly counter-intuitive, it can be fully explained from the computed GB diagram. This abnormal behavior of decreasing GB diffusivity with increasing temperature is due to the fact that Ni has a “retrograde” solubility in the Mo based BCC phase. With increasing temperature, this fixed composition of 0.5 % moves away to the metastable extension to the solidus line (i.e., the black dotted line in the computed GB diagram in Fig. C.10). Consequently, the free energy penalty for forming an undercooled liquid increases with increasing temperature (for fixed 0.5 % Ni). Consistently, the computed λ_L decreases with increasing temperature; this is shown in the inset of Fig. C.10(D). In conclusion, a GB can “solidify” with increasing temperature! The above comparisons support the correctness and usefulness of our thermodynamic models and the computed GB diagram.

(C.5) Tables of Densification Data

(A) Densification data of specimens that were isothermally sintered at 1495 °C.

Linear shrinkage, $\Delta L/L_0$						
Time, mins	0	10	30	60	120	240
Pure Mo	0.0031	0.0105	0.0204	0.0307	0.0393	0.0464
0.25%Ni	0.0126	0.0204	0.0235	0.0272	0.0314	0.0377
0.50%Ni	0.0000	0.0199	0.0288	0.0320	0.0377	0.0477
0.75%Ni	0.0047	0.0372	0.0419	0.0435	0.0451	0.0514
1.00%Ni	0.0078	0.0351	0.0413	0.0466	0.0529	0.0633
1.50%Ni	0.0031	0.0414	0.0503	0.0582	0.0687	0.0786
1.75%Ni	0.0031	0.0713	0.0781	0.0891	0.0959	0.1101
2.00%Ni	0.0047		0.0801	0.0926	0.1091	0.1179
4.00%Ni	0.0031		0.1148	0.1234	0.1344	0.1384
Relative density, ρ						
Pure Mo	0.620	0.631	0.643	0.649	0.660	0.666
0.25%Ni	0.616	0.629	0.634	0.641	0.649	0.661
0.50%Ni	0.588	0.621	0.638	0.645	0.656	0.674
0.75%Ni	0.615	0.673	0.682	0.685	0.688	0.702
1.00%Ni	0.613	0.661	0.674	0.684	0.696	0.717
1.50%Ni	0.599	0.667	0.683	0.696	0.716	0.738
1.75%Ni	0.605	0.727	0.747	0.772	0.789	0.819
2.00%Ni	0.586	-----	0.727	0.751	0.792	0.816
4.00%Ni	0.581	-----	0.803	0.839	0.862	0.874

(B) Densification data of specimens that were isothermally sintered at 1450 °C.

Linear shrinkage, $\Delta L/L_0$						
Time, mins	0	10	30	60	120	240
Pure Mo	0.0031	0.0110	0.0142	0.0183	0.0236	0.0283
0.25%Ni	0.0094	0.0162	0.0189	0.0236	0.0273	0.0330
0.375%Ni	0.0031	0.0162	0.0194	0.0236	0.0288	0.0367
0.50%Ni	0.0094	0.0215	0.0241	0.0283	0.0325	0.0383
0.75%Ni	0.0047	0.0288	0.0325	0.0425	0.0461	0.0571
1.00%Ni	0.0047	0.0356	0.0388	0.0477	0.0519	0.0718
1.50%Ni	0.0031	0.0540	0.0660	0.0776	0.0833	0.0894
1.75%Ni	0.0031	0.0692	0.0854	0.1006	0.1127	0.1242
2.00%Ni	0.0031	0.0655	0.0833	0.0980	0.1111	0.1237
4.00%Ni	0.0047	0.0949	0.1127	0.1263	0.1357	0.1426
Relative density, ρ						
Pure Mo	0.616	0.630	0.636	0.643	0.653	0.661
0.25%Ni	0.613	0.622	0.627	0.634	0.642	0.652
0.375%Ni	0.602	0.624	0.629	0.636	0.646	0.660
0.50%Ni	0.625	0.642	0.645	0.652	0.660	0.672
0.75%Ni	0.609	0.650	0.657	0.673	0.683	0.706
1.00%Ni	0.623	0.664	0.668	0.687	0.694	0.736
1.50%Ni	0.601	0.698	0.720	0.746	0.757	0.777
1.75%Ni	0.607	0.732	0.767	0.803	0.834	0.868
2.00%Ni	0.605	0.724	0.762	0.798	0.830	0.865
4.00%Ni	0.606	0.782	0.828	0.866	0.892	0.911

(C) Densification data of specimens that were isothermally sintered at 1400 °C.

Linear shrinkage, $\Delta L/L_0$								
Time, mins	0	10	30	60	120	240	480	960
Pure Mo	0.0016	0.0094	0.0142	0.0173	0.0200	0.0241	0.0294	0.0346
0.25%Ni	0.0079	0.0157	0.0189	0.0236	0.0272	0.0314	0.0377	0.0451
0.375%Ni	0.0031	0.0157	0.0200	0.0252	0.0303	0.0357	0.0404	0.0477
0.50%Ni	0.0079	0.0220	0.0241	0.0309	0.0362	0.0419	0.0482	0.0556
0.75%Ni	0.0047	0.0299	0.0330	0.0362	0.0430	0.0519	0.0618	0.0781
1.00%Ni	0.0031	0.0383	0.0461	0.0608	0.0645	0.0708	-----	-----
1.50%Ni	0.0031	0.0550	0.0671	0.0833	0.0980	0.1132	-----	-----
1.75%Ni	0.0031	0.0671	0.0875	0.1001	0.1132	0.1268	-----	-----
2.00%Ni	0.0031	0.0629	0.0797	0.0954	0.1101	0.1242	-----	-----
4.00%Ni	0.0031	0.0928	0.1174	0.1316	0.1405	0.1520	-----	-----
Relative density, ρ								
Pure Mo	0.618	0.632	0.641	0.647	0.651	0.659	0.668	0.679
0.25%Ni	0.619	0.630	0.635	0.644	0.650	0.657	0.670	0.684
0.375%Ni	0.607	0.628	0.637	0.646	0.656	0.665	0.675	0.689
0.50%Ni	0.624	0.645	0.648	0.659	0.669	0.680	0.693	0.709
0.75%Ni	0.623	0.656	0.661	0.667	0.680	0.699	0.720	0.754
1.00%Ni	0.621	0.671	0.682	0.712	0.721	0.733	-----	-----
1.50%Ni	0.602	0.699	0.723	0.759	0.794	0.834	-----	-----
1.75%Ni	0.601	0.723	0.765	0.799	0.830	0.869	-----	-----
2.00%Ni	0.606	0.718	0.754	0.790	0.827	0.866	-----	-----
4.00%Ni	0.577	0.743	0.804	0.841	0.869	0.904	-----	-----

(D) Densification data of specimens that were isothermally sintered at 1350 °C.

Time, mins	Linear shrinkage, $\Delta L/L_0$						
	0	20	60	120	240	480	940
Pure Mo	0.0047	0.0083	0.0132	0.0168	0.0220	0.0247	0.0288
0.25%Ni	0.0110	0.0162	0.0199	0.0225	0.0278	0.0335	0.0383
0.375%Ni	0.0031	0.0157	0.0199	0.0241	0.0320	0.0404	0.0451
0.50%Ni	0.0079	0.0220	0.0278	0.0341	0.0425	0.0503	0.0540
0.75%Ni	0.0063	0.0262	0.0419	0.0618	0.0734	0.0802	-----
1.00%Ni	0.0031	0.0294	0.0440	0.0681	0.0839	0.0959	-----
1.25%Ni	0.0063	0.0288	0.0451	0.0723	0.0922	0.1085	-----
2.00%Ni	0.0031	0.0330	0.0482	0.0749	0.0970	0.1116	-----
4.00%Ni	0.0031	0.0346	0.0561	0.0828	0.1053	0.1216	-----
Relative density, ρ							
Pure Mo	0.611	0.617	0.625	0.632	0.641	0.647	0.655
0.25%Ni	0.627	0.633	0.640	0.645	0.655	0.666	0.675
0.375%Ni	0.611	0.633	0.641	0.649	0.664	0.680	0.690
0.50%Ni	0.631	0.650	0.658	0.671	0.687	0.702	0.710
0.75%Ni	0.612	0.646	0.677	0.717	0.743	0.758	-----
1.00%Ni	0.603	0.650	0.678	0.729	0.766	0.792	-----
1.25%Ni	0.612	0.651	0.683	0.739	0.787	0.826	-----
2.00%Ni	0.612	0.666	0.694	0.753	0.804	0.842	-----
4.00%Ni	0.603	0.661	0.702	0.761	0.815	0.854	-----

(E) Densification data of specimens that were isothermally sintered at 1300 °C.

Linear shrinkage, $\Delta L/L_0$							
Time, mins	0	20	60	120	240	480	960
Pure Mo	0.0031	0.0094	0.0110	0.0142	0.0173	0.0236	0.0278
0.25%Ni	0.0110	0.0178	0.0220	0.0252	0.0299	0.0362	0.0419
0.50%Ni	0.0094	0.0215	0.0341	0.0425	0.0540	0.0660	0.0729
0.75%Ni	0.0047	0.0225	0.0393	0.0550	0.0760	0.0922	-----
1.75%Ni	0.0031	0.0262	0.0414	0.0561	0.0791	0.0975	-----
4.00%Ni	0.0047	0.0262	0.0425	0.0597	0.0828	0.1038	-----
Relative density, ρ							
Pure Mo	0.623	0.634	0.637	0.643	0.650	0.660	0.669
0.25%Ni	0.619	0.631	0.637	0.643	0.652	0.664	0.674
0.50%Ni	0.619	0.640	0.656	0.673	0.696	0.708	0.717
0.75%Ni	0.606	0.637	0.668	0.699	0.743	0.782	-----
1.75%Ni	0.601	0.642	0.672	0.700	0.749	0.793	-----
4.00%Ni	0.584	0.620	0.651	0.684	0.733	0.779	-----

(F) Densification data of specimens that were isothermally sintered at 1220 °C.

Linear shrinkage, $\Delta L/L_0$							
Time, mins	0	10	40	120	240	480	1440
Pure Mo	0.0063	0.0063	0.0063	0.0102	0.0118	0.0181	0.0236
0.125%Ni	0	0.0032	0.0105	0.0142	0.0168	0.0231	0.0262
0.25%Ni	0.0094	0.0110	0.0157	0.0275	0.0322	0.0398	0.0487
0.50%Ni	0.0094	0.0110	0.0157	0.0346	0.0495	0.0692	0.0891
1.00%Ni	0.0063	0.0110	0.0173	0.0354	0.0404	0.0634	0.0818
2.00%Ni	0.0047	0.0142	0.0236	0.0401	0.0542	0.0713	-----
Relative density, ρ							
Pure Mo	0.614	0.614	0.615	0.623	0.626	0.637	0.647
0.125%Ni	0.602	0.607	0.618	0.624	0.629	0.640	0.646
0.25%Ni	0.617	0.620	0.627	0.651	0.659	0.672	0.688
0.50%Ni	0.623	0.625	0.633	0.669	0.698	0.739	0.783
1.00%Ni	0.598	0.605	0.615	0.649	0.661	0.704	0.743
2.00%Ni	0.591	0.610	0.625	0.656	0.684	0.720	-----

(G) Densification data of specimens that were isothermally sintered at 1160 °C.

Linear shrinkage, $\Delta L/L_0$							
Time, mins	0	30	60	150	290	600	1080
2.00%Ni	0.0047	0.0126	0.0168	0.0194	0.0304	0.0456	0.0577
4.00%Ni	0.0047	0.0115	0.0162	0.0194	0.0278	0.0409	0.0535
Relative density, ρ							
2.00%Ni	0.615	0.630	0.637	0.641	0.662	0.691	0.717
4.00%Ni	0.602	0.615	0.622	0.629	0.643	0.669	0.694

(H) Densification data of specimens that were isothermally sintered at 1100°C.

Linear shrinkage, $\Delta L/L_0$							
Time, mins	0	60	120	240	480	960	1620
2.00%Ni	0.0047	0.0101	0.0121	0.0220	0.0278	0.0393	0.0478
Relative density, ρ							
2.00%Ni	0.608	0.618	0.622	0.640	0.651	0.674	0.690

(C.6) References for Appendix C

- [1] J Luo. *Crit. Rev. Solid State Mater. Sci.* 32 (2007) 67.
- [2] DL Johnson. *J. Appl. Phys.* 40 (1969) 192.
- [3] SL Kang. *Sintering*, Butterworth-Heinemann, 2004.
- [4] JT Smith. *J. App. Phys.* 36 (1965) 595.
- [5] RL Coble. *J. App. Phys.* 32 (1961) 787.
- [6] SJ Park, SH Chung, JM Martin, JL Johnson, RM German. *Metall Mat Trans A* 39 (2008) 2941.
- [7] WD Kingery, MD Narasimhan. *J. Appl. Phys.* 30 (1959) 301.
- [8] WD Kingery. *J. Appl. Phys.* 30 (1959) 301.
- [9] RM German. *Liquid Phase Sintering*, Plenum Press, New York, 1985.
- [10] AA Clifford. *Multivariate Error Analysis*, Applied Science Publishers LTD, London, 1973.
- [11] J Luo, H Wang, Y- Chiang. *J. Am. Ceram. Soc.* 82 (1999) 916.
- [12] VK Gupta, DH Yoon, HM Meyer III, J Luo. *Acta Mater.* 55 (2007) 3131.